Hydrodynamic loads on oversized cylindrical cargo during marine transport

R.G.M. Wijnands

Delft University of Technology

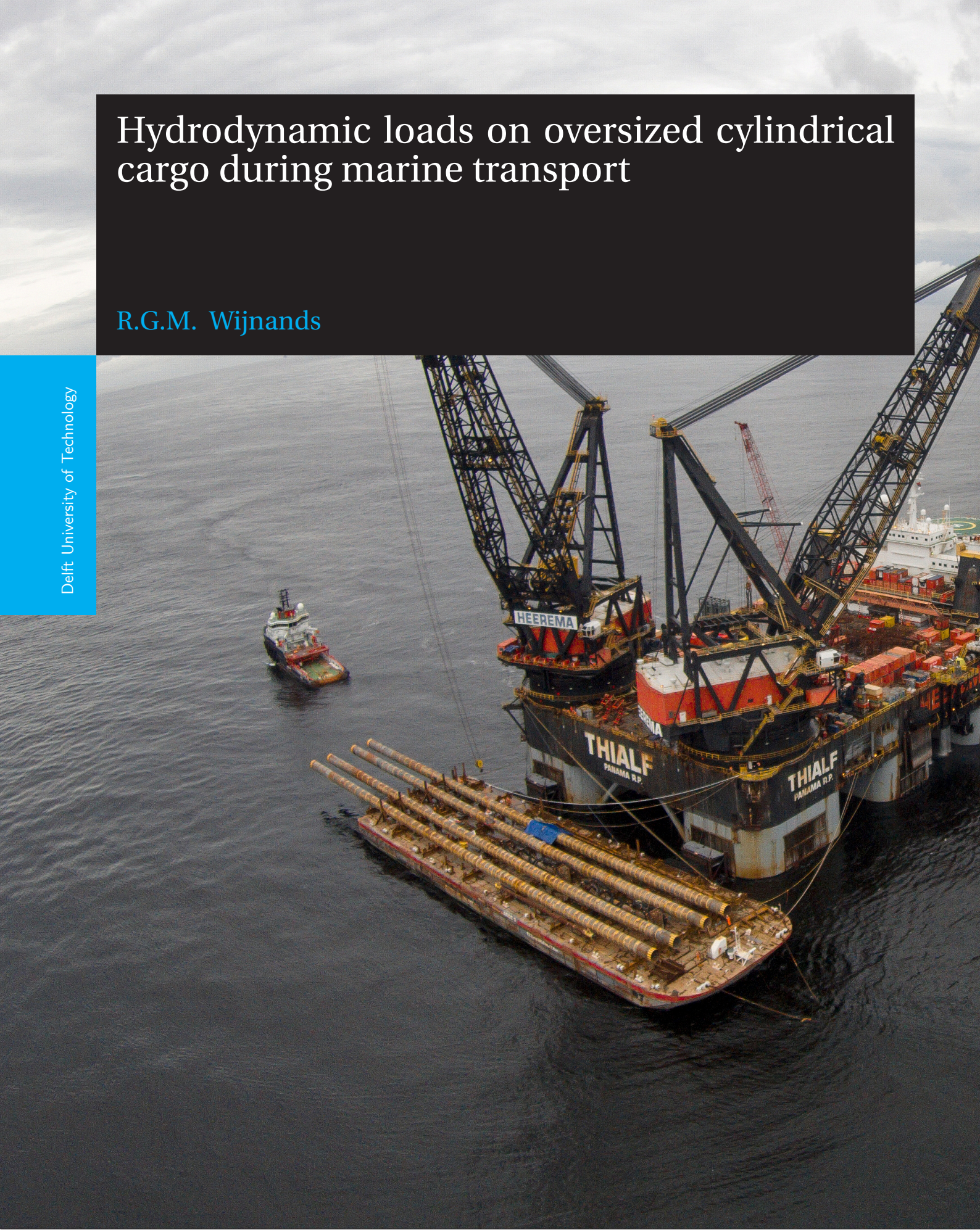

TU Delft Delft University of Technology

Challenge the future

Hydrodynamic loading on oversized cylindrical cargo during marine transport

BY

R.G.M. Wijnands
1521527

10-04-2015

in partial fulfillment of the requirements for the degree of

Master of Science
in Civil Engineering

at the Delft University of Technology,
to be publicly defended on April the 15th, 2015 at 15:00.

Chair	prof. dr. ir. W.S.J. Uijttewaal,	TU Delft
Committee	ir. A. van der Toorn,	TU Delft
	ir. J. den Haan,	TU Delft
	ir. A. Jongbloed,	HMC

An electronic version of this thesis is available at http://repository.tudelft.nl/.



The work in this thesis was supported by Heerema Marine Contractors. Their cooperation is hereby gratefully acknowledged.

Abstract

With the increase in size of offshore structures and the increase in costs related to the construction of these facilities, a necessity to optimize the construction of offshore facilities arises. An element that contributes greatly to these costs is the transportation and installation of the structures. Transportation costs are proportional to the distance covered and the number of transports necessary, since special vessels or tug boats are required. Installation costs are mainly proportional to time since the day rates of specialized construction vessels are extremely high.

One of the most used structural members in offshore construction are steel cylindrical structural members, such as piles and pipelines. With increasing dimensions, also these members increase in size and it is often found wishful from a viewpoint of cost efficiency to transport the members on barges that are smaller in length than their cargo. Not only are standardized cargo barges more widely available then specialized equipment, their use also saves on fuel costs and pollution due to their reduced resistance compared with vessels that are greater in dimensions.

Due to forces induced by the sea state the barges move and the oversized cargo undergoes a relative motion with regard to the sea surface. In certain environmental conditions this relative motion can develop in such a way that impact and/or submergence of the cargo occurs. This thesis focuses on the hydrodynamic loads involved with this interaction of oversized steel piles and the sea.

The relative motions have been determined from a linearized motion analysis of an industry standard 122 m long cargo barge. A radiation and diffraction analysis using potential theory software WAMIT has been performed to 1) determine the hydrodynamic coefficients of the barge, and 2) determine the effect of radiation and diffraction on the fluid pressures in the surrounding fluid field. It was found that the relative motions have a peak amplitude at wave periods that are commonly encountered in marine transport. This holds for approaches with and without taking into account the effects of wave radiation and diffraction. The analysis of the relative motions shows that for large enough wave heights water impact is possible to occur.

To be able to quantify the loads an extensive literature review has been conducted on the involved hydrodynamic processes. It was found that knowledge on the governing load mechanisms is available. Water exit effects are less well covered in literature and conservative upper limit assumptions have been made to account for water exit effects. For quantification of the involved hydrodynamic loads, two approaches have been developed. First, a quasi-stationary approach is chosen to analyze the hydrodynamic loads. Four characteristics orientations have been identified which give a good representation of the maximum loading situations. The parameters for this approach are found from a spectral analysis of the relative motions, both with and without taking diffraction and radiation effects into account. By using this approach a lot of additional conservatism is introduced, which is mainly caused by using upper limit values for the relative motion and slamming force coefficient. To gain a more detailed insight in the magnitude of different load contributions therefore a second approach has been developed. This approach consists of a segmented force model that operates on time traces drawn from response spectra of the relative motions. The cylinder is divided into segments

and the involved loads are determined per segment per time step. The total resulting forces are found by summing the contributions of every segment along the pile length. Using a case study of a recently conducted transport the differences between the two approaches have been investigated. It is found that the maximum loads from the segmented model approach are roughly a factor 2 to 10 smaller than the results from a quasi-stationary approach. Compared with an existing engineering method, the forces from the segmented model are lower for all wave headings except stern waves. The comparison is skewed however because in the current engineering method not all involved loads are accounted for. To gain more confidence in the results of the segmented approach, the model is validated by means of three characteristic situations. The validation shows slight conservatism in the results of the segmented model. Ultimately the segmented model shows that when wave diffraction and radiation are taken into account, a wave heading of 180° is most favorable. With this an additional argument for towed marine transports to weathervane in stormy weather is found.

The contribution of this thesis is that it demonstrates that using a detailed approach with regard to hydrodynamics may be beneficial. Although in a segmented model approach the analyses have to be repeated multiple times to gain a statistically reliable result, it is noted that once a model is available the computational costs do not differ a lot from a traditional frequency domain approach. This thesis therefore opens possibilities to reduce costs involved with offshore construction or marine transport in general.

Further work should be directed at validating the obtained results by means of full scale or model testing, including effects of more complicated cargo configurations, investigating different cargo geometries, and studying the influence of the dynamics of load transfer to support structures.

Preface

This report describes the research conducted as the final part for the Master of Science degree in Civil Engineering at the Delft University of Technology. During my studies the scale and complexity of offshore structures and operations have been an increasingly interested topic for me. As a student in Civil Engineering many of the theories used in this study were new to me, of which mostly the theory on marine hydrodynamics and the related software. I am thankful for the opportunity that Heerema Marine Contractors (HMC) has given me to further explore this interesting field of study with a relevant practical problem.

First I would like to thank Arnold Jongbloed for giving me the opportunity to conduct this research at HMC. His guidance and commitment have been very valuable and his coaching is very much appreciated. From TU Delft I would like to thank Ad van der Toorn for his involvement. He always provided sharp, but constructive criticism and always made time for my questions. Thorough reviews of intermediate reports and his analogies with related disciplines have greatly contributed to the quality of the final result. I also would like to thank Joost den Haan for his involvement and genuine interest in the subject. With his expertise on marine hydrodynamics he made sure that my understanding of the fundamentals of the problem was thorough enough. This, combined with his drive to push me to better model building have made his involvement with this work of great value. I would like to thank the chair of my committee, Wim Uijttewaal, for keeping a helicopter view and the good comments during the entire process.

My time at HMC has certainly been made enjoyable by my colleagues and fellow graduate students. In no particular order I would like to thank Ernst, Scott, Remko, Mattijs, Carel, Michiel, Michiel, Henk, and Aris for all the coffees and good laughs.

Finally I would like to thank my friends and my family for their support. I would like to direct a special word of thanks to Cor, Gerda, and Bram for their support during my entire studies. My gratitude is endless.

I wish you an interesting read.

Delft, April 2015

Rik

Contents

Abstract iii

Preface v

Contents vi

Glossary ix

Physical Constants xi

Nomenclature xiii

1 Introduction 1
- 1.1 Motivation for research . . . 1
- 1.2 Background . . . 2
- 1.3 Problem Statement . . . 4
- 1.4 Report Outline . . . 6

2 Literature Review 7
- 2.1 Inertia related loads . . . 7
- 2.2 Drag Loads . . . 8
- 2.3 Water entry . . . 14
- 2.4 Water exit . . . 18
- 2.5 Motions of floating bodies . . . 19
- 2.6 Conclusions regarding literature . . . 20

3 Methodology 23
- 3.1 Motion Analysis . . . 24
- 3.2 Current engineering approach . . . 34
- 3.3 Quasi-stationary approach . . . 35
- 3.4 Segmented model approach . . . 40

4 Simulations 47
- 4.1 Case study description . . . 47
- 4.2 Current engineering approach . . . 51
- 4.3 Quasi-stationary approach . . . 51
- 4.4 Segmented model approach . . . 54

4.5 Comparison of results 60

5 Validation of segmented force model **61**
5.1 Stationary, fully emerged, horizontal orientation 62
5.2 Stationary, fully submerged, horizontal orientation 63
5.3 Constant velocity, still water, horizontal orientation 65

6 Discussion **67**
6.1 Motion influencing assumptions 67
6.2 Load influencing assumptions 68

7 Conclusions and recommendations **71**
7.1 Conclusions 72
7.2 Recommendations 75

A Hydrodynamics **77**

B RAO plots **95**

C Current engineering methodology **107**

D Flowcharts **113**

E Source code of developed models **115**

Bibliography **129**

List of Figures **131**

List of Tables **137**

Glossary

CFD	Computational Fluid Dynamics
COB	Center of Buoyancy
COF	Center of Floatation
COG	Center of Gravity
DOF	Degree of Freedom
EOM	Equation of Motion
IFFT	Inverse Fast Fourier Transform
FFT	Fast Fourier Transform
FRF	Frequency Response Function
HTV	Heavy Transport Vessel
JONSWAP	Joint North Sea Wave Project
MPM	Most Probable Maximum
MSL	Mean Sea Level
P95	5% exceedance probability
POI	Point of Interest
RAO	Response Amplitude Operator
WAMIT	Wave Analysis MIT

Physical Constants

Gravitational acceleration	g	$=$	$9.81\,\mathrm{m\,s^{-2}}$
Kinematic viscosity of water	ν	$=$	$1.004 \times 10^{-6}\,\mathrm{m^2\,s^{-1}}$
Mass density of water	ρ_w	$=$	$1.025 \times 10^{3}\,\mathrm{kg\,m^{-3}}$
Mass density of steel	ρ_s	$=$	$7.850 \times 10^{3}\,\mathrm{kg\,m^{-3}}$

Nomenclature

β	wave heading	$^\circ$
γ	peak shape parameter	-
ζ	wave amplitude	m
η	surface elevation	m
λ	wave length	m
ω	angular frequency	rads^{-1}

a	acceleration	ms^{-2}
C_D	drag coefficient	-
C_e	water exit coefficient	-
C_m	added mass coefficient	-
C_M	inertia coefficient	-
C_s	slamming coefficient	-
D	cylinder outer diameter	m
Fr	Froude number	-
H_s	significant wave height	m
k	wave number	-
KC	Keulegan-Carpenter number	-
m	mass	kg
Re	Reynolds number	-
r_i	cylinder inner radius	m
r_o	cylinder outer radius	m
T	wave period	s
T_p	peak wave period	s
T_z	mean zero crossing period	s
u	water particle velocity	ms^{-1}

Chapter 1

Introduction

1.1 Motivation for research

With an ever increasing human demand for energy, many sources of energy that were previously considered economically or technologically unfeasible to use have now become lucrative to exploit. One of the main areas of interest for this quest for energy is the offshore exploration and production of oil and gas, and more recently renewable sources of energy such as offshore wind. Since these sources have a proven potential to be profitable, offshore construction of both fixed and floating structures related to winning these sources of energy has experienced a large growth during the past decades.

With increasing complexity the general trend is that offshore structures become larger and are constructed in greater water depths. This development leads to numerous challenges, of which one is the efficient transportation of structural modules to the construction location offshore. The costs involved with offshore construction are high. For a typical offshore wind farm for example, the costs of installation and logistics currently account for more than 20% of the total costs [Smaling, 2013]. Due to high day rates of offshore construction equipment, the work that is done in-situ has to be reduced to a minimum. For the transport to the construction site it holds that a transport duration in the order of weeks is not uncommon, and therefore the number of transports also contributes in a large amount to the construction costs. Combining this and the fact that barges of adequate size are not always available leads to a more often occurring situation in which from a cost efficiency viewpoint it is wishful to conduct marine transports of which the cargo dimensions are larger than the transportation equipment. Due to the relative motions of the transportation vessels and the sea surface, the parts that stick out can come into contact with the water suface during transportation. This contact can result in non-linear dynamic loads such as slamming and water scooping. Although various (simplified) calculation methods are available, the mechanisms of slamming and scooping are still not well understood and are difficult to quantify.

1.2 Background

1.2.1 Cylindrical members in offshore construction

This thesis will focus on cylindrical members as being the cargo. Steel cylindrical elements are the most widely applied structural members in offshore construction. They are for example used in the construction of jackets, as foundation for large structures such as bottom founded or floated oil and gas rigs, as substructures for offshore windmills as so called monopiles, and for subsea pipelines. Examples of these applications are shown in figure 1.1. Because offshore structures in general are increasing in size, also the mentioned sub-elements are taking on larger dimensions.



(A) Pipeline [1]



(B) Jacket on a barge



(C) Monopile founded windmill [2]

FIGURE 1.1: Pictures of cylindrical members in offshore applications

1.2.2 Marine transport

For marine transport a lot of different possibilities exist, each with their advantages and disadvantages. Semi-submersible transport vessels, also known as *heavy transport vessels* or HTV's, for example are used for transportation of very large and heavy cargo. The costs involved with this kind of equipment however are large and their availability is limited. Transportation of cargo on seagoing barges towed by

[1] Source: `http://subseaworldnews.com/`
[2] Source: `http://www.typhoonoffshore.eu/`



(A) Production rig on a HTV[3]

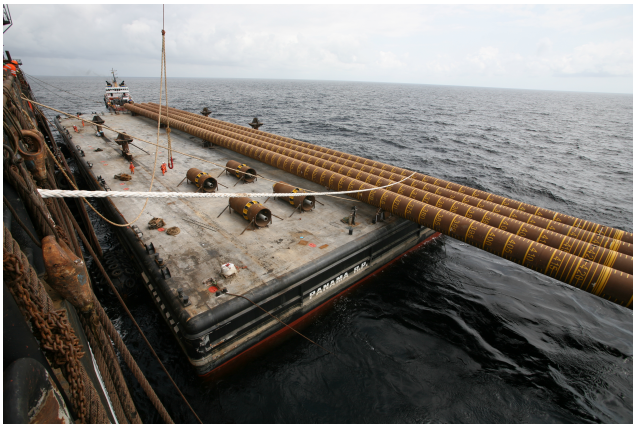

(B) Foundation piles with overhang on barge

FIGURE 1.2: Pictures of heavy marine transport for offshore applications

tug boats is more common and the availability of standardized barges is much higher and is considered to be more flexible. An example of both methods is given in figure 1.2.

The barges are normally towed or pushed by tug boats and usually are flat top and bottom. They are classified by amongst others their length and width. Typical transport barges used in the offshore industry range from 200 ft. up to 450 ft. in length, of which the 300 ft. and 400 ft. barges are the most commonly used. The 400 ft. barges were considered ideal for transporting piles and bridges used in offshore structuers due to their deck space, avoiding the risk of wave slamming. With pile lengths steadily increasing over the years this risk however comes up again because the same barges are still in use because of economic reasons.

It is useful to be able to quantify the hydrodynamic loads involved with wave slamming. First, the structures with which the cargo is secured to the barge should be desgined to withstand these loads. An example of this so called *sea fastening* is shown in figure 3.5b. An accurate assessment of the loads does not only save on the costs of material for the sea fastening. It also potentially reduces the time that is needed offshore to remove the sea fastening again offshore. This saves critical and very costly time during offshore construction and possibly reduces weather windows and therefore increases workability. Secondly an accurate description of the loads can be useful to assess fatigue-life build up.

[3]Source: `http://www.dockwise.com/`

1.3 Problem Statement

Hydrodynamic loads on oversized cylindrical cargo, induced by the relative motion of the structures on a barge and the sea surface, are difficult to quantify. Due to the many uncertainties and the complexity of the problem, currently these situations are avoided or a presumable conservative approach is chosen, both resulting in a non-optimal situation.
Being able to quantify the loads in an accurate manner will gain insight in the extent of the problem and potentially reduce costs of offshore transport and installation.

1.3.1 Research questions and focus

This thesis will focus on the hydrodynamic loads that occur due to the interaction of rigid cylindrical structural members and the water during marine transport. The main questioned to be answered in this study is therefore defined as follows:

"What are the hydromechanic loads on oversized cargo during towed marine transport and how can these loads be quantified?"

To answer this question in a structured manner, several sub questions are formulated. These sub questions are:

1. In which configurations do the transports normally occur and what are common lengths of overhang?
2. What are the relative motions of the water and the oversized structure starting at the moment of water impact until water exit, neglecting the effect of the submergence on the motions?
3. Which physical phenomena play a role during the entry, submergence, uprising and exit of the structure in the water body and how can these processes be quantified?
4. How can the quantified loads be integrated into a numerical model?
5. What are the differences in the results of a numerical model compared with the current engineering approach?

1.3.2 Research demarcation

Due to time constraints this study is focused on conditions that are most commonly encountered in practice. This focus limits the scope of this thesis to:

Cylindrical members
Because of the many applications of cylindrical members in offshore construction, as described in section 1.2.1, the scope of this thesis is limited to cylindrical members. Many of the investigated matters, such as relative motions, would still hold valid for different geometries. However the loading

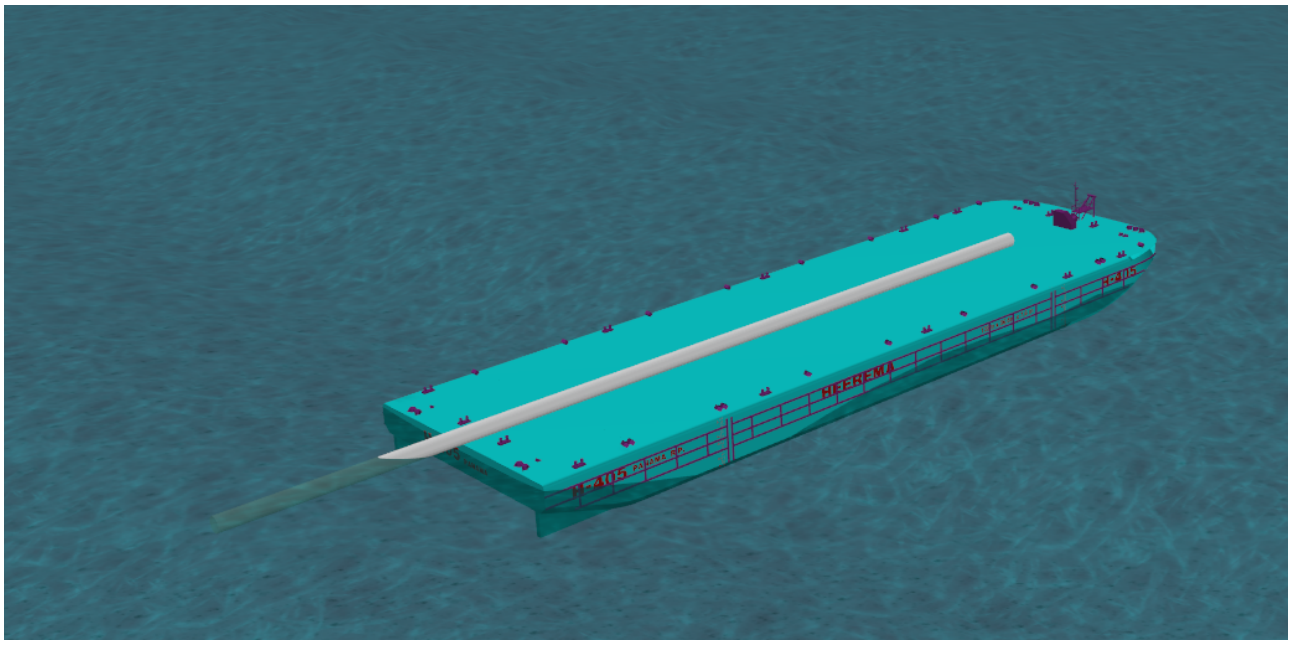

FIGURE 1.3: Simulation screenshot of oversized cylinder transport

mechanisms would change. Therefore when one might be interested in other geometries as well, parts of this thesis might still be useful.

Standard cargo barge

The most commonly used barges for heavy marine transport are standardized cargo barges with a length of 122 m, as described in section 1.2.2. In this study one specific barge is used as a case study, but it is assumed that the characteristics of this barge are representative for the standardized 122 m barges. The results of most analyses have been made dimensionless, such that they are applicable to barges or vessels that deviate in dimensions. It should be noted however that this only holds valid for small deviations and situations in which the proportions of the dimensions are equal. For very different vessels, the relative motions, and therefore the loads, would change significantly. This is not further elaborated upon in this thesis.

Stern overhang at center line

In this study only cylindrical members that are oversized with regard to the stern of a barge are considered. This is illustrated in in figure 1.3. This is a often occurring situation in practice, because mostly one end of the structure should still be accessible for handling reasons. However, since wave headings over 360° are investigated, and the barge can be more or less considered symmetrical, a bow overhang is similar to a stern overhang with mirrored wave heading. For cylinders that are oversized at port or starboard side, or that are placed eccentric with regard to the barge x-axis, the analysis is limited valid (see figure 2.9). This is because for reasons of simplicity roll motions are neglected in this thesis. Roll motions would introduce additional velocities and accelerations at wave headings other than 0° or 180°. When a barge motion model is used that accounts for these effects, the analysis of the loading mechanisms would still be valid.

1.4 Report Outline

In this section the outline of the report is briefly described per chapter.

Chapter 1 The first chapter describes the context of the research and its applicability. The background to the problem is explained and industry common practice is explored. The research focus is then defined by means of research questions. Finally the boundaries of the research are set out in the demarcation.

Chapter 2 Chapter two is a review of the available literature that has a relation to this study. The main part is related to the hydrodynamic loading mechanisms on cylinders and the influence of different parameters on these mechanisms. Also the motions of floating rigid bodies and the way they can be analyzed are introduced. Concluding the applicability of the theory is discussed and a decision is made on the values for different coefficients that will be used.

Chapter 3 The third chapter outlines the methodology in which the hydrodynamic loads will be determined. First an analytical description of the relative motions is given. Next, a quasi-stationary approach is introduced which is composed of four characteristics orientations. Subsequently a second approach is introduced in which a segmented model is used to quantify the loads.

Chapter 4 Chapter four is an elaboration of the methodologies that are introduced in chapter three. First a description is given of a case study. This case study is then used to apply the two different methodologies on. Next, the results of both approaches are given and compared with results from a current engineering methodology. Ultimately, using the segmented model approach, a number of variation studies have been done to investigate the relations of various parameters with regard to force results.

Chapter 5 Chapter five is formed by a validation of one of the developed methodologies. Because the creation of this methodology has been a major effort in this thesis, confidence in the results is herewith increased.

Chapter 6 In the sixth chapter a critical reflection on the approaches is given. The validity of the applied theorems as described in chapter two is underpinned. Subsequently the influence of various assumptions that have been made throughout this thesis is discussed.

Chapter 7 Chapter seven is the last chapter of the main body and it concludes the research by means of answering the research questions that were formulated in chapter one. Noteworthy conclusions are drawn and recommendations for future research are formulated.

Chapter 2

Literature Review

In this chapter relevant literature to the subject under investigation is outlined and summarized. This mainly relates to the loads on cylindrical structures by waves and currents and secondarily the dynamics of floating bodies. The main hydrodynamic loads on the structures can be divided into inertia loads as described in section 2.1, drag loads as described in section 2.2, water entry loads as described in section 2.3, and water exit loads as described in section 2.4. Additionally the dynamics of floating rigid bodies are briefly outlined.

2.1 Inertia related loads

Inertia of mass is one of the fundamental principles of classical physics. The force due to inertia can be described with equation 2.1. For the problem under investigation, not only the mass inertia of the cylindrical structure itself should be considered, but also the contribution due to the water that has to be accelerated when the cylinder is submerged.

$$F_i = ma \tag{2.1}$$

The first contribution to this is the water that fill the cylinder when it submerges and no end plates are used. When end plates are used this contribution will not exist, but additional buoyancy effects have to be taken into account. The second contribution is due to inertia added to the system because the cylinder must accelerate some volume of surrounding fluid as well as it moves through. For simplicity this can be modeled as a volume of fluid moving with the object, referred to as *added mass* or *hydrodynamic mass* . The total load due to mass inertia then can be written as equation 2.2. The mass of the filled cylinder is then given by equation 2.3 and the added mass for a cylinder is given by equation 2.4.

$$F_i = (m + m_{added})a \tag{2.2}$$

$$m = \left(\pi r_i^2 \rho_w + \pi(r_o^2 - r_i^2)\rho_s\right) \Delta x \tag{2.3}$$

$$m_{added} = \rho \pi r_o^2 C_m \Delta x \tag{2.4}$$

In which:

r_i	=	Cylinder inner radius
r_o	=	Cylinder outer radius
ρ_w	=	Mass density of water
ρ_s	=	Mass density of steel
Δx	=	Cylinder length considered
C_M	=	Added mass coefficient

The determination of C_m under various conditions will be treated in the following sections.

2.2 Drag Loads

In this section the forces on the structure due to drag are described. Drag forces originate from two sources, namely shear forces between the water flow and the cylinder surface (friction forces) and a pressure difference induced by flow separation due to the form of the structure (form resistance). To gain insight, first the case of steady current will be described. Subsequently the influence of oscillatory flow and regular waves is regarded. Ultimately also the effect of wave irregularity is described.

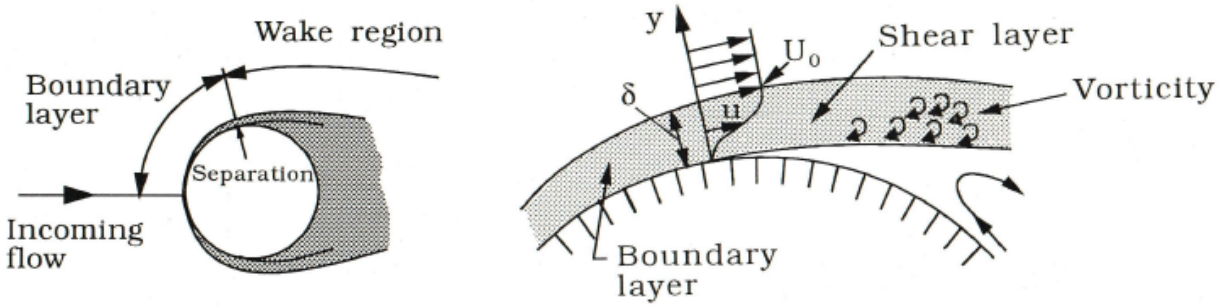

(A) Definition sketch

(B) Viscous boundary layer

FIGURE 2.1: Definition sketch for drag force sources. [Sumer and Fredsoe, 1997]

2.2.1 Steady Current

The general form to determine drag forces is given by equation 2.5. With increasing Re number (defined by equation 2.6) form resistance gets more important and friction forces can be neglected.

$$F_D = \frac{1}{2}\rho_w D C_D u^2 \Delta x \tag{2.5}$$

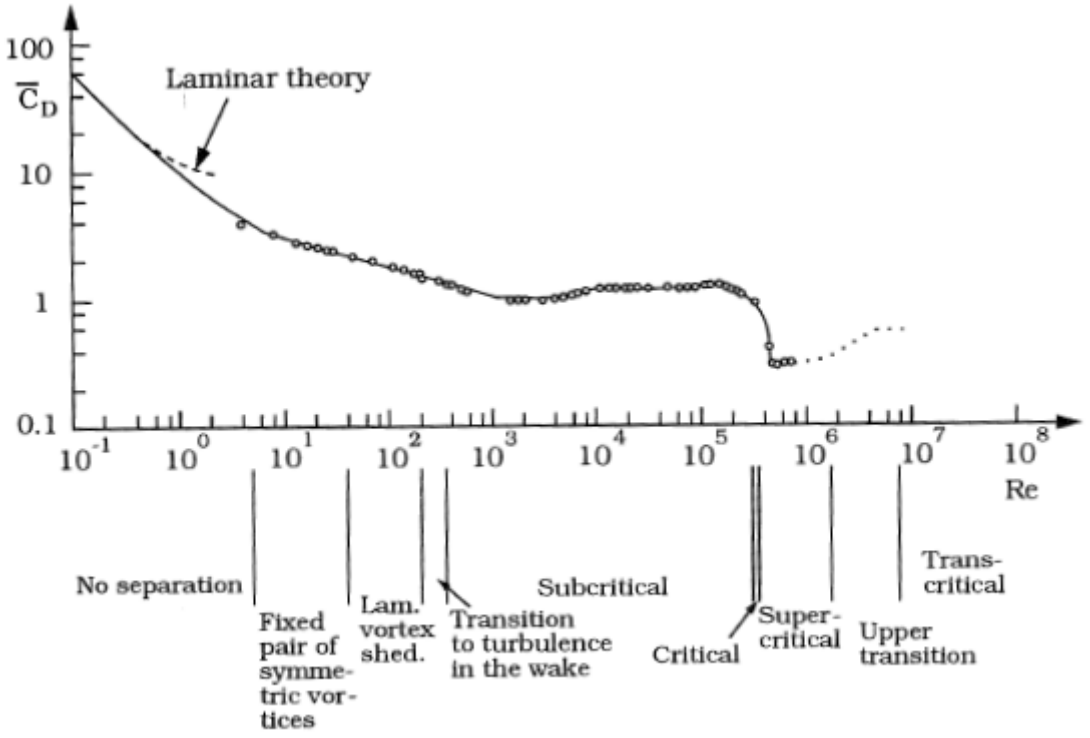

FIGURE 2.2: Drag coefficient as function of Reynolds number for cylinders. Taken from [Sumer and Fredsoe, 1997], originally from [Schewe, 1983]

$$Re = \frac{DU}{\nu} \tag{2.6}$$

Where C_D is the drag coefficient, D is the cylinder diameter, U is the flow velocity, and ν is the kinematic viscosity.

The drag coefficient for steady current is a function of the Reynolds number, which is illustrated in figure 2.2. When a cylinder is placed at an angle to the flow, the force normal to the cylinder may be calculated from equation 2.7. Since experiments show that the cross-flow principle is applicable, the drag coefficient can be taken as that for a cylinder normal to the flow. According to Sumer and Fredsoe [1997] this holds true for $\theta \geq 35^\circ$ under subcritical or postcritical flow only (see figure 2.3).

$$F_N = \frac{1}{2}\rho C_D D U_N^2 \tag{2.7}$$

2.2.2 Oscillatory flow and regular waves

For the situation that is being studied in this report, an approach to the drag loads regarding steady current is not representative. Since waves play an important role it may be assumed that forces can be better represented by assuming oscillatory flow. In addition to the Reynolds number which is important for steady flows, for oscillatory flows the Keulegan-Carpenter number becomes of interest.

The number is given by equation 2.8 and defines the ratio of the orbital motion of the water particles relative to the total width of the cylinder.

$$KC = \frac{UT_w}{D} \tag{2.8}$$

Where T_w is the oscillation period.

The total in-line force for a moving cylinder in an accelerated water environment is given by equation 2.9, which is known as the Morison equation [Morison et al., 1950]. In this equation the first term is called the drag term and the second term is called the inertia term, which is a combination of loading due to the added mass and the Froude-Krylov force. This holds true under the assumption that the body is small enough compared to the wavelength. Normally $\frac{D}{\lambda} \leq 0.1 - 0.2$ should hold, which is a reasonable assumption for the applications in this thesis. In this case the effect of diffraction can be neglected and only the Froude-Krylov force, which is an excitation force due to accelerated water particle motion, has to be taken into account. Note that the mass inertia of the cylinder itself and that of entrapped water as described in section 2.1 are not included here.

$$F = \frac{1}{2}\rho C_D D \left(U - U_b\right)\left|U - U_b\right| + \rho C_m A \left(\dot{U} - \dot{U_b}\right) + \rho A \dot{U} \tag{2.9}$$

Where C_m is the hydrodynamic masss coefficient, U_b is the cylinder body in-line velocity, and A is the cylinder area.
It should be noted that the maximum value of the drag related part has a 90° phase difference with the maximum value of the inertia related part. For small KC values the inertia components of the in-line force are large compared with the drag component. For large KC numbers flow separation occurs and the drag force becomes more important. The regime $0 < KC < 20 - 30$ is regarded as inertia-dominated whereas the regime $KC > 20 - 30$ is regarded as drag-dominated. When for simplicity the body motion is neglected, and the inertia terms are combined, they can be written as a function dependent of a new coefficient, $C_M = 1 + C_m$. The dependence of C_M and C_D on the Reynolds and Keulegan-Carpenter number is illustrated in figure 2.4.

For the effect of the angle of attack on the force coefficients the same reasoning seems to hold as for the case of steady flow. From experiments it is seen that for large KC numbers ($KC \geq 20$), C_D appears to be independent of the angle of attack θ. This can be explained by the fact that in this case the inertia forces are not important and the oscillatory flow approaches the steady current case, so the cross-flow principle holds (see section 2.2.1). It is also seen that for small KC numbers ($KC \leq 8$) the value of C_M approaches the value of 2, regardless of θ. This can be explained by the fact that for these small KC numbers the drag related forces are insignificant and the flow behaves like a potential flow. For the range $8 \leq KC \leq 20$ larger differences exist. This range falls in the regime where disruption of the transverse vortex street takes place. The differences may therefore be attributed to the fact that at an angle of attack deviating from 90° there exists a flow component parallel to the axis of the

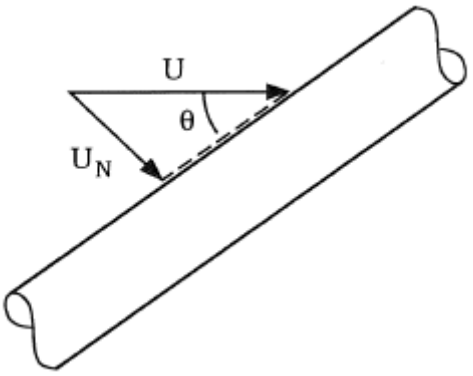

FIGURE 2.3: Definition sketch angle of attack. [Sumer and Fredsoe, 1997]

cylinder that disrupts the transverse vortex street.

2.2.2.1 Effect of ellepticity

Waves differ from plane oscillary flow by the fact that the fluid particles undergo an orbital motion, which for linear wave theory is given by equation 2.10 [Holthuijsen, 2007]. Research regarding the influence of the orbital motion on the force coefficients has been conducted for vertically and for horizontally placed cylinders with regard to the water surface. For vertical cylinders no proof is found that the force coefficients are influenced by the orbital motion, described by the ellipticity E which is given in equation 2.11.

$$\begin{aligned} u_x &= \hat{u}_x sin\left(\omega t - kx\right) \\ u_v &= \hat{u}_v cos\left(\omega t - kx\right) \end{aligned} \tag{2.10}$$

In which:

$$\hat{u} = \omega a \frac{cosh\left[k\left(d+\xi\right)\right]}{sinh\left(kd\right)}, \qquad \hat{v} = \omega a \frac{sinh\left[k\left(d+\xi\right)\right]}{sinh\left(kd\right)}$$

For deep water ($kd \rightarrow \infty$) this reduces to:

$$\hat{u}, \hat{v} = \omega a e^{kz}$$

When the total in-line force is described as a function of a coefficient however, it is clearly noted that the total force is hardly influenced by the ellipticity of the orbital motion. This holds true apart from very large ellepticities, $E \geq 0.7 - 0.8$ for which the total in-line force will be reduced by approximately 20-30% with respect to plane oscillatory flow.

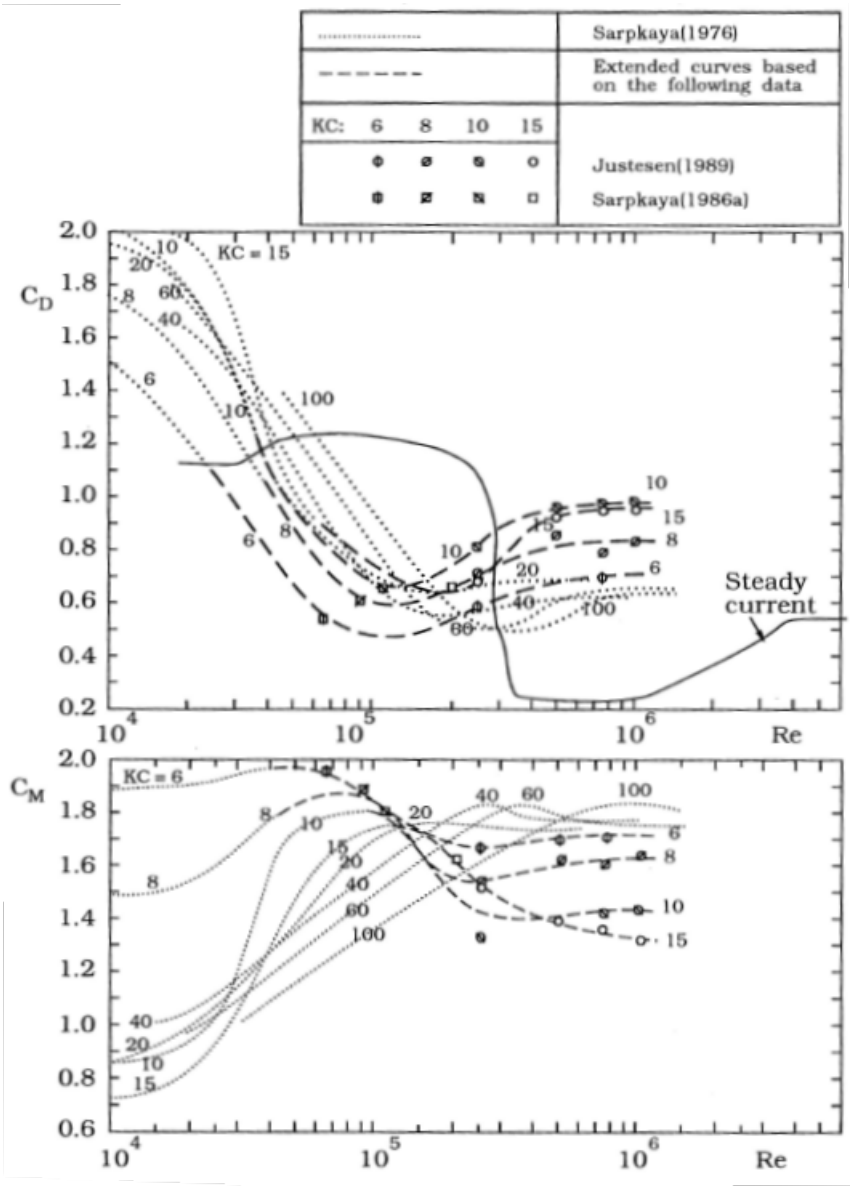

FIGURE 2.4: In-Line force coefficients for a free, smooth cylinder. Taken from [Sumer and Fredsoe, 1997], orginally from [Justesen, 1989, Sarpkaya, 1976, Scarpkaya, 1986, Schewe, 1983]

$$E = \frac{u_v}{u_x} \tag{2.11}$$

In experiments where the orbital motion was simulated by mechanically moving the cylinder, a systematic decrease in the total force with increasing ellipticity was found. It is however likely that this is caused by the fact that in these mechanical simulation no mass transport occurs and the moving cylinder encounters its own wake. When a small current or slight irregularities in the waves exist however this effect is expected to reduce. Although no clear influence of the ellipticity on the force coefficients is found it is noted that even when the force coefficients are available, the Morison equation alone does not provide an accurate approximation to the loading in case of horizontal cylinders in orbital flows with large KC numbers. This is because the vortex shedding that makes a large contribution to the loading with these KC numbers is not accounted for in the Morison equation. For the study

in this thesis however this effect is neglected. The time duration during which the cylinder is subject to drag loads is in the order of seconds. It is assumed that for the build up of vortices a greater time duration is needed.

2.2.3 Irregular waves

The reasoning as in the previous section is a close approximation of the situation encountered during marine transports, except for the fact that in real seas waves are highly irregular.

In figure 2.5 the results of a typical test are given for the force coefficients in irregular waves The Reynolds and Keulegan-Carpenter number can be described as their statistical analog root mean square values. It can be seen in the figure that the drag coefficient for irregular flow approaches to the value of 1 faster. It can also be seen that the inertia coefficient C_M shows an almost constant behaviour and actually reaches a maximum at about 1.6 instead of 2 for regular waves.

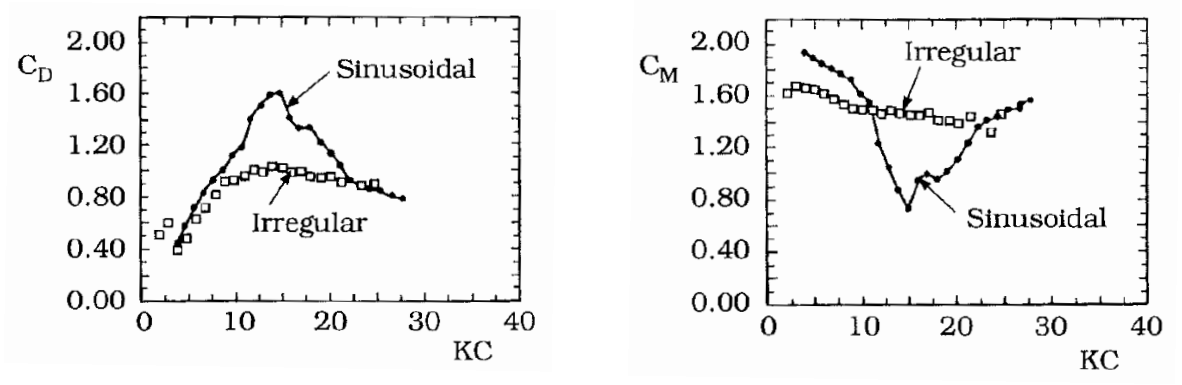

(A) Irregular Cd

(B) Irregular Cm

FIGURE 2.5: Typical force coefficients for irregular waves [Longoria et al., 1991]. Re/KC = 2323.

2.3 Water entry

Because the phenomenon of water entry of structures is a less commonly known matter, it will be described in a more detailed manner than the previous section here. Water entry of structures is also known as slamming and was first investigated by von Karman [1929]. He investigated the impact of floaters of seaplanes during landing. He did this by considering a horizontal cylindrical body with a wedge-shaped under surface and calculating the force acting between the body and the water. This force was calculated by assuming conservation of momentum between the water and the body. He used the high-frequency added mass limit for a plate of width $2c(t)$, where $c(t)$ is the distance from the center line of the wedge to the intersection line with the free undisturbed surface. He defined a slamming and pressure coefficient, which are given by equations 2.12 and 2.13 respectively. These can subsequently be used to determine the slamming force, which is given by equation 2.14. Wagner [1932] continued the research and took into account the uprise of water alonside the submerging body. This resulted in a larger half-width of the flat plate for the estimation of the added mass than von Karman used. Using simple geometric relations the wedge shape can then be transformed to a cylinder. This results in an initial slamming coefficients $C_s = \pi$ for the von Karman approach, and $C_s = 2\pi$ for the Wagner approach [Larsen, 2013].

$$C_s(t) = \frac{F(t)}{\rho V^2 R} \tag{2.12}$$

$$C_p(t) = \frac{p(x,t)}{0.5\rho V^2} \tag{2.13}$$

$$F_S = \frac{1}{2}\rho_w D C_s u^2 \Delta x \tag{2.14}$$

During the second world war the topic gained increasing attention due to the application of surface piercing projectiles such as torpedos. Because of this particular application most research in this period has concentrated on spherical and conical bodies. More recently water entry research has mainly continued to focus into two directions, namely that of wedge shapes and that of cylinders. The wedge shape is an approximation to investigate bow flare slamming of modern high speed vessels. The other direction, that of cylinders, originates from structural members of offshore platforms that are prone to wave loads in the splash zone, and from marine pipelines.

The problem of water entry of cylinders is considered more complicated, since the deadrise angle changes significantly in the initial phase of entry. Moran [1965] made an inventarisation of the studies on water entry up to that date. He found that almost all studies were conducted under the assumptions of irrotational and incompressible flow, and therefore are often aproached with potential theory. Also air density and surface tension are almost always neglected, gravity is assumed to be zero and cavitation is not accounted for. He concludes that upto 1965 it has not been possible to quantify the loads during water entry in a reliable way. Moran ascribes this to mathematical nature of the problem, in which nonlinear boundary conditions on a surface whose shape is unknown a priori must

be solved. Attempts in which these difficulties have been avoided by linearization have lead to unacceptable fictitious singularities at the intersection of the body and the undisturbed position of the free surface. Therefore they are not representative for the investigated phenomenon. Moran recommended to direct further studies for solving water exit and -entry problems at numerical methods.

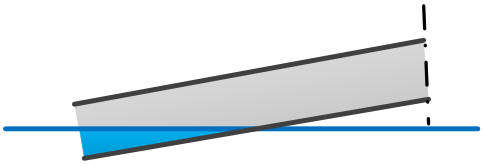

(A) Inclined water entry sketch. Side view.

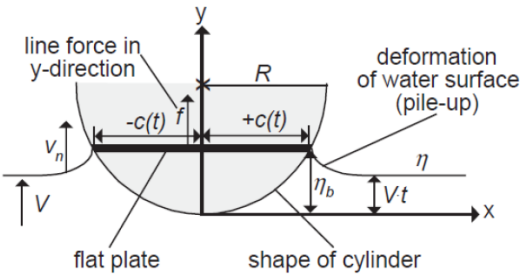

(B) Water entry sketch. Front view. [Ushanth, 2013]

FIGURE 2.6: Cylinder water entry sketches

2.3.1 Analytical & experimental appraoches

In the period between 1970 and 2000 still some effort was put in analytical but also experimental approaches. Miller [1977] found that however slam loading is of a transient nature, and a lot of other loads such as buoyancy, drag and inertia succesively act on the entering body, for Froude numbers greater than 0.6 slamming loads predominate. In 1979 he reviewed the results of eleven experiments. The results lacked complete agreement and showed a lot of scatter, which has been attributed to unknown inclinations of the cylinder axis at impact. Campbell and Weynberg [1980] were the first to conduct new experiments on the parameters effecting slamming in still, disturbed and aerated water. They used drop tests in such a way that the frequency response from the force transducers used was high enough whilst keeping the Froude number large enough. Campbell and Weynberg conclude their work with an empirical relation for horizontally impacting cylinders which is valid for high Froude numbers and small buoyancy, estimated at less than 5%. They state that this relation may also be used for inclined impact using strip theory and that inclined impact in disturbed water is similar to slams in calm water, however secondary excitations occur during the loading history that could produce greater dynamic structural responses. Additionally many photographs of their different experiments have been made available.
Their investigation however did not address the variation of water surface during impact. In an additional study Greenhow and lin [1983] covered this topic with experiments on the high speed entry of half buoyant and neutrally-buoyant cylinders. Also of these experiments many photographs have been made available.

Cointe and Armand [1987] made an attemt to compare the results from these experiments with existing analytical and numerical solutions. They conclude that some analytical solutions overestimate whereas some other underestimate the impact force. However, for all the analytical solutions the impact force rises instantaneously from zero to a finite value whereas in the experiments this is not

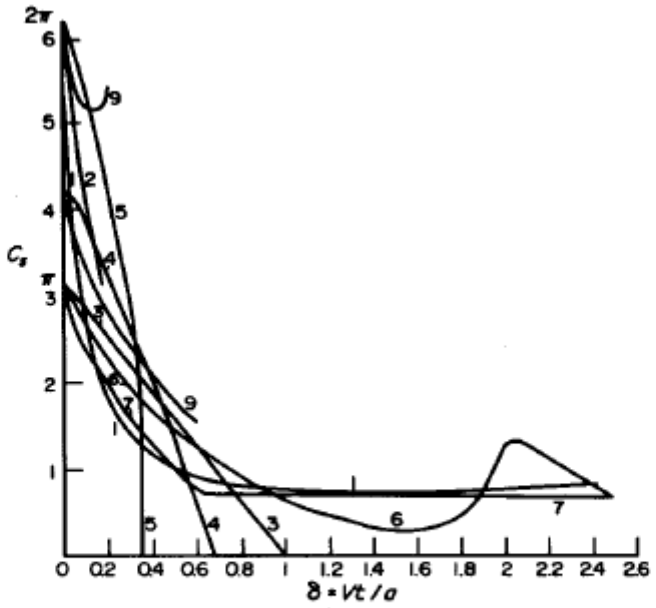

FIG. 9. Slamming parameter C_s against penetration depth. 1, experiments of Campbell and Weynberg (1980). 2, ellipse theory of Fabula (1957). 3, von Karman. 4, semi-Wagner. 5, Wagner (flat plate approaches). 6, von Karman (Kaplan and Silbert, 1976). 7, semi-von Karman. 8, semi-Wagner. 9, Wagner (exact body approaches).

FIGURE 2.7: Different historical solutions for C_s [Greenhow and Yanbao, 1987]

recorded (see figure 2.7). Cointe and Armand argue that phenoma such as air cushion formation, free-surface deformation prior to impact and entrapped gases might account for some finite rise time. They also state that the results of the numerical simulations regarded are in good agreement with the experimental data while the previously described effects are also neglected in these approaches.
Greenhow [1988] theoretically tried to solve the water surface variation and impact force problem as investigated in his experiments, but their data for impact pressure and water surface variation were inadequate. This was caused by the lack of pressure data experiments and the limited shooting speed of the cameras. To fill up this gap Lin and Shieh [1997] conducted new experiments using modern digital image techniques and a high speed data aquisition system. From their experiments they concluded that the early stages of impact cause a change in the water surface that can be divided into three phases. They name these phases the splashing effect, the rising along the surface of the cylinder effect, and the separation effect. Impact pressure occurs only in the splashing phase, except for peak pressure. They also found that increasing the impact velocity firstly causes the separation of the rising water surface to occur earlier and secondly that the water surface near the cylinder has a more obvious rising effect. Additionally they conclude that during the splashing phase nearly no water particles flow in the flow field.
Zhao [1996] in his research agree with the observations of Cointe and Armand and state that while the simplifications may be of negligible effect in the initial phase of water entry, they will be more important at a later stage after flow separation has occurred.

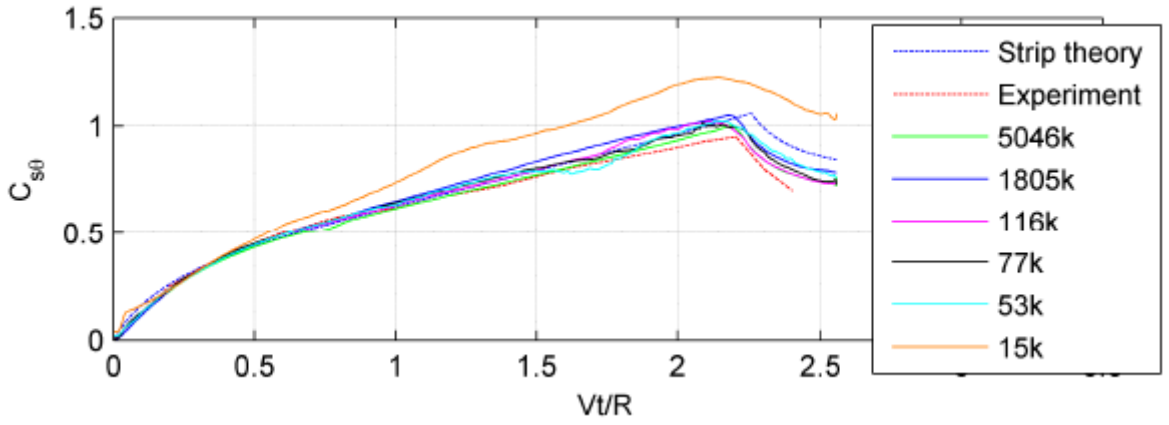

FIGURE 2.8: Slamming coefficient C_s as a function of dimensionless submergence for 8° inclined water entry of cylinders. A comparison between experiments [Campbell and Weynberg, 1980] and CFD computations [Larsen, 2013]. Taken from [Larsen, 2013]

2.3.2 Numerical approaches

As predicted by Moran, the main recent developments in the investigation of slamming took place in the field of numerical approximations. This was mainly caused by the fact that theoretical approximations failed accuracy and computer power increased rapidly. This combined with the fact that experiments are expensive and have the disadvantage of scaling effects set the direction of future developments. Experimental scaling is very difficult since in water entry problems viscous and nonviscous flow-separation both play a significant role since both are dependent on the squared velocity. For modelling viscous flow Reynolds scaling is required whereas for non-viscous flow separation Froude scaling is required.
Numerical attempts for cylinders were done by Greenhow and Moyo [1997], Moyo and Greenhow [2000], Battistin and Iafrati [2003], Seif et al. [2005], Sun and Faltinsen [2007], and Wang and Wang [2009].

Another field of interest that emerged from the numerical studies is the phenomenon of hydroelasticity. In these studies the influence of the deformation on the fluid flow and vice versa are studied. However this phenomenon is assumed to not play a role in this study, for the sake of completeness and because of possible interest of future studies reference is made to Chen and Yu [2009], Panciroli et al. [2012], Piro and Maki [2013], Yan and Liu [2011].
A very recent study on a topic comparable to the topic of this thesis was conducted by Larsen [2013]. He investigated the horizontal and inclined entry of cylinders using the commercially available CFD package Star-CCM+[1]. He compares his results with the results from Greenhow's experiments and concludes that the results are in good agreement. He however notes that there are still some problems with water that clings to the cylinder surface, resulting in reduced hydrodynamic forces. However the difference in results between the CFD calculations and the experiments are small, the forces calculated by Larsen are somewhat higher. It is not sure which results are most correct, but the range of errors falls within the possible error range of the experiment.

[1] `http://www.cd-adapco.com/products/star-ccm`

2.4 Water exit

The water exit problem has been studied in far lesser detail than the water entry problem up to now. Firstly this can already be seen in the study of Moran [1965]. The main part of his research is directed at water entry, but he states that under the assumptions that are made for the entry problem the fluid motion is reversible. Therefore the loading on the body in water exit differs only in sign from water entry. Any minor relaxation of one of the many assumptions however would immediately destroy the reversability, so this reasoning practically does not seem to hold. During their experiments on water entry Greenhow and lin [1983] also did experiments on horizontal water entry of half-buoyant en neutrally-buoyant cylinders of which photographs have been made available. Greenhow [1988] subsequently applied a numerical method of Vinje and Brevig [1981] to calculate the fluid loadings during water exit of a cylinder. He found that the calculations predict the involved effects well compared with experiments. These effects include lifting of the water above the cylinder and subsequent formation of thin layers, draw-down and rush-up of the free surface beneath the cylinder in which the rush-up terminates in localised breaking, and the formation of large regions of strongly negative pressures on the cylinder surface. When the forces on the body are compared with added-mass theory the agreements are not good.

In their study Greenhow and Moyo [1997] amongst others numerically investigate the water exit of a cylinder. They simplify the problem by only considering the inviscid loading but do not linearise the free surface or body boundary conditions. They also state that for cylinder exit gravity may not be ignored. They conclude that breaking can occur due to strongly negative pressures on the cylinder surface.

To quantify the loads involved with water exit, the same strategy that holds for water entry has been adopted. This is shown in equation 2.15, where the force due to water exit has been written as a function of the exit coefficient C_e. The added mass approach gives a coefficient shown in equation 2.16. Although the added mass approach and the experiments show no good agreement, their limit values are equal. These are $C_e = 1$ for a dimensionless submergence of about 1, and $C_e = 0$ for full emergence.

$$F_E = \frac{1}{2}\rho_w D C_e u^2 \Delta x \tag{2.15}$$

$$C_e = \frac{1}{\rho A v_e}\frac{dA_{33}^0}{dt} = -\frac{1}{\rho A_p}\frac{dA_{33}^0}{dh} \tag{2.16}$$

2.5 Motions of floating bodies

Floating bodies such as vessels and barges have six degrees of freedom. These are three translations of the body's center of gravity (COG) along the x-, y-, and z-axes called surge, sway, and heave respectively. And three rotations around these axes which are called roll, pitch, and yaw. These conventions are also illustrated in figure 2.9. For the analysis of the subject under study in this thesis, mainly the heave and pitch motion are of importance.

DOF	Motion description	Motion name	Force and Moment names	Linear and angular velocities	Positions and Euler angles
1	translation in x-direction	surge	F_x [N]	u [$\mathrm{m\,s^{-1}}$]	x [m]
2	translation in y-direction	sway	F_y [N]	v [$\mathrm{m\,s^{-1}}$]	y [m]
3	translation in z-direction	heave	F_z [N]	w [$\mathrm{m\,s^{-1}}$]	z [m]
4	rotation about x-axis	roll	M_x [Nm]	p [$\mathrm{rad\,s^{-1}}$]	ϕ [rad]
5	rotation about y-axis	pitch	M_y [Nm]	q [$\mathrm{rad\,s^{-1}}$]	θ [rad]
6	rotation about z-axis	yaw	M_z [Nm]	r [$\mathrm{rad\,s^{-1}}$]	ψ [rad]

TABLE 2.1: Motion notations

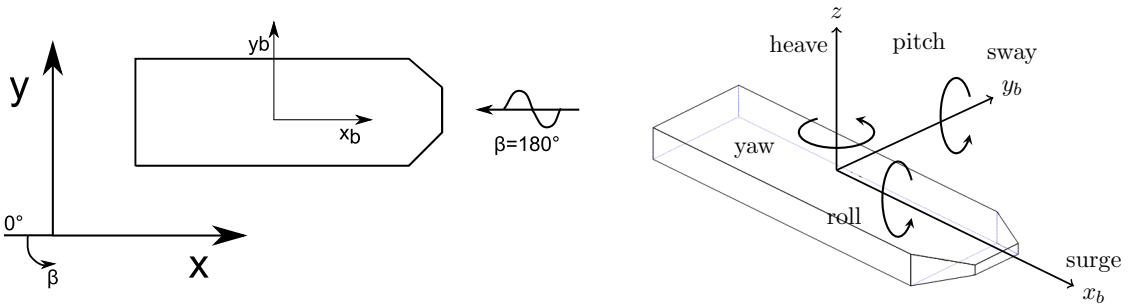

(A) Earth fixed

(B) Body fixed

FIGURE 2.9: Reference frames

The way in which motion characteristics of a floating body in general can be determined is further explained in appendix A. For simple geometries the hydrodynamic coefficients can be determined analytically. For more complicated geometries however an analytical approach becomes very cumbersome. For this reason the characteristics of a transport barge (H-405) have been determined using sophisticated modelling tools. How this is done and how this works is described in section A.0.2. In this study however motions and relative motions of specific points are of interest. In appendix B it is explained how the results of the general analysis can be used to describe specific parameters at the points of interest.

2.6 Conclusions regarding literature

It can be concluded from section 2.2 that upper limit values for the drag and inertia forces for this thesis are $C_d = 1$ and $C_M = 2$, however this seems to be a conservative assumption for cylinders in real seas. Since it is desireful to also take into account the inertia of entrapped water when the cylinder is submerged, and because usage of C_M does not take into account the body accelerations, it is decided to take into account the different contributions seperately. This means that a value of $C_d = 1$ will be used for the drag forces and $C_m = 1$ will be used for the added mass. The inertia of the pile itself, the inertia of entrapped water, and the Froude-Krylov force will be taken into account seperately.

It can also be stated that values for the slamming coefficient C_s for inclined water entry of cylinders is known for angles up to 8°. Since it is expected that this is not sufficient for the problem studied in this thesis, a proposal to extrapolate the available data is made here. For this the data from the experiments of Campbell and Weynberg [1980] are taken, since they show good agreement with recent numerical approaches. The peak values for the different impact angles start at $C_s = 5.15$ for zero submergence and converge to $C_s = 1$ for a dimensionless submergence greater than 1.25. This is shown in figure 2.10. Although a lot of conservatism is introduced by doing this, the complexity of the computations is reduced significantly by removing the dependence of the angle of inclination on the slamming coefficient.

Because of lacking knowledge water exit effects are neglected in this thesis. As a compensation the drag force is considered to be acting on the entire cylinder untill complete emergence, which is actually the same as taking the limit value for horizontal exit of $C_e = 1$. A recommendation is to further investigate this. Possible inertia effects of water left entrapped in the cylinder while emerged will be evaluated in a later analysis.

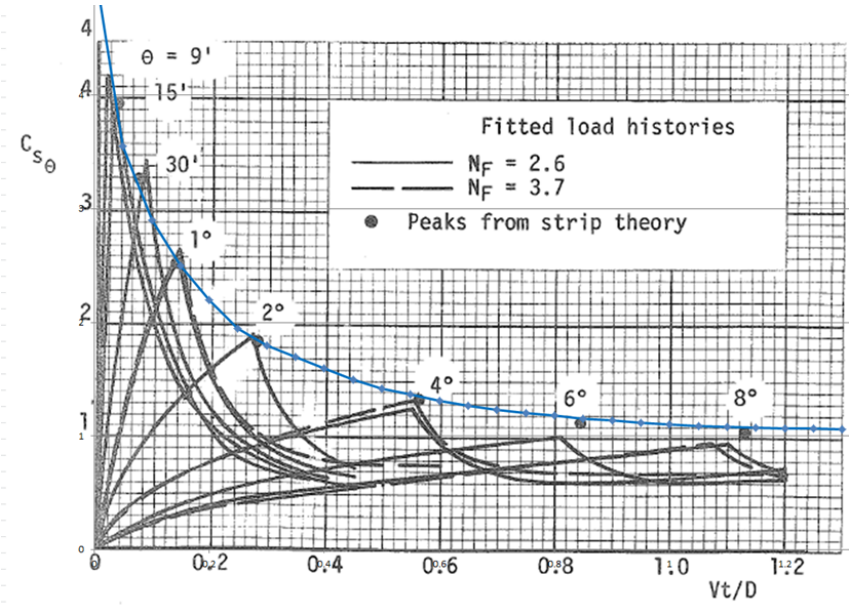

FIGURE 2.10: Extrapolation of slamming coefficient values

In which:

V = Cylinder downward velocity [m/s]

t = time, starting at first moment of impact [s]

D = Cylinder diameter [m]

In this way the x-axis of figure 2.10 represents the submergence of the lowest point of the cylinder divided by the diameter of the cylinder.

Chapter 3

Methodology

In this chapter the methodology with which the research has been approached will be outlined. First an analysis of the motions is given, since this forms the base of the problem. This analysis is split up into a brief description of barge motions, the description of the sea surface level, and concluding an analysis of the relative motions of the two former components. Following, a brief explanation is given of the current engineering method with which the involved loads are determined. Then ultimately two new methods are introduced that implement the physical loading mechanisms that are described in chapter 2.
The first of these two new methods is a quasi-stationary approach from which the acting forces are determined by means of four characteristic quasi-stationary situations. The parameters required are determined from a spectral analysis of the relative motions. In chapter 4 this approach is worked out for a case study and it will become clear that this approach includes many (conservative) assumptions. Therefore a more elaborate approach is wishful. This is accounted for in the second out of the two new approaches, which consists of a more extensive segmented model. This model uses time-trace realizations from the relative motion spectra as input. This approach is introduced in section 3.4. A graphical overview of the approaches and methods used and how these relate to each other is given in appendix D.

All of analyses are determined for a survival condition of the marine transport. This means that it is assumed that the forward velocity of the barge equals zero for the design sea states. It might however be possible that at lower wave heights than the design wave height slamming occurs. In this case the barge will not be operating in a survival mode and therefore have a forward speed. The influence of this effect is discussed in chapter 6.

3.1 Motion Analysis

The motions of the oversized cargo relative to the body of water forms the base of all analyses in this thesis. Therefore first the manner in which these relative motions are analysed is explained here. First the motions of the barge itself will be outlined briefly. A more detailed analysis is to be found in appendix A. Following, the description of the sea surface will be explained. Finally, both elements are integrated into a description of relative motions.

3.1.1 Barge motions

The system of a floating rigid body can be modeled for each DOF by a mass-spring-damper system as is shown in figure 3.1a.

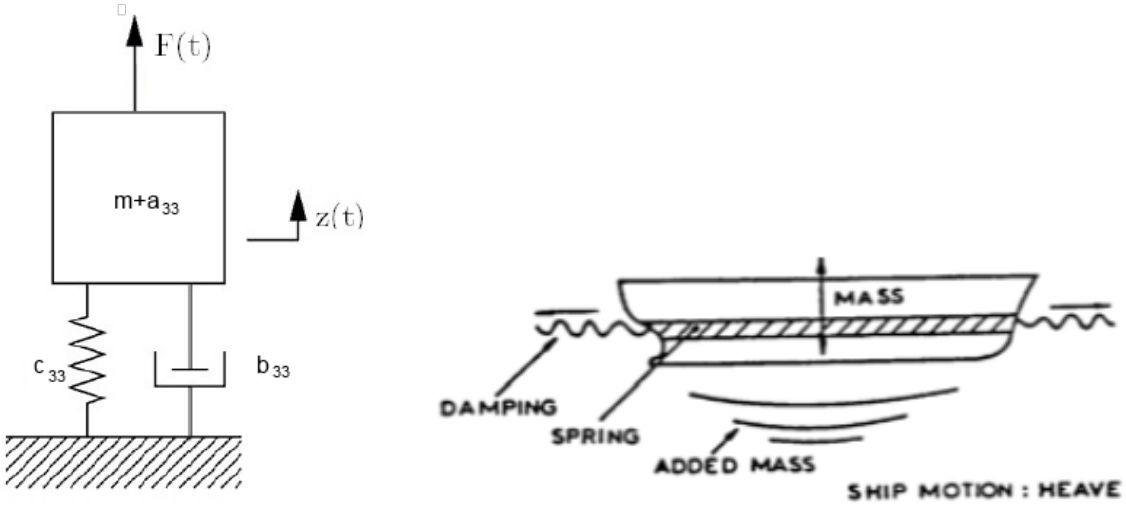

(A) Mass spring damper system (B) Ship motion resistance terms. From Journee and Massie [2001].

FIGURE 3.1: Schematisation of ship motions

As an example, equation 3.1 gives the equation of motion for heave.

$$(m + a_{33})\,\ddot{z} + b_{33}\dot{z} + c_{33}z = F \tag{3.1}$$

This equation can be expanded to all DOF's as is shown in matrix notation in equation 3.3. This equation of motion is coupled, which means that a motion in one direction can influence a motion in another direction. The result is that there are non-zero terms off the diagonals of the hydrodynamic coefficient matrices.

$$\underline{M}\ddot{\mathbf{s}} + \underline{B}\dot{\mathbf{s}} + \underline{C}\mathbf{s} = \mathbf{F} \tag{3.2}$$

	$\underline{M}$	=	Mass and frequency dependent added mass matrix
	$\underline{B}$	=	Frequency dependent damping matrix
In which:	$\underline{C}$	=	Stiffness matrix
	F	=	Wave excitation force
	s	=	Displacement vector

The forcing F is caused by a summation of the incident wave force (Froude-Krylov force) and diffraction forces. The response includes a number of terms that are sketched in figure 3.1. First, these are the in-phase hydrodynamic- or added mass that was already introduced for cylinders in chapter 2, and the out of phase radiation damping. Radiation damping is a form of damping in which energy is dissipated by radiating surface waves. These waves will be of importance in the analysis of the sea surface elevation in the next section. Both these latter two terms are frequency dependent. The hydrodynamic stiffness is caused by the displaced volume of water and therefore is a constant, assuming constant barge draft. The hydrodynamic coefficients and force terms can be determined by various methods. In this thesis 3D potential software WAMIT is used. For an in-depth analysis reference is made to appendix A. In this appendix also the frequency dependent values of the hydrodynamic coefficients are given.

When a steady state solution of equation 3.1 is regarded, the response z can be given as a function of the excitation F. Equation 3.3 gives this ratio, which is called RAO, for the heave motion of the barge. Because the forcing and the hydrodynamic coefficients are frequency dependent, and the forcing is additionally also dependent on the wave direction, the RAO is dependent on wave frequency and direction as well.

$$RAO(\beta,\omega) = \frac{\hat{z}}{\hat{\zeta}} = \frac{F}{\sqrt{\left(c_{33} - \left[m + a_{33}\right]\omega^2\right)^2 + \left(b_{33}\omega\right)^2}} \tag{3.3}$$

In which:

$\hat{z}$	=	Amplitude of heave motion		m	=	Mass of barge + cargo
$\hat{\zeta}$	=	Amplitude of incident wave		a	=	Added mass
F	=	Wave exciting force		ω	=	Excitation frequency
c	=	Spring coefficient		b	=	Damping coefficient

The RAO's and phase shifts are dependent on the excitation frequency and wave heading, and are given for all six DOF's for eight different wave headings in appendix A. A more extensive derivation of the RAO is also given in this appendix. Because the RAO's are a linear transfer function from incident wave amplitude to motion amplitude, they can be used to to determine the relative motions as follows in section 3.1.3.

3.1.2 Determination of the free surface level

The sea surface elevation at specific points in the fluid domain can also be described as a function of the incident wave. In this respect the analysis is similar to the analysis of the barge motions. The amplitude and phase shift of the sea surface elevation at a certain location can be determined with or without taking the effect of the presence of the barge into account. This is referred to as the disturbed or undisturbed approach respectively.

3.1.2.1 Undisturbed Approach

The undisturbed approach for determining the sea surface elevation is applied in the current engineering method for determining the loads on the oversized structure. In this thesis linear wave theory for deep water is applied, and it is assumed that wave energy dissipation can be neglected. Therefore, when the presence of the barge is not taken into account, the amplitude of the sea surface level at a location of interest will equal the amplitude of the incident wave. The phase shift with regard to the wave origin will be dependent on the horizontal distance between the wave origin and the POI, and on the wave frequency. This is illustrated in figure 3.2, where the wave origin is chosen at the COG of the barge.

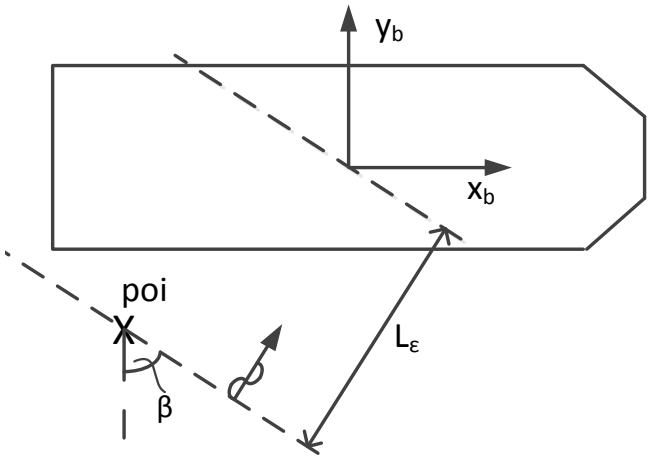

FIGURE 3.2: Top view of horziontal distances between a POI and the wave origin

The distance L_ε is the horizontal distance between the wave origin, which is chosen at the origin of the barge axis system. This distance can be determined with equation 3.4.

$$L_\varepsilon = x_{poi} \cdot \cos(\beta) + y_{poi} \cdot \sin(\beta) \tag{3.4}$$

The analyses are conducted for deep water. Therefore the wave length λ can be computed from the wave frequency by the deep water dispersion relation that is stated in equation 3.5.

$$\lambda = \frac{g}{2\pi} T^2 \tag{3.5}$$

$$k = \frac{2\pi}{\lambda} \tag{3.6}$$

Using a transformation from wave length to wave number (see equation 3.6), the phase shift with regard to the wave origin can then be found by equation 3.7

$$\varepsilon_{\eta\eta_0} = -k \cdot L_\varepsilon \tag{3.7}$$

A more comprehensive approach is introduced below, in which the effects of wave diffraction and radiation are taken into account

3.1.2.2 Disturbed approach

A more detailed way of describing the sea surface elevation at specific points is achieved when the presence of the barge is taken into account. Because the barge dimensions are significant relative to commonly encountered wave lengths, the incident wave will be (partially) reflected and diffracted such that a scattered wave field is generated. Because the extent in which the waves are hindered greatly dominates the result, the amplitude and phase shift of the sea surface elevation at specific points is dependent on the wave heading and frequency relative to the submerged dimensions of the barge.
Secondly, the motions of the barge cause wave radiation. These radiated waves originate from the damping that is described in section 3.1.1. The radiated waves also contribute to the total sea surface elevation at a specific point.

As is mentioned in section 3.1.1, the hydrodynamic coefficients are determined by means of 3D potential theory. An advantage of this technique is that it is possible to determine the fluid pressures at specific points in the surrounding of the barge as well. The actual sea surface elevation can then be determined from the fluid pressure.

As is extensively explained in appendix A, the space-dependent part of the velocity potential is given by equation 3.8.

$$\phi = \phi_D + i\omega \sum_{j=1}^{6} \eta_j \phi_j \tag{3.8}$$

Where ϕ_{1-6} are the contributions of the potentials of wave radiation, induced by the motion of the barge in the corresponding degree of freedom. Additionally, $\phi_D = \phi_0 + \phi_7$, which is the contribution of the incident wave and the diffraction of this wave due to the presence of the barge.

The amplitude $\hat{\eta}$ and phase shift $\varepsilon_{\eta\eta_0}$ of the surface elevation at a point relative to an incident wave can then be found by regarding the velocity potential for the boundary condition stated in equation 3.9.

$$\eta = -\frac{1}{g}\left(\frac{\partial\phi}{\partial t}\right)_{z=\zeta} \tag{3.9}$$

The effect of wave diffraction

When equation 3.8 is regarded just for ϕ_D, the effect of wave diffraction can be investigated. By combining the real and imaginary parts of the remaining equation evaluated for the boundary condition stated in equation 3.9, the amplitude and phase shift of the free surface with regard to the undisturbed wave can be caculated. In figure 3.3 examples of the sea surface amplitude with taking the effect of diffraction into account are shown for two different wave frequencies at a wave heading of 180°. The amplitudes are evaluated for field points at a grid size of $5x5$ m.

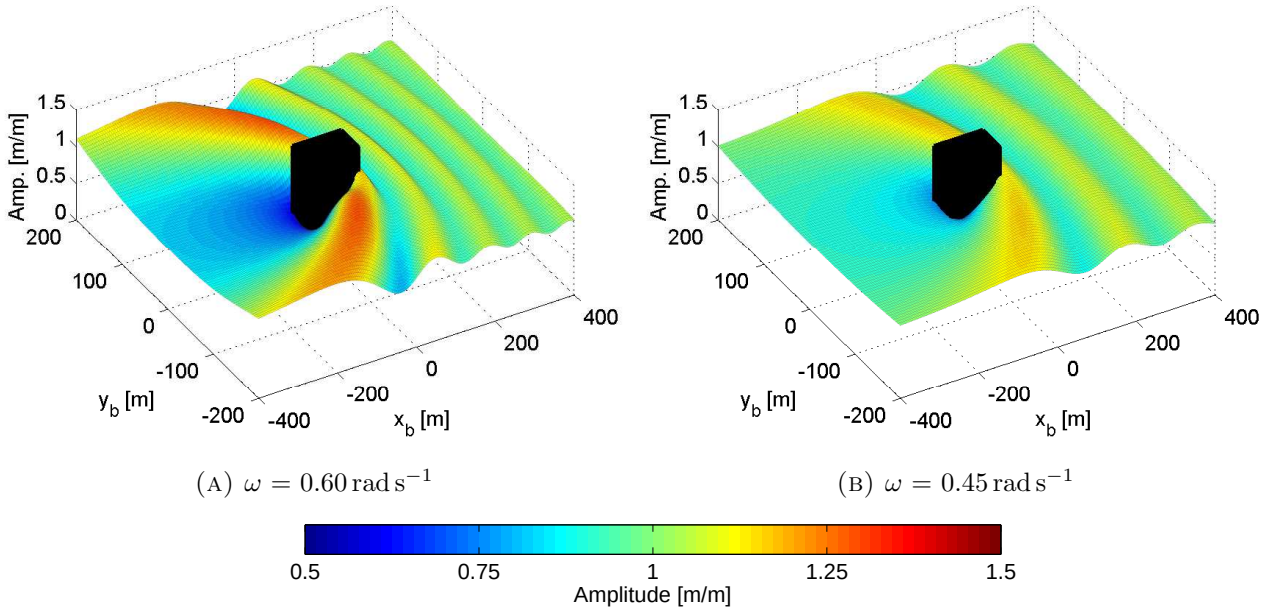

(A) $\omega = 0.60\,\mathrm{rad\,s^{-1}}$ (B) $\omega = 0.45\,\mathrm{rad\,s^{-1}}$

FIGURE 3.3: Surface elevation amplitudes with wave diffraction for $\beta = 180°$

In this figure the diffraction of the incident wave is clearly visible. It can be seen that for a wave at a heading of 180° a standing wave pattern in front of the barge is created. Due to the fact that the wave is just partly reflected, the minimum amplitude of 0 and maximum amplitude of 2 are not fully reached. It is also clearly visible in this picture that at this wave heading a wake is formed behind the barge stern, where the amplitude is lowered significantly.
For a wave heading of 0° however, the standing wave pattern will develop at the barge stern, which is exactly the place of the oversized cargo. Therefore the wave heading will not only affect the absolute barge motions, but also the sea surface elevation. The influence of the wave heading is shown in appendix B in figure B.1 and figure B.2.
The influence of the wave length with regard to the barge dimensions is also clearly visible. For a wave length of about 4.75 times the width of the barge (figure 3.3b the scattered wave field is much

more expressed than for a wave length of about about 8.5 times the barge width (figure 3.3b). The influence of wave heading and frequency on the amplitude and phase shift is taken into account for the determination of the relative motions in section 3.1.3.

The effect of wave radiation

In section 3.1.1 it was briefly explained that the damping term in the equation of motion originates from radiation damping. This means that the motion of the barge is damped by radiating energy to the surrounding in the form of surface waves. Clearly these waves will influence the sea surface level. In the same manner as is explained in section 3.1.2.2, the amplitudes and phase shifts of the sea surface elevation at field points can be determined. Now however equation 3.14 is evaluated for the potentials correspondig to the six modes of motion (ϕ_1 up to and including ϕ_6).

The amplitudes of the radiated waves behind the stern of the barge ($y_b = 0$ and $x_b < -61$), is largest for the heave and pitch motion. These are exactly the two relevant motions that also cause the vertical displace of the cargo. As an example, the amplitudes of the radiated waves due to these two motions at a frequency of $0.60\,\mathrm{rad\,s^{-1}}$ are given in figures 3.4a and 3.4b respectively. The amplitudes in these figures are scaled relative to a unit amplitude of the corresponding motion at the same frequency. The amplitudes and phase shifts of the radiated waves for all six DOF's are given in appendix B in figure B.3 and B.4.

The contributions of the radiated waves due to heave and pitch and their are taken into account in the analysis of the relative motions in section 3.1.3.

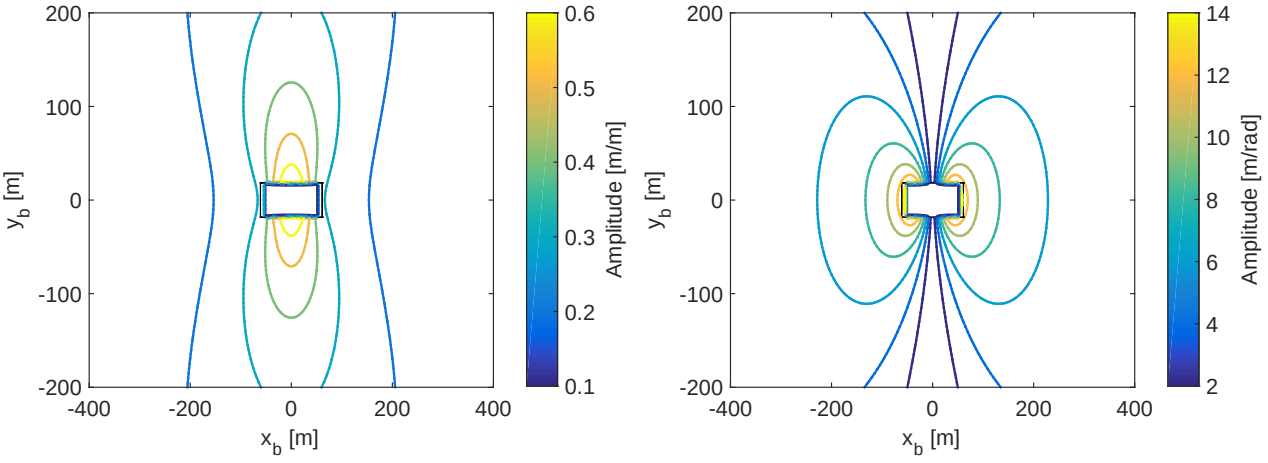

(A) Amplitude of radiated waves per meter of heave motion at $\omega = 0.60\,\mathrm{rad\,s^{-1}}$

(B) Amplitude of radiated waves per radian of pitch motion at $\omega = 0.60\,\mathrm{rad\,s^{-1}}$

FIGURE 3.4: Amplitudes of radiated waves due to heave and pitch at $0.60\,\mathrm{rad\,s^{-1}}$ relative to a unit amplitude of the corresponding motion

The combined effect of wave diffraction and radiation

The above metioned contributions of wave diffaction and radiation on the sea surface level have all been determined following linear wave theory. Therefore the total amplitude of the sea surface at a specific point can be found by complex superposition of the different contributions. Since the amplitudes and phase shifts of the radiation components are given relative to their corresponding motion, whereas the diffraction components are given relative to the incident wave, the radiation components have to be corrected for this. To be able to relate the total sea surface elevation at a point to the incident wave, given a wave heading and frequency, the amplitudes of the radiation components are multiplied with the amplitude of the corresponding motion per wave direction and frequency. The corresponding phase shifts are added. In this way a total sea surface elevation at specified points can be found as a function of the incident wave. This is shown in equation 3.10.

$$\hat{\eta}cos(\omega t + \varepsilon_{\eta\eta_0}) = \hat{\eta}_d cos(\omega t + \varepsilon_{\eta_d\eta_0}) + \hat{\eta}_{\phi_3}\hat{z}cos(\omega t + \varepsilon_{\eta_{\phi_3}z} + \varepsilon_{z\eta_0}) + \hat{\eta}_{\phi_5}\hat{\theta}cos(\omega t + \varepsilon_{\eta_{\phi_5}\theta} + \varepsilon_{\theta\eta_0}) \quad (3.10)$$

In this equation all amplitudes and phase shifts are dependent on wave heading and frequency. The amplitude and of the total disturbed sea surface at a specific points can then be found by combining the real and imaginary parts of equation 3.10. The modulus gives the amplitude $\hat{\eta}$ and the angle gives the phase shift $\varepsilon_{\eta\eta_0}$.

3.1.3 Relative vertical motions

The description of the relative vertical motion of the structure with regard to the sea surface is given in this section. In figure 3.5a the definitions that are used in the description of the relative motion are illustrated.

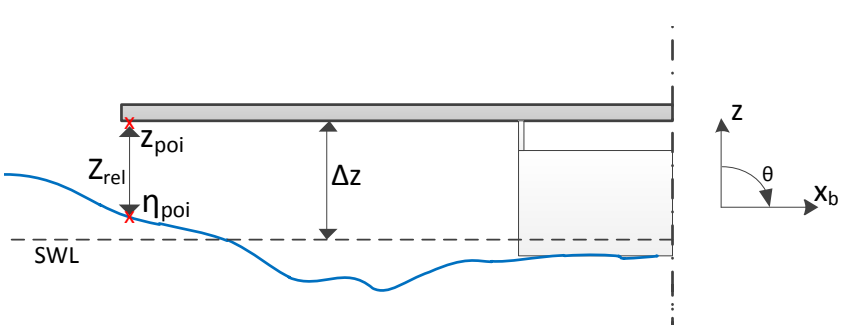

(A) Definition sketch of relative positions



(B) Detail of support structure

FIGURE 3.5: Relative motion definition sketch and photographic detail of pile support structure at barge stern

In the simplified case that is considered in this thesis, in which an overhanging pile is placed on the x-axis of the barge reference frame with a rigid connection, only the heave and pitch motion of the barge will influence the vertical position of the point of interest. The linearized vertical motion of the POI can then be described by equation 3.11. From figure A.10 it can be seen that the maximum of

the pitch RAO is about $0.02\,\mathrm{rad\,m^{-1}}$. With a hypothetical wave height of ten meters, the maximum absolute pitch angle then becomes 0.2 rad. Since $\sin(0.2\,\mathrm{rad}) \approx 0.2\,\mathrm{rad}$, and a 10 m wave height can be seen as quite extreme, the assumption of linearized motions is justified. This also means that angles of attack of the submerged forcings are very small, and therefore only vertical directed forces are of relevance.

$$z_{poi} = z - x_b\theta \tag{3.11}$$

In which x_b is the x-coordinate of the POI in the barge reference frame, z is the heave motion and θ is the pitch motion.

To explain the motions, a monochromatic cosine wave with unit amplitude at a 180° heading as shown in equation 3.12 is assumed as the incident wave. The steady state vertical motion of the POI as a response to this wave can then be described by equation 3.13. In this equation the frequency ω equals the frequency of the incident wave.

$$\eta_0 = \cos(\omega t) \tag{3.12}$$

$$z_{poi} = \hat{z}\cos(\omega t + \varepsilon_{z\eta_0}) - x_b\hat{\theta}\cos(\omega t + \varepsilon_{\theta\eta_0}) \tag{3.13}$$

The amplitudes and phase shifts of the heave and pitch motion are frequency- and wave heading dependent and are determined by their RAO's as described in section 3.1.1. The values of the heave and pitch RAO's and phase shifts are given for frequencies from $0.2\,\mathrm{rad\,s^{-1}}$ to $2\,\mathrm{rad\,s^{-1}}$ and eight different wave headings in appendix B in figure A.8 and figure A.10 respectively.

When the sea surface elevation at the location of the POI is described with equation 3.14, the relative vertical motion of the POI and the sea surface at that location can be written as equation 3.15. This is illustrated in figure 3.5a.

$$\eta_{poi} = \hat{\eta}\cos(\omega t + \varepsilon_{\eta\eta_0}) \tag{3.14}$$

$$\begin{aligned} z_{rel} &= \eta_{poi} - z_{poi} \\ &= \hat{\eta}\cos(\omega t + \varepsilon_{\eta\eta_0}) - \hat{z}\cos(\omega t + \varepsilon_{z\eta_0}) + x_b\hat{\theta}\cos(\omega t + \varepsilon_{\theta\eta_0}) \end{aligned} \tag{3.15}$$

The amplitude and phase shift of the sea surface elevation at the location of the POI follow from one of the approaches as explained in the previous sections. The disturbed approach is used in both methodologies that are developed in this thesis.

The relative motion as described in equation 3.15 has been obtained by a linear superposition of harmonic motions. Therefore the resultant motion itself must be harmonic as well;

$$z_{rel} = \hat{a}\cos(\omega t + \varepsilon_{a\eta_0}) \tag{3.16}$$

By using complex addition, the relative equation of motion can be split as shown in equation 3.17.

$$\begin{aligned} Re(z_{rel}) &= \hat{\eta}\cos(\varepsilon_{\eta\eta_0}) - \hat{z}\cos(\varepsilon_{z\eta_0}) - x_b\hat{\theta}\cos(\varepsilon_{\theta\eta_0}) \\ Im(z_{rel}) &= \hat{\eta_0}\sin(\varepsilon_{\eta\eta_0}) - \hat{z}\sin(\varepsilon_{z\eta}) - x_b\hat{\theta}\sin(\varepsilon_{\theta\eta_0}) \end{aligned} \tag{3.17}$$

The amplitude and phase of the relative vertical motion can be found by combining the real and imaginary parts of equation 3.17. The modulus gives the amplitude of the relative motion and the argument gives the phase, as is shown in equation 3.18.

$$\begin{aligned} \hat{a} &= \sqrt{Re^2(z_{rel}) - Im^2(z_{rel})} \\ \varepsilon_{h\eta} &= \arctan\left({}^{Im(z_{rel})}/_{Re(z_{rel})}\right) \end{aligned} \tag{3.18}$$

It should be noted that since the amplitudes and phase shifts of the different components are dependent of the frequency and the wave heading, also the amplitude and the phase shift of the relative motion are dependent of these parameters.
The amplitude $\hat{a}$ can be used as a RAO, just as was done for the absolute vertical motion section 3.1.1. In figure 3.6 a comparison between the disturbed and the undisturbed approach for the RAO of the relative vertical motion is made. For this comparison a point placed 20 m behind the barge stern is chosen.

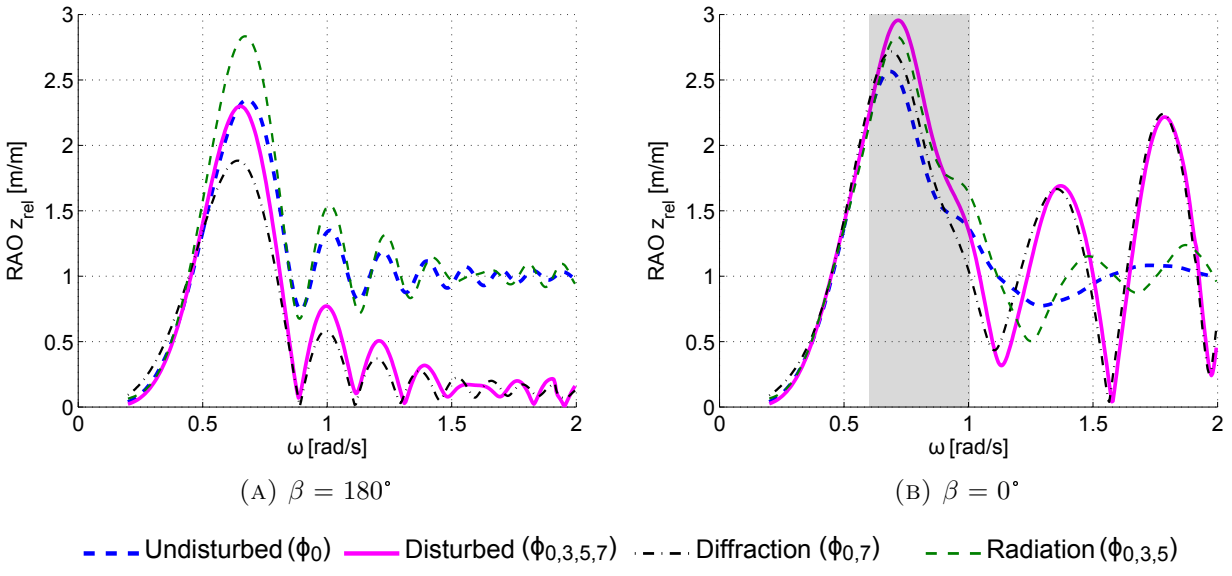

(A) $\beta = 180°$ (B) $\beta = 0°$

FIGURE 3.6: Comparison of RAO's of z_{rel} between the disturbed and undisturbed approach for a point at 20 m behind the barge stern

It can be seen in figure 3.6a that the RAO of z_{rel} is zero for very large wave lengths (small ω). For large wave lengths with regard to the barge length, diffraction effects do not play a role. Moreover the barge motions will follow the sea surface with negligible phase shift, so the relative motion tends

to zero.
Secondly, the RAO of z_{rel} is smaller for the disturbed approach with regard to the undisturbed approach for a 180° wave heading. The significant reduction in RAO due to the effect of wake forming (see diffraction line) however is almost levelled out for the peak frequencies due to the effect of radiated waves (see radiation line). For larger frequencies the effect of radiation diminishes because barge motions tend to zero, whereas the effect of diffraction increases for higher wave frequencies (shorter wave lengths).
Figure 3.6b shows the RAO of z_{rel} for a 0° wave heading. In this situation a standing wave pattern develops behind the barge stern, and the relative motion is actually larger for a disturbed approach for some ranges of wave frequencies. This can be explained by the fact that dependent on the wave frequency a node or antinode of the standing wave is located at the POI. This effect also occurs for a wave frequency range from approximately $0.60\,\mathrm{rad\,s^{-1}}$ (10.47 s) to $1\,\mathrm{rad\,s^{-1}}$ (6.28 s). This frequency range, that is shaded grey in figure 3.6b, includes wave frequencies that are commonly encountered during marine transports.

The RAO's of the relative vertical excitation, velocity and acceleration as a function of wave frequency for points with a stern overhang ranging from 5 to 60 m for eight wave headings are determined and given in figures B.8 to B.10.

3.1.4 Motion response in irregular waves

With the amplitudes of the relative vertical motions known, the response of the relative motions to a certain sea state can be found by using the RAO's as a frequency response function. The response spectrum of the relative vertical motion can be found by multiplying the wave variance density spectrum with the squared RAO, which is shown in equation 3.19. The RAO has to be squared because a variance spectrum is derived from the squared wave amplitude.

$$S_{z_{rel}} = \hat{h}^2(\beta, \omega)S \tag{3.19}$$

In wich S is the wave variance spectrum.

In the same way as for the relative vertical position, also a RAO and thus response spectrum for the relative vetical velocity or acceleration can be determined. This can be done by taking respectively the first or second derivative with respect to time of equation 3.16. The RAO's of the relative vertical position, velocity, and acceleration of POI's at distances up to 60 m behind the stern of the barge for different wave headings have been determined in the way described above and are given in appendix B.

Once a spectrum is known, its moments can be used to determine significant values. The i-th moment of a spectrum is defined by equation 3.20. The significant value, which is defined as the average of the $\frac{1}{3}^{\mathrm{rd}}$ highest values, can then be found from equation 3.21.

$$m_i = \int_0^\infty \omega^i \cdot S(\omega) d\omega \tag{3.20}$$

$$H_s = 4\sqrt{m_0} \tag{3.21}$$

Also, using the moments the mean zero crossing period of a wave spectrum can be found. This is shown in equation 4.6.

Just as is done for the wave height from a wave spectrum in equation 3.21, also the significant values of for example z_{rel} can be determined from the corresponding response spectrum. Using the response spectra, also time-traces of the relative motions can be constructed through an inverse discrete Fourier transform. This is further elaborated upon in chapter 4.

3.2 Current engineering approach

The current engineering method that is used is based on a number of load cases. A spectral analysis of undisturbed relative motions as explained above is used to obtain the required parameters to calculate the forces. Because this method is not a result of the work in this study, it is further described in appendix C. It should be noted however that not all relevant forcings are accounted for by these load cases, so the results give a distorted view when compared with the two approaches that are outlined below.

3.3 Quasi-stationary approach

In this section the first method that is developed to investigate the loads that are acting on the cylinder is introduced. For this first approach, a number of quasi-stationary orientations are sketched that are considered representative for governing loading situations. These orientations are based on the loading phenomena as described in chapter 2. The orientations are created in a way that for each loading mechanism an orientation exists such that its governing physical parameter is at a maximum. These parameter are obtained from a spectral analysis as is described in section 3.1.4. The orientations that have been identified are sketched below.

3.3.1 Maximum impact force

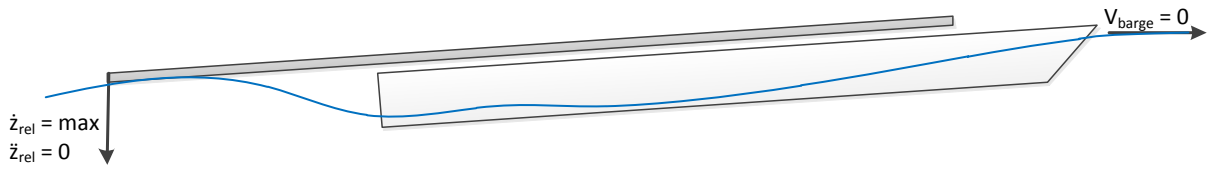

FIGURE 3.7: Maximum impact velocity

The first situation relates to the water entry load and is based on a maximum impact velocity. It is sketched in figure 3.7. The impact force due to water entry can be calculated by equation 3.22. Since the relative velocity of the pile and the water surface is squared in this equation the relative velocity is considered to be the governing parameter for this loading mechanism. The orientation sketched in figure 3.7 is therefore regarded such that the relative velocity is at a maximum. An additional consequence is that at maximum relative velocities, the relative acceleration is zero due to their 90° phase shift, which is explained in section 3.1. Therefore possible inertia related loads will not play a role in this situation. Additionally, Miller [1977] states that slamming loads predominate other loading mechanisms for $Fr > 0.6$. When the RAO's of the relative velocity are investigated, which are given in figure B.9, it can be concluded from the RAO's of the z_{rel}, that this condition is easily met when the relative motion has to exceed realistic values of initial gaps with the MSL.

$$F_s = \frac{1}{2}\rho_w D C_s \dot{z}_{rel}^2 l_{slam} \tag{3.22}$$

The values of $\dot{z_{rel}}$ and l_{slam} can be found from a spectral analysis. This is worked out for a case study in chapter 4.3.

3.3.2 Maximum submerged inertial forces

The second orientation represents inertia loads of submerged bodies and is sketched in figure 3.8. The situation is based on a maximum relative acceleration and is sketched in figure 3.8. A maximum

relative acceleration implies that the relative velocity is zero. For this maximum submerged state the acceleration of the cylinder is at a upward direction maximum and the acceleration of the sea surface at a downward directed maximum.

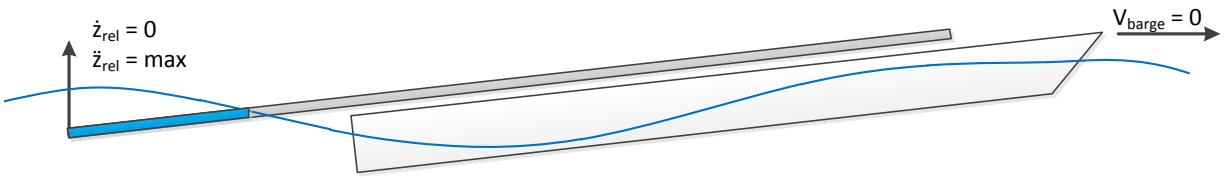

FIGURE 3.8: Maximum submerged acceleration

The forces that are maximized here are the inertia forces. These include the added mass, Froude-Krylov force and the mass inertia of entrapped water in the cylinder. In this situation, where the cylinder and the water body are both in motion, actually only the added mass is dependent on the relative acceleration. The Froude-Krylov force is dependent on the acceleration of the fluid and the entrapped water is dependent on the acceleration of the cylinder (see equation 2.9. Because a_{rel} is a superposition of both latter terms, and the maximum of this superposition is always larger than or equal to the maximum of its contributions, it is a safe assumption to use the relative acceleration for all three the load mechanisms. The total load in this orientation can therefore be described by equation 3.23.

$$F_i = \left(\rho_w \pi r_i^2 + (1 + C_m)\rho_w \pi r_o^2\right) \ddot{z}_{rel} \cdot l_{inertia} \tag{3.23}$$

3.3.3 Maximum drag force

The third orientation relates to drag loads and is therefore based on maximum submerged velocities. The situation is sketched in figure 3.9. For this orientation the maximum relative velocity is of interest. A consequence of this is that at maximum relative velocities, the relative acceleration equals zero due to their 90° phase shift. Because of this reason inertia related loads as described in orientation two do not play a role. The drag force can then be described with equation 3.24.

$$F_d = \frac{1}{2}\rho_w C_D D \dot{z}_{rel}^2 l_{slam} \tag{3.24}$$

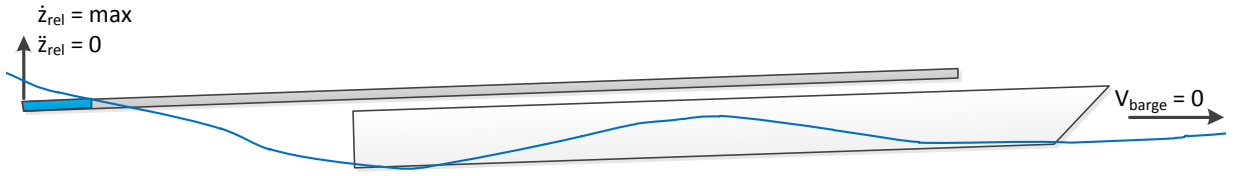

FIGURE 3.9: Maximum submerged velocity

3.3.4 Combined drag and submerged inertial forces

The two orientations that describe the maximum drag forces and maximum inertial forces, as shown above, are dependent on the relative velocity and the relative acceleration respectively. The total force is a combination of these two terms. In the above outlined orientations, one of these two forces always equals zero, because of the 90° phase shift between the relative velocity and the relative acceleration. Orientations in between these two extremes however are also loaded by the combination of drag and inertial forces, and in these situation neither of the two contributions equals zero. Therefore the combination of these two forces to a total force is investigated here.
The relative vertical velocity and the relative vertical acceleration as a linear function of an incident unit wave are described with equations 3.25 and 3.26 respectively.

$$v_{rel} = RAO(\dot{z}_{rel}) \sin(\omega t) \tag{3.25}$$

$$a_{rel} = RAO(\ddot{z}_{rel}) \cos(\omega t) \tag{3.26}$$

Then the drag force contribution is hypothetically described by equation 3.27, and the inertial force contribution with equation 3.28.

$$F_{drag} = A \cdot v_{rel}^2 \tag{3.27}$$

$$F_{inertial} = B \cdot a_{rel} \tag{3.28}$$

In which:
$A = \frac{1}{2}\rho_w D C_D l_{slam}$
$B = \left(\rho_w \pi r_i^2 + (1 + C_m)\rho\pi r_o^2\right) \cdot l_{inertia}$

The total force due to the combined contributions of drag and inertial forces can then be determined by equation 3.29.

$$F_{tot} = F_{drag} + F_{inertial} \tag{3.29}$$

In which the inertial force contribution is linearly dependent on the incident wave amplitude and the drag force contribution has a quadratic dependence. Additionally, both terms have a phase shift of 90°.
In governing situations, this summation of a linear and out of phase quadratic term is at a maximum. To gain insight in the behaviour of the maximum of this function, first the terms A and B are more closely considered. It is seen that when the amplitude B, of the inertial contribution is larger than the amplitude A of the drag contribution, the maximum amplitude of the combined contributions equals B. When the value of A exceeds the value of B, the maximum amplitude of the combined force converges to the amplitude of A for an increasing difference.
If A and B are now compared, and when it is assumed that: $C_D = 1, C_m = 1, l_{slam} = L_{inertia}$ and $r_i = r_o$ (slender body theory), it can be found that $A = 3\pi r B$. Since for this magnitude of difference, the convergence is very strong. Further it is noticed that in this analysis it is assumed that $RAO(\dot{z}_{rel}) = RAO(\dot{z}_{rel})$. In the figures appendix B it can be seen that is is roughly true, but that the values of $RAO(\dot{z}_{rel})$ are slightly larger than these of $RAO(\dot{z}_{rel})$. If this were to be included, the convergence would even be greater.
For the reasoning mentioned above it is assumed here that the maximum amplitude of the combined contributions of drag and inertia forces equals the maximum amplitude of the drag force.

3.3.5 Maximum emerged inertial forces

The fourth orientation represents inertia loads when the cylinder is filled with water during an emerged state of motion, also referred to as scooping. The situation is therefore based on a maximum vertical excitation, and thus a maximum vertical acceleration (see figure 3.10). In this situation, the excitation is maximum upward and therefore the acceleration is directed downwards. This induces an inertia-related load that is directed upward, that can be determined by equation 3.30.

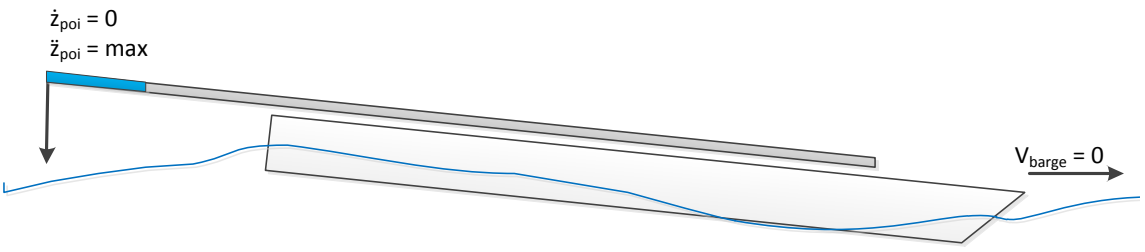

FIGURE 3.10: Maximum emerged acceleration

$$F_i = \rho_w \pi r_i^2 (\ddot{z}_{poi} + g) \cdot l_{inertia} \tag{3.30}$$

The forces resulting from these orientations can easily be found by the mentioned equations. Since the forces are assumed to be equally distributed over their acting lengths, the bending moment at the first support can be found by simply multiplying the total force with the distance from the support to the point of application of the force. In chapter 4, the results of this approach applied to a case study are discussed.

3.4 Segmented model approach

As is already mentioned in the introduction of this chapter, the second approach comprises a more detailed segmented model. In this model the cylindrical structure is divided into individual segments of finite length, for which the actual loading mechanisms and corresponding physical quantities are evaluated as a function of time. The total load as a function of time can then be found by a summation of the loads on every segment. A visual representation of this model is given in figure 3.11.

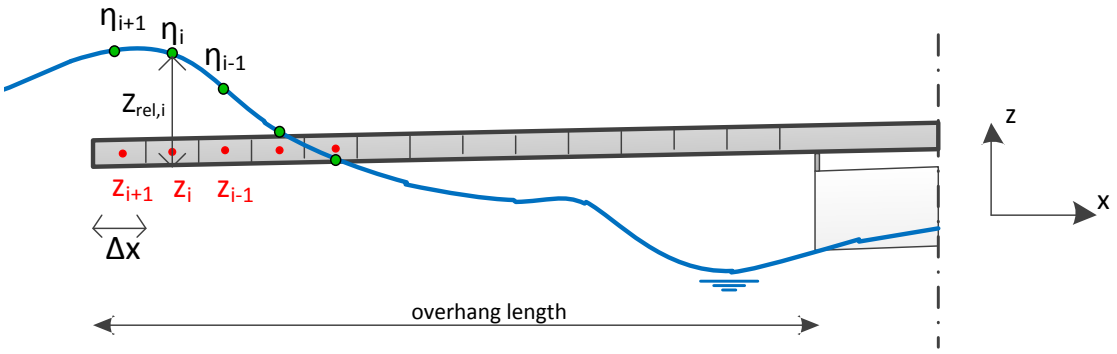

FIGURE 3.11: Visualization of segmented model

For every segment time-traces are generated for the vertical position, velocity, and acceleration of the cylinder and of the sea surface. These time-traces are realised from the response spectra by means of an inverse discrete Fourier transform that will be further described in chapter 4.
Because this segmented load load model is a product of the work in this thesis, it is validated by means of a number of characteristic situation in appendix 5. The developed source code is given in appendix E.

3.4.1 Loading states

The loading mechanisms on every segment are related to the state in which a segment abides. The states and their related loading mechanisms are described here below. A functional representation of how the model works is given in the flowchart in figure D.2.

3.4.1.1 Water entry state

The first state that a segment enters when the relative motion exceeds the initial gap with the SWL is the water entry state. The water entry state is the state in which the lowest point of the cylinder satisfies the condition stated in equation 3.31. This is also illustrated in figure 3.12.

$$0 \leq z_{rel} - \Delta z \leq 1.25D \tag{3.31}$$

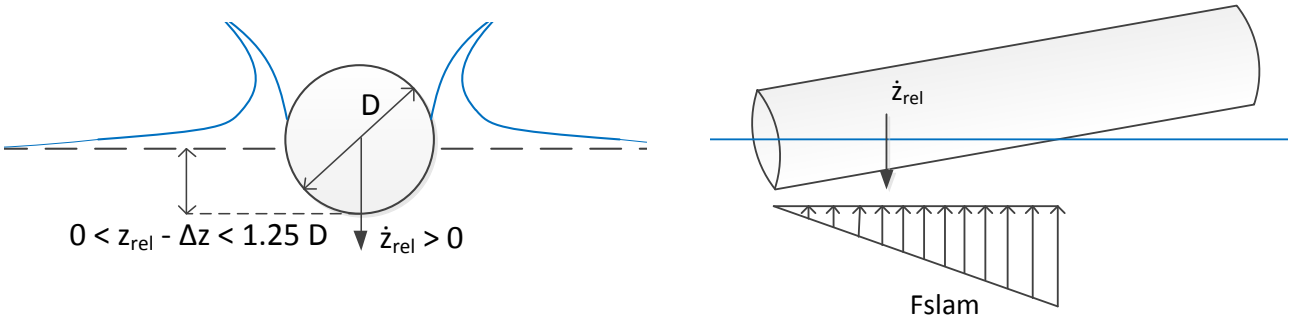

(A) Front view

(B) Side view

FIGURE 3.12: Sketched impression of position and loading during water entry state

As is mentioned in section 2.3, during water entry slam loads predominate for $Fr > 0.6$ [Miller, 1977]. The acting force due to slam loading can be calculated with equation 3.32.

$$F_{s,i}(t) = \frac{1}{2}\rho_w D C_{s,i}(t)\dot{z}^2_{rel,i}(t)\Delta x \tag{3.32}$$

In this approach $\dot{z}_{rel}$ and C_s are determined per time step for every segment i. The slamming coefficient C_s is dependent on the dimensionless submergence as is explained in section 2.6. The slamming coefficient has a very steep slope at low submergence values. With relatively high significant velocities and small cylinder diameters, it is possible that the first time step in which the segment is submerged already has passed the range of high coefficient values. Therefore the time step in this state is decreased with a factor ten by means of backward linear interpolation. More explanation of this on the influence of the result is given in chapter 4.

3.4.1.2 Drag downward state

Following the water entry state follows the drag downward state. This state is reached when the conditions stated in equation 3.33 are satisfied. In text this means that the dimensionless submergence should be greater than $1.25D$ and that the relative velocity should be directed downward. Since constant drag and added mass coefficients are used, there is no need for a refined time step here.

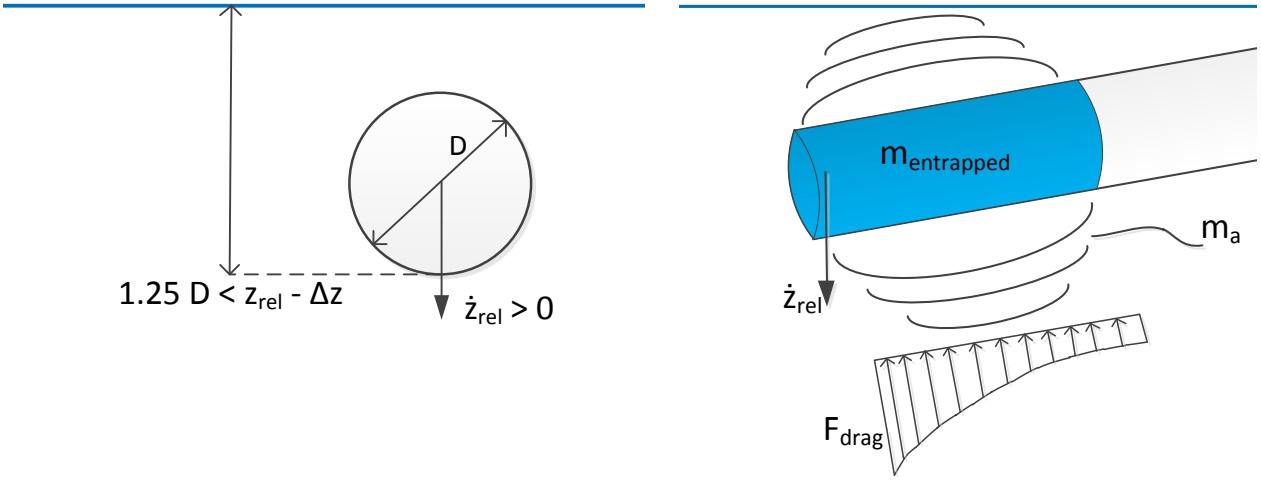

(A) Front view (B) Side view

FIGURE 3.13: Sketched impression of position and loading during drag downward state

$$1.25D < z_{rel} \text{ and } \dot{z}_{rel} > 0 \tag{3.33}$$

The total loading in this state is a summation of various in- and out of phase drag and inertia contributions. Because for every segment a time-trace is made, the total load is a summation of the different contributions in each time step. The loading terms are:

Drag Force

The physical mechanism of drag forces is extensively described in chapter 2 and is determined by equation 3.34. In this chapter it is also explained that a constant drag coefficient $C_d = 1$ may be used.

$$F_{d,i}(t) = \frac{1}{2}\rho_w D C_d \dot{z}_{rel,i}(t)\Delta x \tag{3.34}$$

Entrapped mass

The submerged part of the cylinder will flood during the water entry phase. The mass of this volume of fluid has mass inertia, and therefore exerts a force on the cylinder when accelerated. For a segment in a fully submerged state this force is described with equation 3.35.

$$F_{m,entrapped,i} = \rho_w \pi r_i^2 \ddot{z}_{poi,i}(t) \Delta x \tag{3.35}$$

Where r_i equals the cylinder inner radius.

Because the absolute accelerations are used in this equation, it is assumed that the entrapped water has no interaction with the surround fluid. For small diameter cylinders compared with the wave length this assumption seems valid, but is not validated.

Added mass

The phenomenon of added mass is extensively described in chapter 2. Its contribution may be calculated with equation 3.36. In chapter 2 it is also explained that an added mass coefficient $C_m = 1$ may be used.

$$F_{m,added,i}(t) = \rho_w \pi r_o^2 \ddot{z}_{rel,i}(t) C_m \Delta x \tag{3.36}$$

Froude-Krylov force

The Froude-Krylov force is a force caused by the pressure gradient in an accelerated fluid flow, such as in waves. The loading on a segment may be described by equation 3.37.

$$F_{FK} = \rho_w \pi r_o^2 \ddot{z}_\eta \Delta x \tag{3.37}$$

It should be noted that in all these force contributions, the effect of a decrease in the amplitude of the orbital water particle motions with increasing depth is not accounted for. This a conservative approach.

3.4.1.3 Drag upward state

The third state equals the second state in terms of load mechanisms but only differs by the direction in which the forces are acting. The condition that is satisfied to reach this state is given in equation 3.38. In text this means that the cylinder should be at least partly submerged, and that the relative velocity should be directed upward.

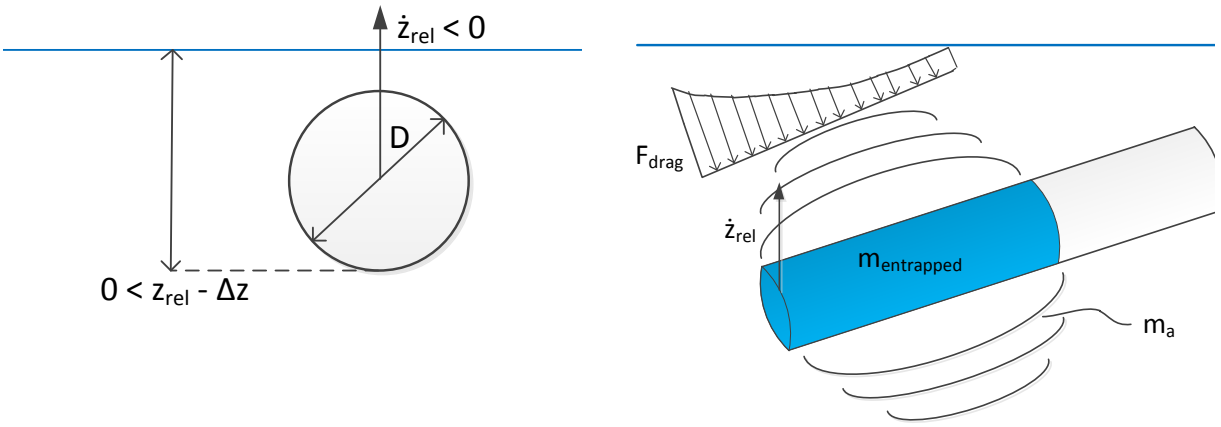

(A) Front view (B) Side view

FIGURE 3.14: Sketched impression of position and loading during drag upward state

In the last phase of this state, the cylinder is partly emerged. During this time the forces are determined as if the cylinder is still completely submerged. In chapter 2 it is explained that this is a loading upper limit.

$$0 < z_{rel} \text{ and } \dot{z}_{rel} < 0 \tag{3.38}$$

3.4.2 Resulting forces

The loading states that were described in the previous section are evaluated for every segment at each timestep. The total hydrodynamic load on the oversized part of the structure as a function is time is then found by summation of the contributions from all segments per time step. It is assumed in this study that the total vertical force is transferred through the structure to the supports as a static load. The total force can be described with equation3.39.

$$F_v(t) = \sum_{i=1}^{N} F_i(t) \tag{3.39}$$

The bending moment at the first support from a segmented model approach can be found by multiplying the force contribution from every segment with its corresponding distance to the support. This is written in equation 3.40. The definitions are sketched in figure 3.15.

$$M_s(t) = \sum_{i=1}^{N} F_i(t) x_{s,i} \tag{3.40}$$

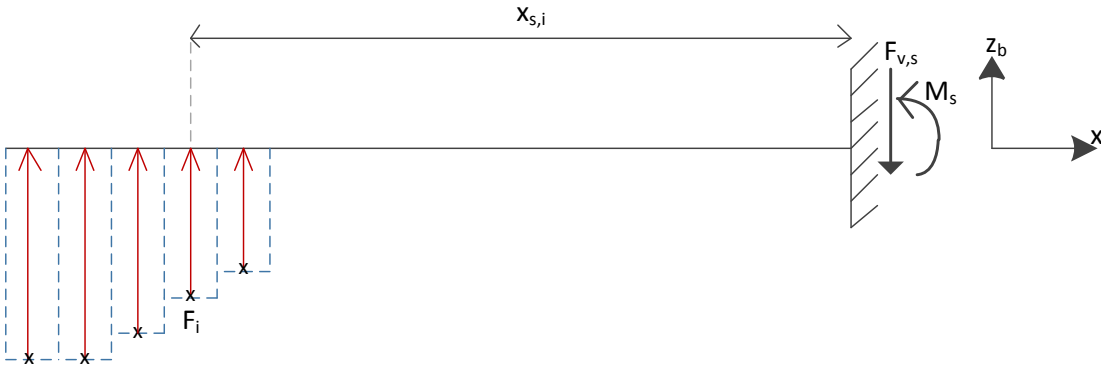

FIGURE 3.15: Bending moments at first support

Chapter 4

Simulations

In this chapter the methodologies as described in chapter 3 are elaborated. To be able to compare the methods that have been developed in this thesis, both are worked out for a case study that is described in section 4.1. Subsequently the segmented model is used to investigate if general conclusions can be drawn regarding parameters of interest, such as the total vertical load and bending moments as a function of wave height.

4.1 Case study description

To be able to compare the two described methods and assess their suitability, first a case study on which this comparison is based is formulated here. From the relative motion analysis in section 3.1.3 it becomes clear that the amplitude of the RAO of the relative motion has a peak at a wavelength of about 1.3 times the barge length (see figure B.8). The analyses are conducted for deep water conditions.

As the governing situations occur when the hydrodynamic forces are the largest, a case study in which the response is at a maximum is most interesting.
To simulate a realistic situation, not a monochromatic wave with its frequency equal to the peak frequency of the response is chosen. Instead a wave spectrum is used to simulate a random sea state, with its peak frequency T_p equal to the peak frequency of the response. In this case study eight wave headings will be considered, ranging from 0° to 315° with a 45° increment.

As a suitable case study a transport is chosen that was conducted from Italy to Ivory Coast in November 2014. Amongst others, the transport comprised jacket foundation piles, with a stern overhang of 22 m and an initial gap (Δz) of 5.43 m. The wave variance spectrum that is used is a Jonswap spectrum with a significant wave height $H_s = 6.3$ m and peak shape factor $\gamma = 3.3$.

$$S_{z_{rel}} = RAO^2_{z_{rel}}(\beta, \omega) \cdot S_w \tag{4.1}$$

Pile outer diameter:	2.13 m
Pile inner diameter:	2.04 m
Stern overhang:	22 m
Spectrum:	Jonswap, $\gamma = 3.3$
Design H_s:	6.3 m
Design T_p:	9.05 s - 13.75 s
Δz:	5.425 m

TABLE 4.1: Characteristics of the case study

The design significant wave height equals 6.3 m and according to design guidelines [DNV, 2014] the peak period of the spectrum should be chosen accordingly as stated in equation 4.2.

$$\sqrt{13H_s} < T_p < \sqrt{30H_s} \tag{4.2}$$

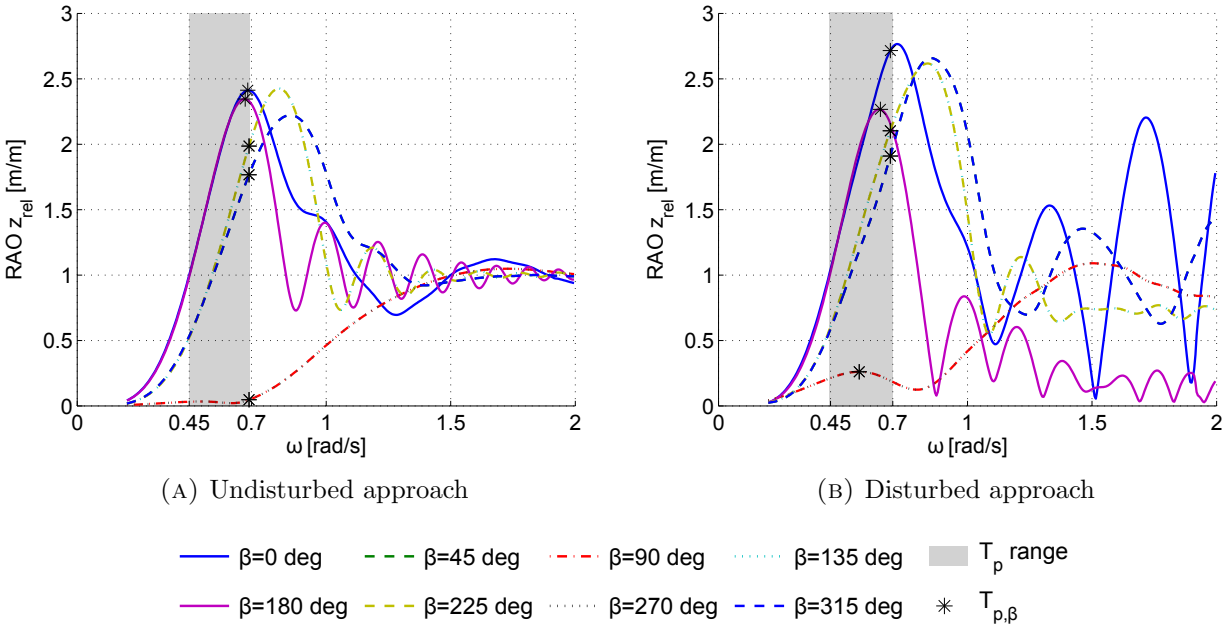

(A) Undisturbed approach (B) Disturbed approach

FIGURE 4.1: RAO of z_{rel} at 22 m behind stern for 8 wave headings

Figure 4.1 shows the RAO's of z_{rel} for different wave headings for the disturbed and the undisturbed approach. The period range according to DNV [2014] is shaded grey in these figures. For every wave heading the peak period of the wave spectrum is chosen to be the period at which the RAO of z_{rel} of the most outward POI is maximum in this period range. These periods are marked $T_{p,\beta}$ in figure 4.1.

The wave spectrum used for a 180° wave heading with disturbed approach is illustrated in the left plot of figure 4.2. This wave spectrum is a Jonswap wave spectrum as defined in equation 4.3. From this wave variance spectrum the response spectra for the relative motions, velocities, and accelerations can be determined by using the corresponding RAO's. This is shown in equation 4.1. As an indication of

the relative motion for this case study, the response spectrum of z_{rel} for the most outward point for a wave heading of 180° is shown in the right plot of figure 4.2.

$$
\begin{aligned}
S &= \frac{C \cdot H_s^2 \cdot \gamma^{\alpha}}{(\omega/\omega_p)^5} \cdot \exp\left(\frac{-1.25}{(\omega/\omega_p)^4}\right) \\
&\text{where} \\
\omega_p &= \frac{2\pi}{T_p} \\
\alpha &= \exp\left(-\frac{(\omega/\omega_p - 1)^2}{2\sigma^2}\right) \\
C &= \frac{5}{\frac{16}{T_p}\left(1.15 + 0.168\gamma - \frac{0.925}{1.909+\gamma}\right)2\pi} \\
\sigma &= \begin{cases} 0.07 & \omega \leq \omega_p \\ 0.09 & \omega > w_p \end{cases}
\end{aligned}
\tag{4.3}
$$

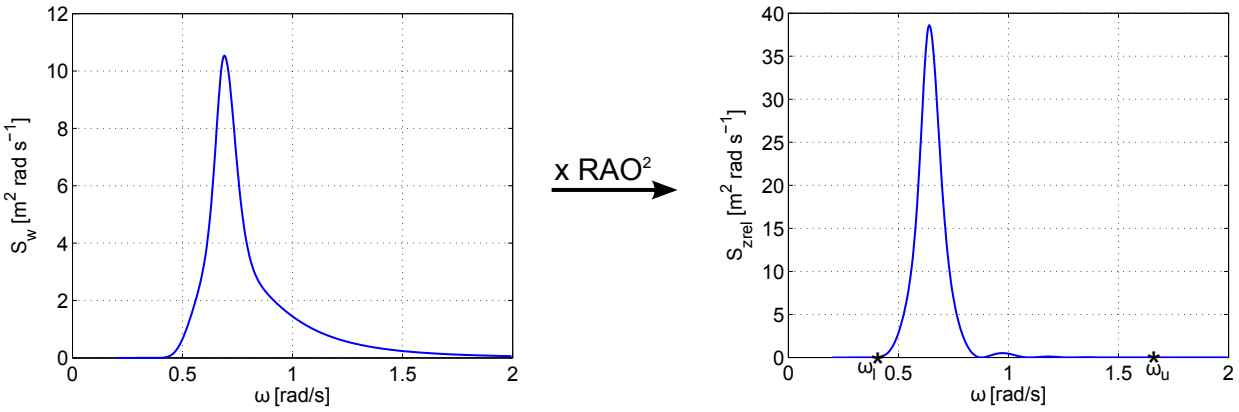

FIGURE 4.2: Left: Jonswap variance density spectrum, $\gamma = 3.3$, H_s =6.3 m.
Right: Response spectrum z_{rel} at 22 m overhang for $\beta = 180°$

.

The response spectrum for different wave headings and for different POI's or relative velocities or accelerations can be found by using the corresponding RAO in equation 4.1.

The significant values for the different components of the relative motion can be found using the moments of these response spectra, as is explained in section 3.1.4. The resulting values for this case study are given in table 4.2. Because the cargo is placed on the x-axis of the barge, and the geometry of the barge is symmetrical around this axis, the results for the significant amplitudes are also symmetrical.

The values in table 4.2 are significant values for a point at 22 m behind the barge stern. It strikes that the significant amplitudes for the disturbed approach are larger than the ones of the undisturbed approach, except for wave headings of 90°, 180°, and 270°. Wave headings of 90° and 270° are neglected in this reasoning for now because these values are so low for both approaches that no impact is expected. As is explained in section 3.1.3, wave radiation due to the barge motions is a factor that contributes to the sea surface elevation that is not taken into account in the disturbed approach. This explains part of the larger significant values. Additionally also wave diffraction contributes, which for

β	[°]	**0**	**45**	**90**	**135**	**180**	**225**	**270**	**315**
		POI							
T_p	[s]	9.11	9.11	11.12	9.11	9.74	9.11	11.12	9.11
$\hat{\theta}_s$	[rad] e^{-2}	4.87	5.36	0.118	5.18	5.13	5.18	.118	5.36
$\hat{\theta}_s \times x_{b,poi}$	[m]	1.07	1.18	0.03	1.14	1.13	1.14	0.03	1.18
$\hat{z}_s$	[m]	0.78	1.41	2.85	1.39	1.02	1.39	2.85	1.41
$\hat{z}_{poi,s}$	[m]	4.09	4.48	2.89	4.46	4.18	4.46	2.89	4.46
$\frac{d}{dt}\hat{z}_{poi,s}$	[m s^{-1}]	2.80	3.21	1.80	3.18	2.67	3.18	1.80	3.21
$\frac{d^2}{dt^2}\hat{z}_{poi,s}$	[m s^{-2}]	2.01	2.41	1.21	2.35	1.77	2.35	1.21	2.41
		Undisturbed							
T_p	[s]	9.11	9.11	9.11	9.11	9.31	9.11	9.11	9.11
$\hat{z}_{rel,s}$	[m]	6.26	5.45	1.02	5.78	5.88	5.78	1.02	5.45
$\frac{d}{dt}\hat{z}_{rel,s}$	[m s^{-1}]	4.62	4.38	1.29	4.50	4.24	4.50	1.29	4.38
$\frac{d^2}{dt^2}\hat{z}_{rel,s}$	[m s^{-2}]	3.74	3.86	1.77	3.83	3.42	3.83	1.77	3.86
		Disturbed							
T_p	[s]	9.11	9.11	11.12	9.11	9.74	9.11	11.12	9.11
$\hat{z}_{rel,s}$	[m]	7.00	6.12	0.91	6.23	5.53	6.23	0.91	6.12
$\frac{d}{dt}\hat{z}_{rel,s}$	[m s^{-1}]	5.24	4.90	0.83	4.81	3.65	4.81	0.83	4.90
$\frac{d^2}{dt^2}\hat{z}_{rel,s}$	[m s^{-2}]	4.41	4.27	0.93	3.97	2.50	3.97	0.93	4.27

TABLE 4.2: Significant values from a spectral analysis for a point at 22 m behind the barge stern

wave headings of 0°, 45°, and 315° creates a partially standing wave pattern behind the stern of the barge(see figures B.1 and B.2) and therefore enhances the increased significant amplitudes. For wave headings of 135°, 180°, and 225° a wake will be formed at the stern of the barge. The results listed in table 4.2 however indicate that only for a wave heading of 180° this wake formation is larger than the contributions of the radiated waves. This is shown by the fact that only for this wave heading the amplitudes of the significant values are smaller for the disturbed approach than for the undisturbed approach.

Because this wave direction is not governing, and the disturbed significant values are used to determine the loads in the quasi-stationary approach whereas in the current engineering method the undisturbed values are used, it can already be predicted that the loads from a disturbed approach will be higher than for the undisturbed approach that is used in the current engineering method. This is in contrast with the hypothesis that the undisturbed approach in the current engineering method is conservative. The sought-after conservatism therefore should not be looked for in a more realistic representation of the surface elevations, although this is an advancement to more realistic modeling in itself and will therefore still be taken into account. It does show the desire for a more detailed description of the loading itself, which is accounted for in the segmented load model.

4.2 Current engineering approach

Because the current engineering approach is not a product of this thesis, only the results of the method for the case study listed above is given here. The results are listed in table 4.3. A more detailed explanation of how these results have been obtained is given in appendix C.

β	[°]	**0**	**45**	**90**	**135**	**180**	**225**	**270**	**315**
Upward force	[N]e6	2.806	2.363	0	2.593	2.331	2.593	0	2.363
Downward force	[N]e6	1.439	1.139	0	1.328	1.182	1.328	0	1.139
Upward moment	[N]e6	50.508	42.525	0	46.666	41.965	46.666	0	42.525
Downward moment	[N]e6	17.836	14.342	0	16.596	14.669	16.596	0	14.342

TABLE 4.3: MPM load results from the current engineering method for undisturbed sea surfaces.

4.3 Quasi-stationary approach

In section 3.3 four quasi-stationary situations have been proposed to determine the hydromechanic loads involved. Now that the motion characteristics of the barge are known, an analysis regarding the actual parameters of interest can be conducted.

It is common industry practice to use most probable maximum values in an extreme value analysis. When assumed that the waves are Rayleigh distributed [Holthuijsen, 2007], the most probable maximum (MPM) values follow from the significant values in table 4.2 by means of equation 4.4. The MPM value is the value that is exceeded once in a storm duration.

$$MPM = \sqrt{\frac{\ln N_w}{2}} \cdot 2\sqrt{m_0} \tag{4.4}$$

In which:

$$N_w = \frac{\text{storm duration}}{T_z} \tag{4.5}$$

and

$$T_z = 2\pi\sqrt{\frac{m_0}{m_2}} \tag{4.6}$$

A spectral estimation of the number of water entry occurrences of the POI considered, during a specific storm duration can be obtained by multiplying the probability that the relative motion amplitude exceeds Δz with the number of waves in one storm. This is written in equation 4.7.

$$N_{slam} = \exp\left(-2 \cdot \left(\frac{\Delta z}{\hat{z}_{rel,s}}\right)^2\right) \cdot N_w \tag{4.7}$$

Heading	[°]	**0**	**45**	**90**	**135**	**180**	**225**	**270**	**315**
					Undisturbed				
T_p	[s]	9.11	9.11	9.11	9.11	9.31	9.11	9.11	9.11
$\hat{z}_{rel}$	[m]	11.92	10.41	2.01	11.05	11.21	11.05	2.01	10.41
$\frac{d}{dt}\hat{z}_{rel,entry}$	[m s^{-1}]	8.63	8.08	2.65	8.36	7.88	8.36	2.65	8.08
$\frac{d^2}{dt^2}\hat{z}_{rel,entry}$	[m s^{-2}]	7.21	7.28	0.00	7.26	6.55	7.26	0.00	7.28
$\frac{d^2}{dt^2}\hat{z}_{poi,entry}$	[m s^{-2}]	3.73	4.41	0.00	4.38	3.20	4.38	0.00	4.41
$\frac{d^2}{dt^2}\hat{z}_{eta,entry}$	[m s^{-2}]	5.05	5.00	0.00	5.02	4.86	5.02	5.00	5.05
					Disturbed				
T_p	[s]	9.11	9.11	11.12	9.11	9.74	9.11	11.12	9.11
$\hat{z}_{rel}$	[m]	13.37	11.68	1.85	11.88	10.50	11.88	1.85	11.68
$\frac{d}{dt}\hat{z}_{rel,entry}$	[m s^{-2}]	9.83	9.13	1.85	8.94	6.68	8.94	1.85	9.13
$\frac{d^2}{dt^2}\hat{z}_{rel,entry}$	[m s^{-2}]	8.48	8.11	0.00	7.46	4.58	7.46	0.00	8.48
$\frac{d^2}{dt^2}\hat{z}_{poi,entry}$	[m s^{-2}]	3.75	4.45	2.28	4.36	3.23	4.36	2.28	4.45
$\frac{d^2}{dt^2}\hat{z}_{eta,entry}$	]m s^{-2}]	6.39	5.49	0.00	4.98	2.31	4.98	0.00	5.49

TABLE 4.4: MPM values for a 3 hour storm from a spectral analysis for a point at 22 m behind the barge stern

With regard to the loadcases of the quasi-stationary approach, but also the current engineering method, the interest lies with the maximum velocity encountered in the number of slamming occurrences instead of the number of waves. When the conservative assumption is made that water entry occurs at the moment that this relative velocity is at a maximum, this value can be found by equation 4.8. The resulting values are given in table 4.4.

$$MPM\left(\dot{z}_{rel,entry}\right) = \sqrt{\frac{\ln N_{slam}}{2}} \cdot \frac{d}{dt}\hat{z}_{rel,s} \tag{4.8}$$

These values will be used as input for the quasi stationary situations from section 3.3. The lengths over which the forces in these situations act are determined by considering the MPM value of $\hat{z}_{rel}$ for points along the cylinder with a spacing of 1 m. It is found that for all headings the MPM value of z_{rel} monotonically increases with overhang length. Therefore the MPM slamming length and drag length can be determined by considering as of which point the MPM value of $\hat{z}_{rel}$ exceeds Δ_z and $\Delta_z + 1.25D$ respectively. The results from this analysis are given in table 4.5.

Heading	[°]	**0**	**45**	**90**	**135**	**180**	**225**	**270**	**315**
Undisturbed									
slam length	[m]	22	22	0	22	22	22	0	22
drag length	[m]	20	11	0	18	19	18	0	11
Disturbed									
slam length	[m]	22	22	0	22	20	22	0	22
drag length	[m]	21	15	0	14	12	14	0	15

TABLE 4.5: MPM lengths measures over which forces act

It stands out that for almost all headings, for both the disturbed and undisturbed approach, the slam length equals the full cylinder length. Apart from the fact that these lengths are MPM extreme values and therefore large values can be expected, it should be kept in mind that viscosity is neglected and therefore the amplitudes of points close to the barge may be overestimated. The influence of viscosity on the validity of the results is further discussed in chapter 6.
The results from the quasi-stationary approach are listed in table 4.6.

β		[°]	**0**	**45**	**90**	**135**	**180**	**225**	**270**	**315**
Upward force	Und	[N]e6	9.211	8.075	0	8.644	5.306	8.644	0	8.075
	Dis	[N]e6	11.951	10.310	0	9.885	2.358	9.885	0	10.310
Downward force	Und	[N]e6	4.592	2.630	0	4.296	3.99	4.296	0	2.630
	Dis	[N]e6	5.628	3.884	0	3.37	2.118	3.37	0	3.884
Upward moment	Und	[Nm]e6	101.325	88.822	0	95.084	58.369	95.084	0	88.822
	Dis	[Nm]e6	131.463	113.406	0	108.735	28.302	108.735	0	113.406
Downward moment	Und	[Nm]e6	55.101	13.393	0	55.85	49.874	55.85	0	13.393
	Dis	[Nm]e6	64.719	56.313	0	50.556	33.881	50.556	0	56.313

TABLE 4.6: MPM load results from a quasi-stationary approach for disturbed and undisturbed sea surfaces.

4.4 Segmented model approach

As explained in the previous section, the results from the quasi-stationary approach are considered inaccurate. The wish for a more representative analysis results in the second approach; a segmented, time dependent model. The model is illustrated in figure 4.3. As already briefly explained in section 3.4, in this model the oversized cylindrical member is divided into sections, for which the acting forces are considered per time step. The resulting forces then follow by summation of all these individual contributions.

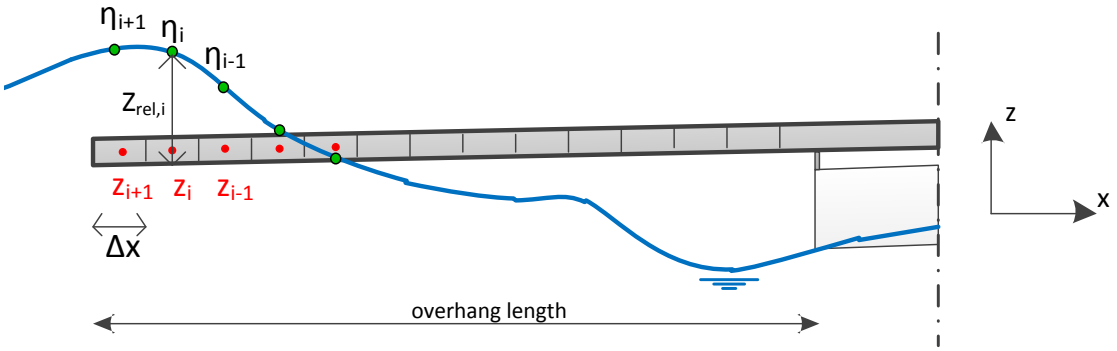

FIGURE 4.3: Visualization of segmented model

To introduce the time dependency of this approach, first the response spectra have to be transformed into time-trace realisations. This is done by means of an inverse fast fourier transform (IFFT) which is shown in equation 4.9.

$$z_{rel,i} = \sum_{j=1}^{N} \hat{a}_i(\beta, \omega_j) \cdot \cos(\omega_j \cdot t + \varepsilon_{a\zeta_0,i}(\beta, \omega_j) + \varepsilon_{\zeta_0\zeta,j}) \tag{4.9}$$

In which:

N	=	number of wave components
ω_j	=	angular frequency of wave component j
$\hat{a}_i(\beta, \omega_j)$	=	frequency dependent amplitude of relative motion of segment i
$\varepsilon_{a\zeta_0,i}(\beta, \omega_j)$	=	frequency dependent phase shift of relative motion of segment i with regard to wave origin
$\varepsilon_{\zeta_0\zeta,j}$	=	random phase shift of wave component j with regard to wave origin

This is also visualized in figure 4.4a.

For this study time-traces with a duration of 3 hours and a time step of 0.1 s are generated. The wave frequencies are chosen equally spaced in the range between $0\,\mathrm{rad\,s^{-1}}$ and $2\pi\,\mathrm{rad\,s^{-1}}$, since this is the range in which the response spectrum is defined. The amplitudes of the wave components can then be found from the response spectra by equation 4.10.

$$\hat{a}_i(\omega_j) = \sqrt{2 \cdot S_{z_{rel},i} \cdot \Delta\omega} \tag{4.10}$$

The frequency dependent phase shift $\varepsilon_{a\zeta_0,i}(\omega_j)$ is the corresponding phase shift of the relative vertical motion with regard to the wave excitation in the wave origin. These follow from the analysis given in appendix 3.1.3. The additional phase shift $\varepsilon_{\zeta_0\zeta,j}$ is due to the phase shift of the incident wave itself with regard to the wave origin. Since the phase information of the sea state is lost when the variance spectrum is created, this additional phase shift is taken randomly between $0\,\mathrm{rad\,s^{-1}}$ and $2\pi\,\mathrm{rad\,s^{-1}}$ for every wave component. This is consistent with linear wave theory, since one of the main assumptions is that the waves are randomly distributed [Holthuijsen, 2007]. The additional phase shift is constant for every segment considered per wave component. A realisation of $\hat{a}_{22}(\omega_j)$ and $\varepsilon_{a\zeta_0,22}(\omega_j)$ for the case study of a segment at 22 m overhang length is illustrated in figure 4.4b.

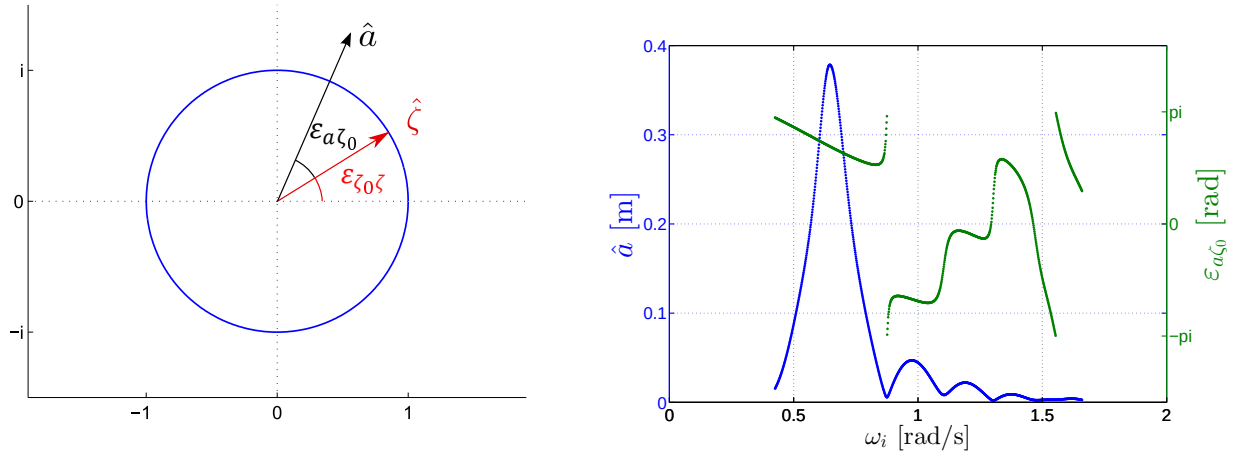

(A) Amplitudes and phases in the complex plane

(B) Amplitudes and phase shifts used in IFFT for a segment at 22 m overhang length for $\beta = 180°$

FIGURE 4.4: Example of amplitudes and phase shift used in IFFT

The analysis results in a time-trace realisation of the relative vertical motion. For the segmented model this realisation is made for every segment. An example of a time-trace for a segment at 22 m overhang and 180° wave heading is given in figure 4.5a. Figure 4.5b shows a zoomed view of the timetrace in figure 4.5a. It can be seen that for this realisation in the time range of 200 s to 300 s the initial gap Δz is exceeded, and thus water entry of this segment occurs three times in this time range. During the submerged state of the segment, hydrodynamic forces are generated. Depending on the position of the segment with regard to the water surface, different force mechanisms are governing as is described in section 3.4.

Figure 4.6 shows an analysis of the submergence event of the grey shaded area in figure 4.5b. In this plot the coloured shadings correspond to the different loading states that are shown in figure D.2. In the top plot the dimensionless submergence of the segment at 22 m overhang with a length $\Delta x = 1$ m is shown. In the two middle plots the corresponding velocities and accelerations are shown. The bottom plot gives the forces on the segment. It can be seen that in the water entry state the time-step is refined to $\Delta t_i = 0.01$ s to make sure that also the first phases of water entry are covered and that there is enough resolution to determine C_s accurately enough. The first submerged time step occurs at t =5702 s, where $z_{rel} = 5.72$ m and the dimensionless submergence thus equals 0.14. At this submergence the slamming coefficient has already reduced from $C_s = 5.15$ to $C_s = 2.58$, which shows the importance of the time step resolution in the water entry state. The figure also

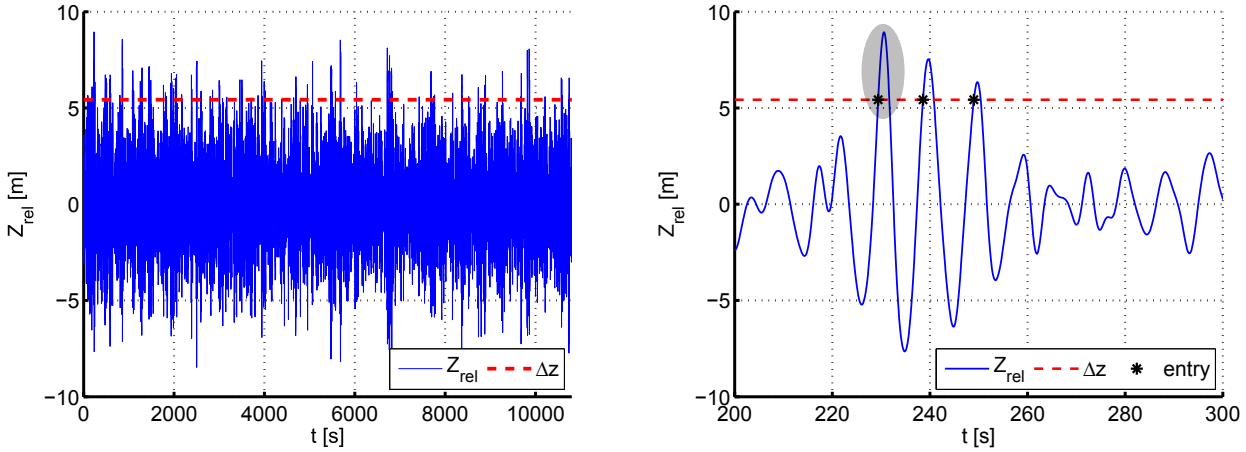

(A) 3 hour timetrace realisation for a segment at 22 m overhang and $\beta = 180^{\circ}$

(B) Zoom of time-trace in figure 4.5a for occerences of water entry

FIGURE 4.5: Example of a time trace realisation

shows the procedure that is implemented in the developed segmented force model, in which the time step is reduced with a factor ten in the water entry state, and the submergence and relative velocity parameters are determined by backward linear interpolation upto the first time step before water entry. In the bottom plot the influence of this interpolation on the total force can be seen. Due to the interpolation, the highest upward force on the segment is assigned to time step $t = 5701.9\,\text{s}$ due to the refined time step, whereas without this refinement the maximum upward force would only be about half the value.

In table 4.7 the difference in total upward between applying and not applying the refined time step is shown. These high forces exist only for very short time durations but are also treated as static forces. The influence of this short time duration is further discussed in chapter 6.

$F_{v,total}$	upward	without refinement	with refinement	rel. error.
MPM	[N] e6	0.773	1.1702	-34%
P95	[N] e6	1.1706	1.925	-39%

TABLE 4.7: Difference between simulations with and without refined water entry time step. MPM and P95 total upward force results from 100 simulations for β =180°, $\Delta t = 0.1\,\text{s}$, and $\Delta t_{int} = 0.01\,\text{s}$ with disturbed sea surface approach.

It can be seen in figure 4.6 that in the water entry state and in the first part of the drag downward state the relative velocity is close to its maximum value. This combined with the fact that the slamming coefficient is large for small submergences leads to the fact that the upward vertical force is very high in the initial stage of water entry. As the cylinder further submerges the relative velocity declines, and accelerations increase. In the first part of the drag downward state the velocity is still large, such that drag forces dominate and the loading is directed opposite to the direction of relative movement. In the second part of the drag downward state however accelerations increase. The combined contributions of the loading due to the Froude-Krylov force, entrapped water, and added mass are all directed in the same direction. Therefore in the second stage of the drag downward state, the direction of

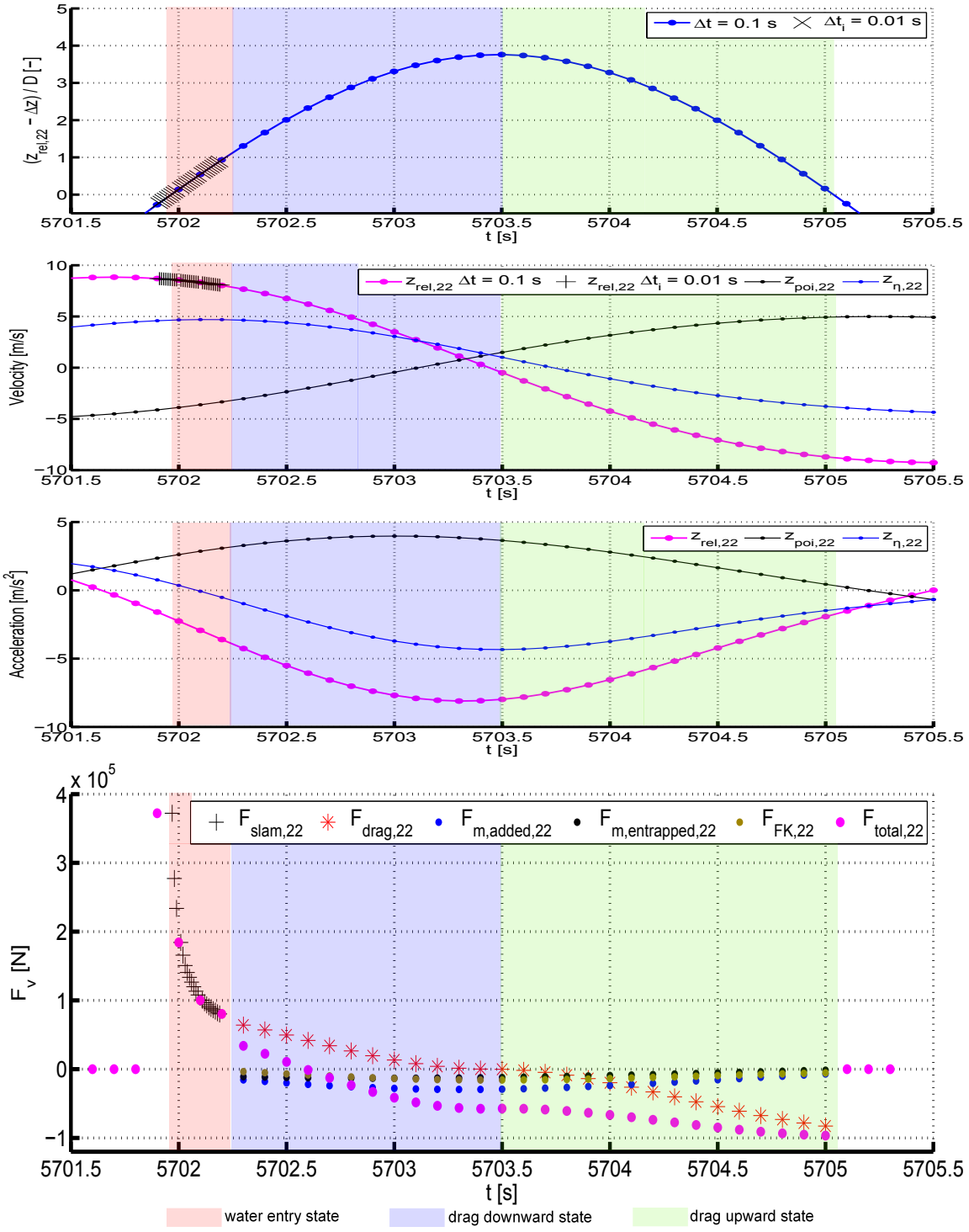

FIGURE 4.6: Example of a time trace realization for one segment at 22 m overhang length and wave heading 180°

loading is reversed and inertia loads dominate. As the drag upward state is reached, the direction of relative motion is reversed and the accelerations on the cylinder diminish. The decrease in downward acceleration loads however is compensated by an increase in downward loading due to increasing drag force. As the acceleration decreases, the relative velocity increases. Because the drag force scales with the squared velocity, the total downward force increases until the cylinder emerges again.

In table 4.8 the influence of different time step sizes on the resulting forces is investigated.

Δt [s]	MPM Upward [N]e6	P95 Upward [N]e6	MPM downward [N]e6	P95 downward [N]e6
0.025	1.0941	1.5648	0.5713	0.6508
0.05	1.1060	1.6185	0.5636	0.6462
0.1	1.1848	1.8406	0.5759	0.6739
0.5	0.6787	1.5519	0.5559	0.6512
1	0.2209	0.5313	0.5097	0.5937
2	0.0043	0.0410	0.3466	0.4245

TABLE 4.8: Influence of time step size on force results. Obtained from 100 simulations for β =180° with disturbed sea surface approach.

From the determination of forces as shown in figure 4.6, the total force on a segment as a function of time can be found. By conducting this analysis for every segment and summing up the total forces, the total resulting forces the support can be found. By applying equation 3.40 also the bending moment can be determined.

4.4.1 Results

As is mentioned in the previous section, the summation of the forces acting on the segments gives a total vertical load, and a resulting bending moment per time step. The maximum values per simulation of the total upward and downward force and both the positive and negative bending moments are collected from a 3-hourly simulation. The simulation is repeated a number of times, which means that for each simulation the phase shifts $\varepsilon_{\zeta_0\zeta,j}$ are generated randomly. In this study 100 unique time trace realizations are generated per wave heading. The maxima values from every simulation can then be used in an extreme value analysis. The simulations result in 100 maxima for the vertical forces and bending moments. When these results are sorted, their probability of exceedance can be determined by equation 4.11. As an example, the extreme values and corresponding probabilities of exceedance of the total upward vertical force are shown in figure 4.7. In this figure also maximum likelihood estimator fits of a Weibull and Gumbel extreme value distribution are shown. For further comparison of the results, the P95 values from equation 4.11 and MPM values from a Weibull fit are used. The results for the forces and bending moments for eight wave headings and both an undisturbed and disturbed approach of the sea surface elevation are given in table 4.9.

$$P = 1 - \frac{position}{\#simulations} \tag{4.11}$$

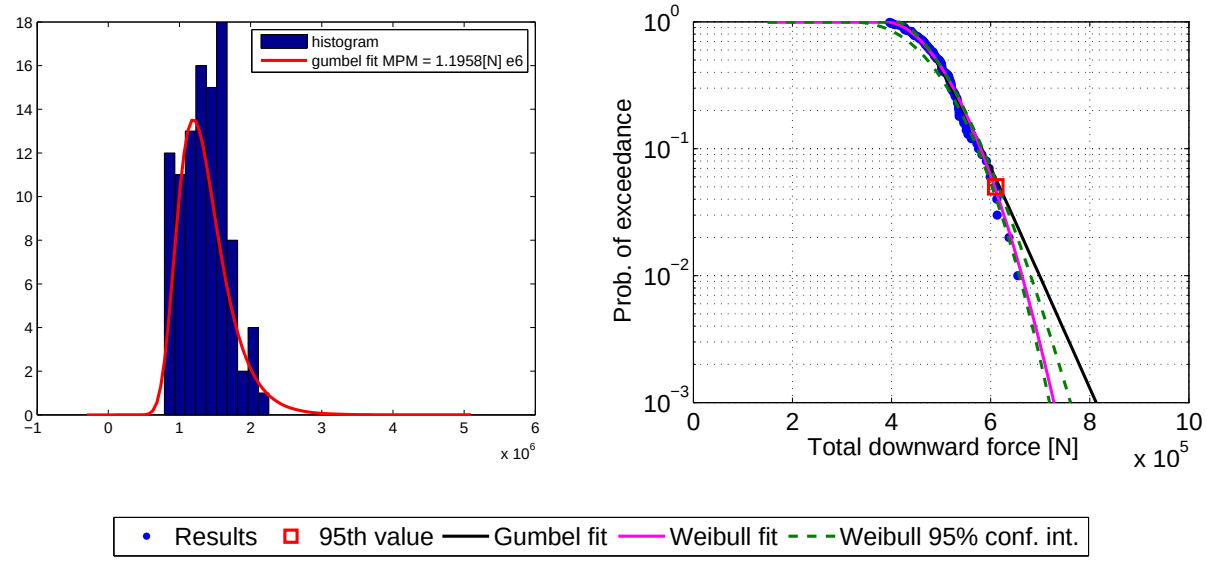

FIGURE 4.7: Extreme value analysis for total vertical forces results from segmented model approach with disturbed sea surface for $\beta = 180°$

β		[°]	**0**	**45**	**90**	**135**	**180**	**225**	**270**	**315**
MPM										
Upward force	Und	[N]e6	0.869	0.713	0	1.966	1.349	1.981	0	0.684
	Dis	[N]e6	2.490	1.663	0	1.785	1.196	1.989	0	1.780
Downward force	Und	[N]e6	1.474	1.346	0	1.192	0.961	1.170	0	1.291
	Dis	[N]e6	1.908	1.531	0	0.906	0.565	1.119	0	1.572
Upward moment	Und	[N]e6	15.701	12.934	0	29.639	21.394	29.917	0	12.552
	Dis	[N]e6	37.545	27.289	0	29.534	19.419	30.357	0	28.604
Downward moment	Und	[N]e6	18.889	17.635	0	15.239	12.579	15.142	0	16.750
	Dis	[N]e6	24.594	20.923	0	13.713	8.179	14.334	0	21.360
P95										
Upward force	Und	[N]e6	1.420	1.207	0	3.085	1.983	3.094	0	1.140
	Dis	[N]e6	3.968	2.814	0	2.388	1.948	2.548	0	3.645
Downward force	Und	[N]e6	1.696	1.649	0	1.377	1.094	1.352	0	1.496
	Dis	[N]e6	2.317	1.759	0	1.046	0.663	1.051	0	1.854
Upward moment	Und	[N]e6	23.277	21.753	0	43.197	30.630	46.321	0	21.578
	Dis	[N]e6	57.082	42.318	0	39.992	31.060	42.727	0	51.659
Downward moment	Und	[N]e6	23.346	21.030	0	17.668	14.579	17.992	0	19.642
	Dis	[N]e6	29.683	24.334	0	16.748	9.566	16.964	0	25.014

TABLE 4.9: MPM and P95 load results out of 100 simulations from a segmented model approach for disturbed and undisturbed sea surfaces. $\Delta x = 1\,\text{m}, \Delta t = 0.1\,\text{s}$, *Dis* = disturbed sea surface approach, *Und* = undisturbed sea surface approach.

4.5 Comparison of results

With the results from three approaches known, conclusions can be drawn with respect to their relative differences. The comparison here will be based on MPM values.

First it is noted that the quasi-stationary approach results in the highest loads in general. When this approach is compared with the segmented model approach, the differences are largest for upward directed forces. This can be explained by the fact the in the quasi-stationary approach the high limit value of $C_s = 5.15$ is used over the entire slamming length, and that the entry velocity (which is squared in the load equation) is taken at the most unfavorable point. For the downward directed forces the differences are less but still significant, in the order of a factor 2 to 4. Because the quasi-stationary model and the segmented model take into account the same loading mechanisms, this difference may be ascribed to the fact that in the quasi-stationary model the values of one governing POI are used, and that in the quasi-stationary approach the inertia related loads are combined such that they all are at a maximum simultaneously.

When the results from the current engineering method are compared with the segmented model results, it is found that for an undisturbed sea surface approach of the segmented model, the results of the current engineering method are larger for all headings for upward directed loads. The difference is quite significant, especially for stern waves. Because the upward forces in the current approach are governed by the first load case (water entry), this is probably caused by the fact that a constant slamming coefficient is used. For downward directed loads the differences are less convincing. The current engineering method gives smaller loads for wave headings 45° and 315°. It should however be noted that in the current engineering approach no contributions due to the Froude-Krylov force and added mass are taken into account.

When the results from the segmented model with a disturbed approach are compared to the current engineering method (which is based on an undisturbed approach), it is concluded that for the upward working load the results of the current engineering method are still larger. This is remarkable since in chapter 3 and in section 4.1 it became clear that the significant values of the relative motion with a disturbed approach are larger than the values of the undisturbed approach, especially for stern waves. From this the added value of a detailed model to describe the loading becomes evident.
For the downward directed load the results from the segmented model with a disturbed approach are only larger for stern waves (0°, 45°, and 315°) and the differences are relatively small, but still significant.

Furthermore it is interesting to conclude that for the segmented model results with a disturbed approach for the free surface elevation, both upward and downward working loads are smallest for a wave heading of 180°.

Chapter 5

Validation of segmented force model

In this chapter the segmented force model that has been created as part of this thesis is validated. This is done by means of a number of typical orientations for which results can be compared to theory. For all these situation a cylinder of length 22 m and diameter 2.13 m is used. For the incident wave a monochromatic deep water wave of height 6 m and angular frequency $0.6\,\mathrm{rad\,s^{-1}}$ is chosen. Because the wave length is much greater than the cylinder diameter $\left(\frac{D}{\lambda} \ll 0.2\right)$, diffraction effects may be neglected and theory on slender structures such as the Morison equation may be applied.

5.1 Stationary, fully emerged, horizontal orientation

In this orientation the cylinder is kept horizontal (θ =0 rad) and stationary at a level of $z_{poi} = 6$ m, where $z = 0$ equals MSL. This orientation is sketched in figure 5.1. Since the amplitude of the incident wave is lower than Δz, and gravity is not included in the calcuation of the hydrodynamic loads, the force result should equal zero. This can also be found in the simulation results for this situation, that are shown in figure 5.2.

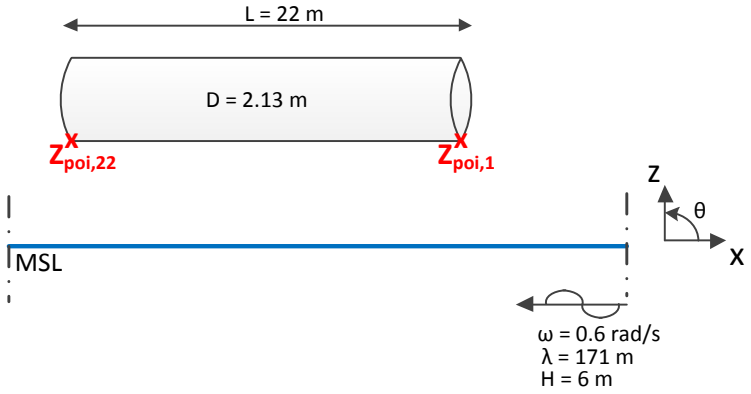

FIGURE 5.1: Validation sketch orientation 1

It can also be clearly seen that an undisturbed approach is chosen by the fact that the wave height at the two poi's is equal to the wave height of the incident wave. The phase shift between the the plotted lines is caused by the spatial distance between the two points.

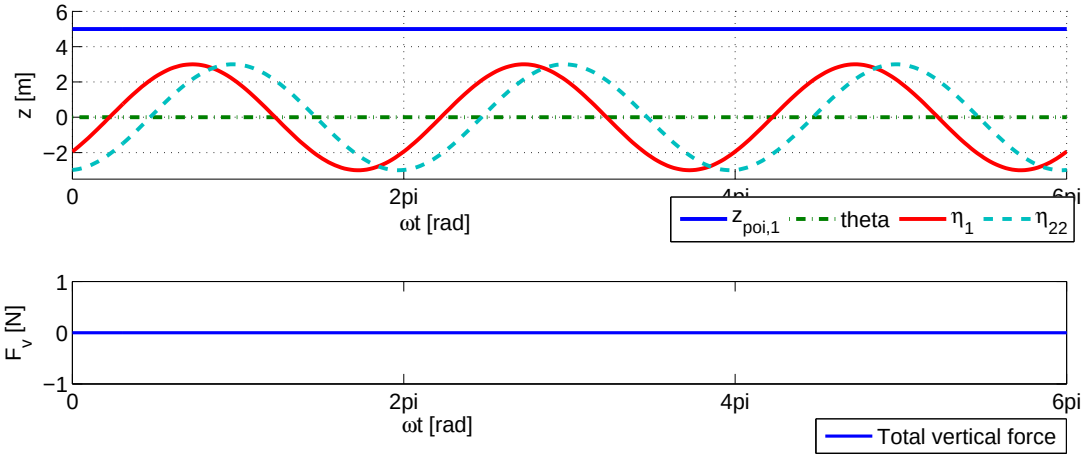

FIGURE 5.2: Simulation results for validation orientation 1

5.2 Stationary, fully submerged, horizontal orientation

In the second orientation the cylinder is kept horizontal (θ =0 rad) and stationary at a level of $z_{poi} = -6$ m. This orientation is sketched in figure 5.3. The characteristics of this orientation can be found in the top plot of figure 5.4.

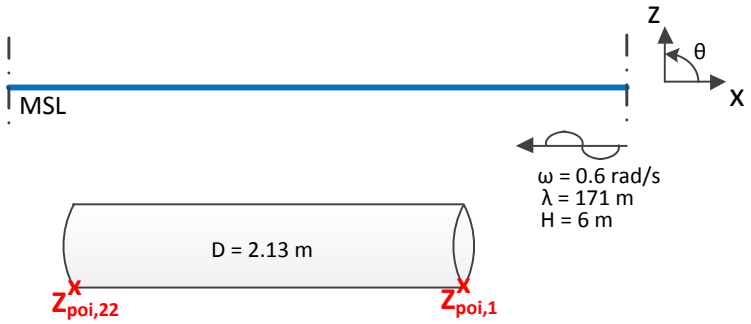

FIGURE 5.3: Validation sketch orientation 2

Because the cylinder is kept stationary and can be regarded as a slender body, the total load can be described with the Morison equation, see chapter 2.

$$F_v = \frac{1}{2}\rho_w C_D D u_v |u_v| + \rho_w A C_M \dot{u}_v \tag{5.1}$$

in which $C_D = 1$ and $C_M = 2$.

Because the cylinder is placed perfectly horizontal, only the vertical fluid flow will cause a loading. The 90° phase shift between the orbital velocity and acceleration can be found back in the time trace of the forces, which is shown in the bottom plot of figure 5.4. It can be seen that the peaks of the total force are in phase with the peak of the inertia forces. From this it can be deducted that the Froude-Krylov forcing and added mass load are exactly in phase whereas the drag force is out of phase, which indeed is a confirmation that the absolute motion of the cylinder is zero. From equation 5.1 it can be obtained that the amplitude of the inertia forces for a cylinder length of22 m should equal 1.45×10^5 N, whereas the segmented model results in 1.568×10^5 N. This difference is caused by the fact that in the segmented model the decrease of the orbital fluid motion with depth is not taken into account.
From the same equation it can also be deducted that the maximum drag force should equal 0.5×10^5 N. The maximum drag force from the segmented model equals 0.522×10^5 N. Also this difference is caused by the fact that in the segmented model the decrease of the orbital fluid motion with depth is not taken into account. The small conservatism of this approach is herewith proven.

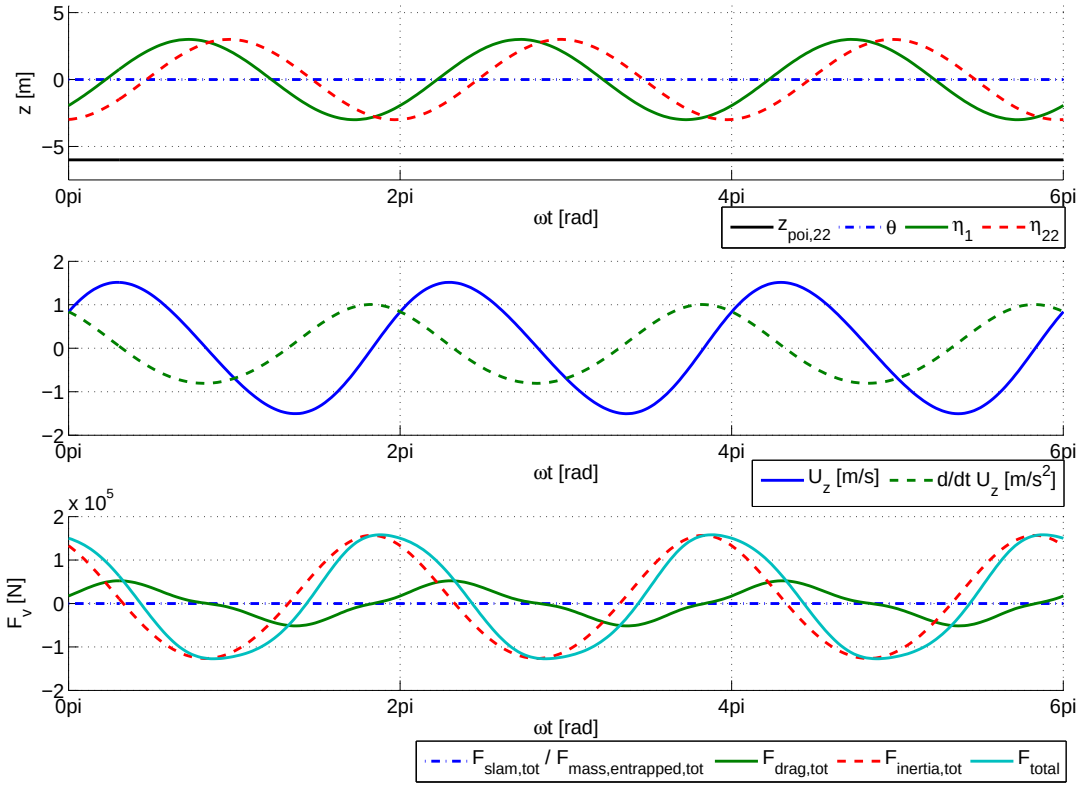

FIGURE 5.4: Simulation results for validation orientation 2

5.3 Constant velocity, still water, horizontal orientation

In this orientation the cylinder is kept horizontal (θ =0 rad) and is forced downward with a constant velocity of $-3\,\mathrm{m\,s^{-1}}$ with regard to a stationary still water line. This orientation is sketched in figure 5.3. The velocity is chosen such that $Fr > 0.6$, which according to Miller [1977] is a condition for slamming loads to predominate. To make sure that enough resolution is available to determine C_s accurately, the refined time step method as explained in section4.4 is applied.

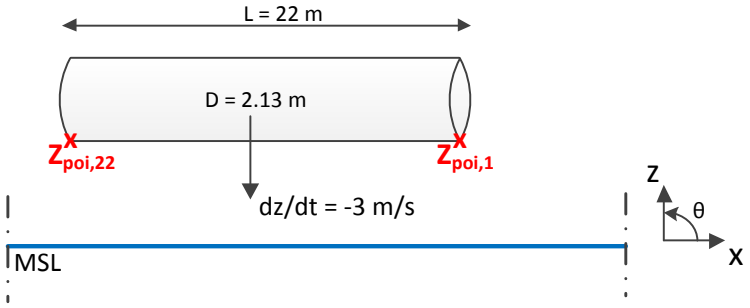

FIGURE 5.5: Validation sketch orientation 3

Because only the cylinder moves with a constant velocity, only water entry loads will be generated up to a submergence of 1.25 D, whereafter drag forces will be generated. Since there are no accelerations of the body or water particles, all inertia forces equal zero. As can be seen figure 5.6 the model behaves as expected.

The maximum values for the slamming and drag load can also be determined. Because the cylinder is kept horizontal, the entire cylinder length will enter the water simultaneously, resulting in a maximum total upward force at moment of impact. With $C_s = 5.15$ for $z_{rel} = 0$, $dz/dt = 3$ m/s, $\rho_w = 1025$ kg/m^3, and D=2.13 m this value should equal 1.113 MN. The slam force should converge to a constant drag force of 0.216 MN at a moment that $z_{rel} \geq 1.25$ D. Figure 5.6 shows good agreement with these expectations.
It should be realised that while the maximum impact force corresponds with theory, the forces at greater dimensionless submergences are overestimated, because for the determination of the slamming coefficient, a envelope of peak values is used to get rid of the dependency of impact angle.

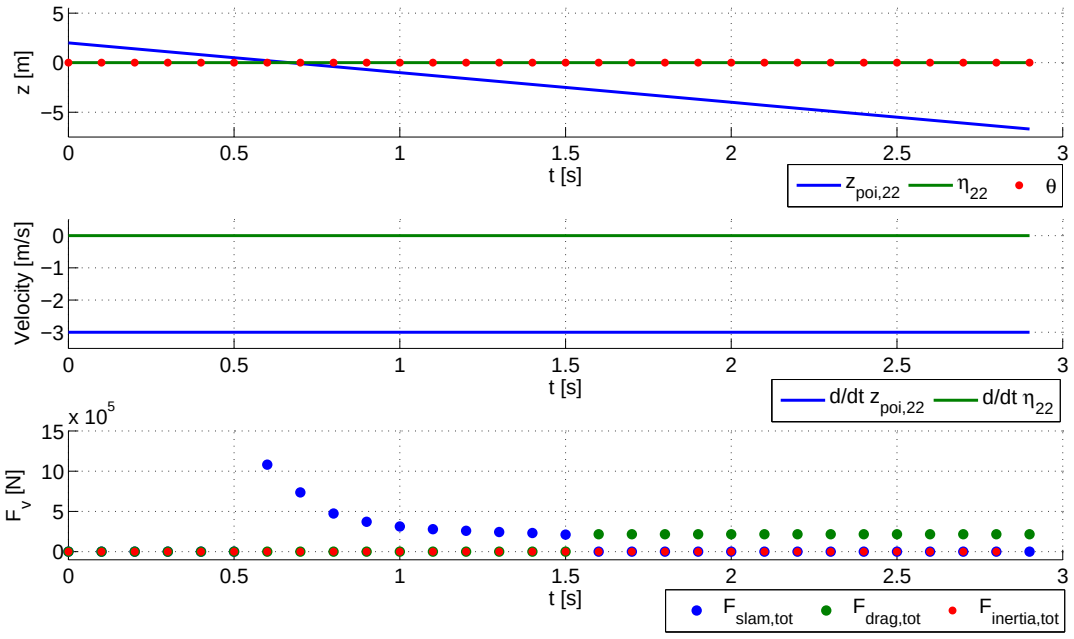

FIGURE 5.6: Simulation results for validation orientation 3

Chapter 6

Discussion

For simplicity and due to time constraints various assumptions have been made. The influence of these assumptions on the result is discussed here.

6.1 Motion influencing assumptions

Viscous effects
The analysis of the barge motions that is given in appendix B makes use of potential theory. Potential theory is based on the assumption of an ideal fluid and assumes that the fluid is incompressible, inviscid, and irrotational. The damping that is used in the equations of motion therefore only includes potential damping. In reality however viscosity will exist and therefore will be of influence on the barge motions as an additional form of damping due to friction and vortices. For the sway, heave, yaw, and pitch motion the major part of the damping is caused by radiation damping [Journee and Massie, 2001]. Because in this thesis only heave and pitch motions are regarded, viscosity is of minor importance and is therefore neglected. With neglecting the effect of viscosity the modeled motions of the barge are slightly overestimated, so this is a conservative approach. When however eccentric cargo is regarded, and roll motions should be considered, viscous damping can become of importance. A commonly applied method to account for this effects it to apply additional roll damping in the equation of motion, as a percentage of the critical damping.

Additionally, neglecting viscosity will lead to an overestimation of sea surface amplitudes and velocities for field points close to the barge. This eventually introduces extra conservatism in the disturbed approach.

Influence of slamming forces on barge motions
One of the main assumptions of this study is that the forces on the pile overhang do not influence the motions of the barge. In equation 3.40 and figure 3.15 it is shown how for the segmented model approach the bending moment caused by the hydrodynamic loads on the oversized cylinder can be computed at the place of the supports. The same equation can be used to calculate the total moment around the center of floatation of the barge, which then can be used as a force term in the equation

of motion of the pitch motion of the barge. It is found that for the case study in chapter 4, the exciting moment around the COF of the barge due to the impact forces is about 10% of the exciting moment induced by the Froude-Krylov force and the diffraction force caused by the waves on the barge. Therefore the assumption that the forces on the cylinder due to its interaction with the fluid can be neglected on the motion is justified. When multiple cylinders are placed next to each other, or structures with larger dimensions are applied, this assumption may become less valid. When the loading may not be neglected in the determination of the barge motions, the results of the hydrodynamic forces on the structure from the segmented model can be in the equation of motion to account for this interaction in the time domain. The equation of motion can be expanded with an impulse response function equation 6.1 [Cummins, 1962]. It should however be noted that (numerically) solving this equation may be be computationally expensive. For more information reference is made to Journee and Massie [2001].

$$(M + A)\,\ddot{x} + \int_0^\infty B\,(\tau)\,\dot{x}\,(t - \tau)\,d\tau + Cx = F(t) \tag{6.1}$$

6.2 Load influencing assumptions

Forward tow speed

In the current analysis the forward tow speed of the barge is neglected. The contribution of this forward speed to the relative speed of water entry, or submerged drag velocity is therefore not accounted for. The influence on the vertical force however is very small, because pitch angles stay small for conditions in which a significant forward speed is still possible. The contribution to the vertical force in that case is small as well.

Neglecting the forward speed also means that the motions of the barge itself are overestimated. Namely when the barge pitches, the towing force F_{tow} becomes increasingly eccentric, which will cause a restoring moment M_r as illustrated in figure 6.1.

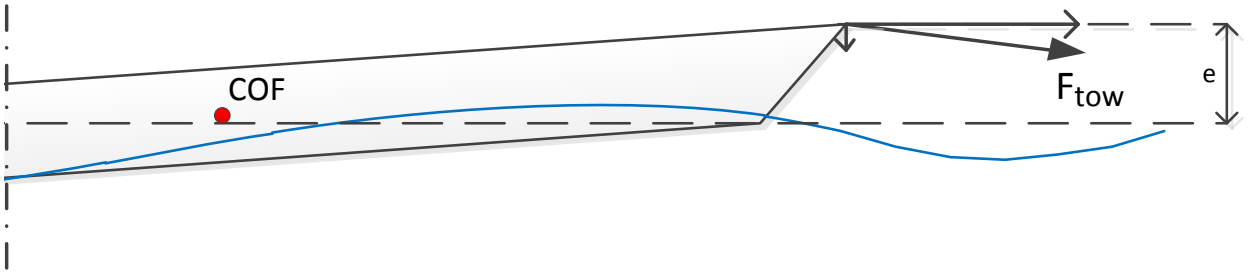

FIGURE 6.1: Restoring moment

Screen effect

In this thesis the hydrodynamic loads on a single pile have been investigated. In reality however often multiple piles are transported at once. Depending on the arrangment of the piles, additional effects may play a role. Apart from the fact that when piles are placed eccentric from the barge x-axis roll motions have to be considered, the presence of multiple piles will also possibly influence to loading. Two of the most commonly encountered configurations have been sketched in figure 6.2.

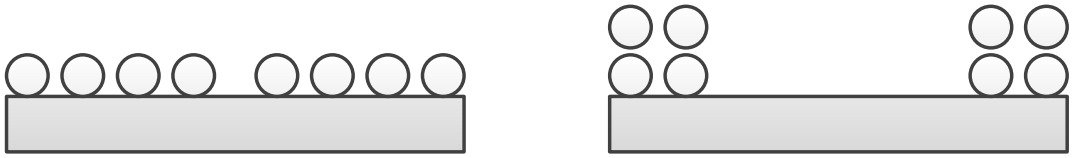

FIGURE 6.2: Different encountered lay outs for pile transport

The limited distance betwteen the piles will introduce a screen-effect when the flow in between the piles gets hindered. With decreasing spacing between the piles, the orientation will behave more like a flat plate under hydrodynamic loading. A detailed analysis of this effect fall outside the scope of this thesis, but reference is made to Jacobsen and Hansen [1990].
In the second orientation in figure 6.2 the first row of piles will create a wake when moving through the water. This will significantly reduce the hydrodynamic loading on the second row. It therefore is preferable to place the piles in such an orientation. With respect to the right orientation in figure 6.2 it is more preferable to put the piles placed closer to the barge x-axis when possible.

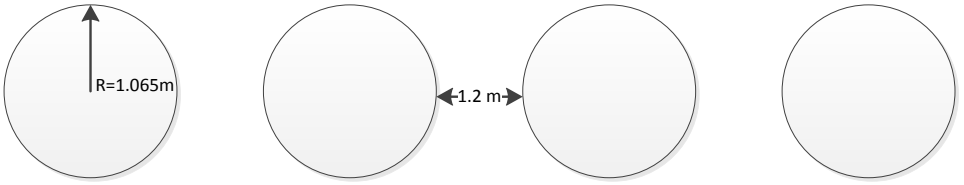

FIGURE 6.3: Multiple piles on a row with limited spacing leads to screen effects

Load dynamics

For the transfer of the loads on the cylinder to the supporting structure, the forcing is treated as if it were a static load. Especially for the slamming loads at the first stage of water impact, this seems to be inaccurate. The peak loads at the first stages of water impact have a duration in the order of 10^{-2} s. A dynamic analysis of the structural transfer of these to their supports therefore would is advisable.

Orbital water particle motions

The effect of a decrease of the amplitude of the orbital motions of fluid particles is neglected in this thesis. Since the fluid acceleration occurs in the Froude-Krylov force and the added mass force, and the fluid velocity in the drag force these forces will be slightly overestimated. The effect is briefly touched upon in chapter 5. For a more detailed, less conservative approach, this decreasing amplitude can be taken into account. For the magnitude of this effect in irregular waves, reference is made to Daemrich [1982].

Chapter 7

Conclusions and recommendations

With increasing dimensions of offshore structures it has for various reasons become wishful to more often transport structural modules of which the dimensions are larger than the equipment it is transported with. Due to the relative motions with the sea surface, hydrodynamic loads are generated that up to now have been assessed in a limited way.

To formulate conclusions with regard to this topic, the main research question that was formulated in the beginning of this report is restated here:

"What are the hydromechanic loads on oversized cylindrical cargo during towed marine transport and how can these loads be quantified?"

In this thesis an attempt is made to gain a better understanding of the hydrodynamics related to this problem. It is found that by using potential theory, the relative motions of the structure with regard to the sea can be determined in a detailed way. With taking the effects of wave diffraction and radiation on the free surface level into account, it is discovered that the relative motions have a peak in the wave frequency range that is often encountered in marine transports. Moreover it is found that the heading of the waves encountered is of great influence on the magnitude of the forces that are generated. For cargo that is transported on a barge with a stern overhang, head seas are preferable because of the wake that is formed at the stern of the barge due to wave diffraction. For commonly encountered wave frequencies however this effect is largely opposed by wave radiation due to the barge motions. For stern waves a scattered wave field is generated at the stern of the barge. This leads to larger relative responses and thus forces than is accounted for in an approach where diffraction is not taken into account. This effect is increased by wave radiation of the barge.
Taking all these effects into account, two approaches to determine the total resulting loads have been developed. The results for a quasi-stationary approach and a more detailed segmented model approach show very large differences. The smaller results from the detailed approach prove the conservatism of the first approach and partly of the current engineering approach.

It is concluded that a more realistic description of relative motions than is commonly done in industry does not necessarily have a significant beneficial effect on the motion characteristics. In some cases, mainly for stern waves, the effects of wave diffraction even have a disadvantageous effect on the relative motions and therefore the loading.
It is however shown that by using a detailed model of the hydrodynamic loading, the estimation of the forces involved is reduced significantly. This gives possibilities for a more efficient use of construction material. Additionally critical offshore time can be saved whilst a more realistic approach with regard to relative motions is followed. The model that is created as part of this thesis is not significantly more expensive in terms of computation time than techniques used in current engineering approaches and is validated by means of existing theory. The results from the model are just slightly conservative and show good overall agreement when compared with this theory.

7.1 Conclusions

- **A clear peak in the response functions of the vertical relative motion is found at wave periods that are commonly encountered during marine transport. For** 122 m **long cargo barges this is mainly between** 7 s **and** 12 s**. This holds true for all wave headings for both a disturbed and undisturbed approach with regard to the sea surface elevation.** The relative motions have been determined for centrically positioned cargo that is oversized at the stern of the barge. Because of the almost symmetrical form of the barge this conclusion will also hold true for bow overhangs. When cargo is oversized at starboard or port side, as sometimes occurs during the transport of oversized jackets, beam seas might become governing however since roll motions will be of influence.
  It is found that when the effects of wave diffraction and radiation are taken into account, the peak amplitude of the relative motions for bow waves stays almost unchanged compared with an undisturbed approach. The effects of wake formation due to wave diffraction are largely opposed by the radiated waves due to the barge motions.
  For stern waves the effect of wave diffraction leads to a scattered wave field at locations of cargo overhang. This gives rise to enlarged amplitudes of relative motion. This enlargement is further increased by radiated waves.

- **The physical mechanisms that play a role during the interaction of the structure with the fluid have been determined from literature and are well known.** This holds true for all relevant effects except water exit. This has been dealt with in a upper bound approach. Because a wide range of environmental conditions are probable to occur and the main interest lies with extreme loading situations, upper limit values of coefficients for slamming, drag, and inertia forces are applied. The fact that slamming coefficients are dependent on dimensionless submergence is one of the main findings that is applied in a newly developed method for loading calculation.

- **The results between the two approaches that have been developed to determine the loads differ significantly. Based on a case study, the loads resulting from a segmented model approach are two to ten times as small as the loads from a quasi-stationary approach.** Both approaches have been applied to a suitable case study. The quasi-stationary approach results in higher loads in all respects with regard to the current engineering method. A starting hypothesis was that the current engineering method is very conservative. This hypothesis is violated with the results from the quasi stationary approach. To gain more insight in the different load contributions, the time dependent segmented load model was created. The difference in load results from this model compared with the quasi-stationary approach, ranges from a decrease with a factor two to a decrease with a factor ten. This is presumably caused by the facts that the quasi-stationary approach uses the maximum relative velocity at the most unfavorable position to determine water entry loads for the entire submerged part of the cylinder. Additionally, a constant maximum value for the slamming coefficient is used. Also the most unfavorable value for accelerations is used to determine inertia loads along the submerged part of the cylinder. Whereas the segmented model takes into account the phase difference of the relative motions for different points along the cylinder.

- **Validation of the segmented model shows good agreement with literature, and only slight conservatism of the model.** To increase the confidence in the results from the segmented model, the model has been validated by means of a number of typical orientations. When compared with theory the model shows slight conservatism due to a number of assumptions. Overall, good agreement with theory is found.

- **Compared with the current engineering model, the segmented model approach gives lower force values for all wave headings for upward forces. For downward forces this also holds true except for headings of** 0°, 45°, **and** 315°**.** For an undisturbed approach of the segmented model (that is also used in the current engineering method), the upward directed loads from the segmented model are lower for all wave headings. For downward directed loads, the loads from the segmented model with an undisturbed approach are lower for all wave headings, except 0°, 45° and 315°. In the current engineering approach however, loads due to Froude-Krylov forces and added mass are not taken into account, and therefore the comparison gives a skewed view.
  For a disturbed approach of the segmented model, the results compared to the undisturbed current engineering method for upward directed loads are lower for the segmented model for all wave headings. For the case study, the difference is largest at a 180°, namely about a factor two. For 0° wave heading the difference is least at about 20 %. For the downward directed

loads, again only for wave headings of 0°, 45° and 315° the results from the current engineering approach are lower, with about a factor 0.3 for a 0° heading. For a 180° heading the results for downward forces from the segmented model are about half as large as from the current engineering approach.
It is interesting to notice that the segmented model results in lower load results in general, even for disturbed approaches that result in higher significant values of relative motions for stern waves. This is one of the main indicators that application of a segmented model can be of added value when a reduction of conservatism is required.

From the segmented model results it may be concluded that a wave heading of 180° is preferable when a storm is encountered. This may be an additional reason for tug boats to weathervane in stormy conditions.

7.2 Recommendations

This thesis has given rise to a number of new questions that are worth exploring in more detail.

Validation
Unfortunately it has not been feasible to validate the developed segmented model by means of experimental data. It is wishful to do so because a number of assumptions have been made in the approach. These include:

- A potential flow for the surrounding wave field around the barge
- A conservative choice for constant force coefficients for drag and inertia loads and for water exit effects
- A conservative approach for the force coefficient of slamming loads, in which the dependency on dimensionless submergence is taken into account. The dependency on the angle of impact however is overcome by determining a converging envelope of peak values.
- Entrapped water is assumed to be accelerated with the absolute acceleration of the cylinder by which possible interaction with the outside fluid domain is neglected. This could be mainly of influence on segments close to the outer cylinder boundary.
- The decreasing orbital motions with increasing water depth are neglected

These items give cause for validation of the segmented force model by means of experimental data. For this full scale or model scale experiments can be conducted. In the case of model scale experiments however attention has to be paid to scaling effects since a number of loading mechanisms are included that scale with different dimensionless numbers. These are Froude numbers for slamming loads, and Reynolds and Keulegan-Carpenter numbers for drag and inertia loads.

Feedback of forces on barge motions
For the case investigated in this study, the influence of the cylinder loads on the barge motions are negligible, as is stated in chapter 6. For different cargo arrangments or dimensions however this assumption may be violated and therefore it is interesting to investigate the influence of the forces on the barge motions. This holds especially for the short, but high impact forces at the initial stage of water entry.

Different barge characteristics
In this thesis a standardized, 122 m long cargo barge has been investigated. Changing the barge draft, mass (including cargo) and submerged geometry will change the hydrodynamic coefficients of the barge that are used in modeling the motions. Additionally also the extent of the wave diffraction is governed by the submerged geometry.

Dynamic consideration of load transfer
As is mentioned in chapter 6 it is unsure how the loads that are generated are transferred to their support structures because of great their time-dependency. To gain insight on this, the dynamics of structure have to be taken into account. Additionally can also fatigue life build up be investigated in this manner, which may be of importance in the case of pipelines or monopiles being transported.

Mitigation measures
The influence of mitigation measures to reduce the total loading may be interesting to look into as a cost-effective way of reducing total loads. Possible interesting examples are wedge-shaped caps on the cargo, and when the structural dynamics are regarded the influence of the stiffness and damping of the support structure.

Other cargo geometries
In this thesis only cylindrical cargo has been investigated. Other cargo geometries may also be of interest, such as for example flat plates in the case of mud mats.

Appendix A

Hydrodynamics

In this appendix the theory behind the hydrodynamics that were used in this thesis are explained. First the basics of the dynamic behaviour of a vessel are described. Following, the use of 3D potential theory to determine the hydrodynamic coefficients of cargo barges is shown. Finally it is explained how potential theory can also be used to determine disturbed sea surface elevations that are used in the analysis of relative motions.

Barge dynamics

Motions of floating rigid objects such as vessels and barges can be described by modeling the system as a mass-spring-damper system and using Newton's second law. The equation of motion for the heave motion that of which the system is illustrated in figure A.1a, is given in equation A.1.

$$m\ddot{z} = F_h + F_w \tag{A.1}$$

in which F_h are the hydromechanical reaction forces of the oscillating body in still water and F_w is the wave excitation force on the restrained body.

$$F_h = -a_3\ddot{z} - b_3\dot{z} - c_3 z \tag{A.2}$$

The hydromechanical reaction force is built up out of a frequency dependent added mass term a_3, a restoring term c_3 caused by the displacement of a volume of water and a frequency dependent damping term b_3 due to radiation damping and viscous damping. This is shown in equation A.2. The wave exciting force is composed of the undisturbed incoming wave F_{k3} (Froude-Krylov force) and the diffraction of this wave F_{d3}. Combining equations A.1 and A.2 leads to the equation of motion for a floating body, as shown in equation A.3.

$$(m + a)\,\ddot{z} + b\dot{z} + cz = F_{w3} + F_{d3} \tag{A.3}$$

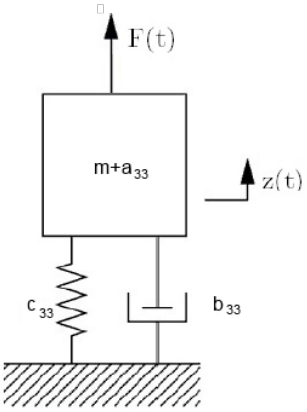

(A) Mass spring damper system for floating rigid bodies

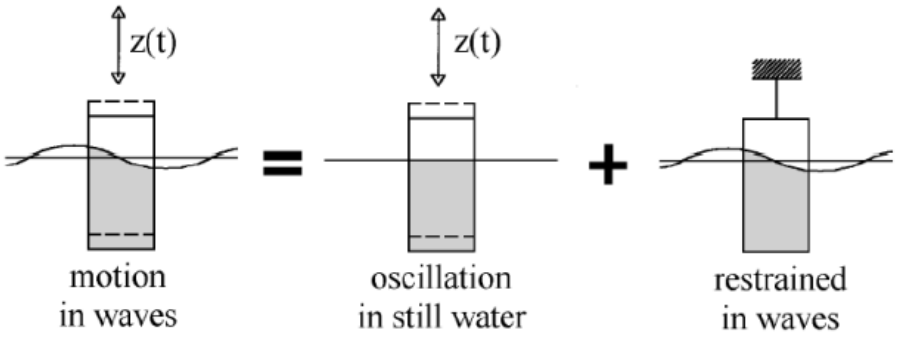

(B) Determination of hydrodynamic forces on floating bodies. From Journee and Massie [2001]

FIGURE A.1: System sketches for floating bodies

When this equation is expanded to all six degrees of freedom of the floating body, the total equation of motion can be written in matrix notation as is shown in equation A.4. Since this is a coupled system, there will exist non-zero terms off the diagonals of the hydrodynamic coefficient matrices.

$$\begin{bmatrix} M+a_{11} & a_{12} & a_{13} & a_{14} & a_{15} & a_{16} \\ a_{21} & M+a_{22} & a_{23} & a_{24} & a_{25} & a_{26} \\ a_{31} & a_{32} & M+a_{33} & a_{34} & a_{35} & a_{36} \\ a_{41} & a_{42} & a_{43} & I_{xx}+a_{44} & a_{45} & a_{46} \\ a_{51} & a_{52} & a_{53} & a_{54} & I_{yy}+a_{55} & a_{56} \\ a_{61} & a_{62} & a_{63} & a_{64} & a_{65} & I_{zz}+a_{66} \end{bmatrix} \cdot \begin{bmatrix} \ddot{x} \\ \ddot{y} \\ \ddot{z} \\ \ddot{\phi} \\ \ddot{\theta} \\ \ddot{\psi} \end{bmatrix} + \begin{bmatrix} b_{11} & b_{12} & b_{13} & b_{14} & b_{15} & b_{16} \\ b_{21} & b_{22} & b_{23} & b_{24} & b_{25} & b_{26} \\ b_{31} & b_{32} & b_{33} & b_{34} & b_{35} & b_{36} \\ b_{41} & b_{42} & b_{43} & b_{44} & b_{45} & b_{46} \\ b_{51} & b_{52} & b_{53} & b_{54} & b_{55} & b_{56} \\ b_{61} & b_{62} & b_{63} & b_{64} & b_{65} & b_{66} \end{bmatrix} \cdot \begin{bmatrix} \dot{x} \\ \dot{y} \\ \dot{z} \\ \dot{\phi} \\ \dot{\theta} \\ \dot{\psi} \end{bmatrix} + \begin{bmatrix} c_{11} & c_{12} & c_{13} & c_{14} & c_{15} & c_{16} \\ c_{21} & c_{22} & c_{23} & c_{24} & c_{25} & c_{26} \\ c_{31} & c_{32} & c_{33} & c_{34} & c_{35} & c_{36} \\ c_{41} & c_{42} & c_{43} & c_{44} & c_{45} & c_{46} \\ c_{51} & c_{52} & c_{53} & c_{54} & c_{55} & c_{56} \\ c_{61} & c_{62} & c_{63} & c_{64} & c_{65} & c_{66} \end{bmatrix} \cdot \begin{bmatrix} x \\ y \\ z \\ \phi \\ \theta \\ \psi \end{bmatrix} = \begin{bmatrix} F_x \\ F_y \\ F_z \\ M_x \\ M_y \\ M_z \end{bmatrix} \tag{A.4}$$

Next, the response of the equation of motion to a regular wave is investigated. For simplicity, here only the heave reponse is shown as an example. When the excitation is described with equation A.5, the steady state response can be given with A.6.

$$F_w = \hat{\zeta} \cos(\omega t + \varepsilon_{f\xi}) \tag{A.5}$$

$$\begin{aligned} z &= \hat{z_a} \cos(\omega t + \varepsilon_{z\xi}) \\ \dot{z} &= -\hat{z_a}\omega \sin(\omega t + \varepsilon_{z\xi}) \\ \ddot{z} &= -\hat{z_a}\omega^2 \cos(\omega t + \varepsilon_{z\xi}) \end{aligned} \tag{A.6}$$

After substitution of equations A.5 and equation A.6 in equation A.3, and equating the in-phase and out-of-phase terms seperately, the amplitude of the motion can be found by computing the modulus of these terms. Subsequently, also the phase shift of the motion with regard to the exciting wave can be found by determining the phase angle of the terms. The amplitude is often written as a fraction of the amplitude of the exciting wave and is known as the RAO. It is a frequency response function that is defined by equation A.7.

This motion RAO has been given for eight different wave headings for all six DOF's in figures A.6 to A.11.

$$RAO(\omega) = \frac{\hat{z}_a}{\hat{\zeta}} = \frac{F_w}{\sqrt{\left(c_3 - \left[M + a_3\right]\omega^2\right)^2 + \left(b_3\omega\right)^2}} \tag{A.7}$$

Determination of hydromechanic coefficients

The hydrodynamic coefficients used in the equations above depend on the submerged geometry of the floating body. Whereas the added mass and damping coefficients are frequency dependent and require extensive computation, the restoring spring coefficients can be determined from a linearized hydrostatic consideration. The added mass and damping coefficients can be determined by full scale or model scale testing, or by using numerical models.

A.0.1 Hydrostatic coefficients

The spring coefficient, or hydrostatic stiffness, is a constant coefficient that can be calculated by equation A.8 [Journee and Massie, 2001]. Because there is no restoring force for the surge, sway, and yaw motion these coefficients are zero.

$$\begin{array}{lrcl} Heave: & c_{33} & = & \rho g A_{wl} \\ Roll: & c_{44} & = & \rho g \nabla \cdot \overline{GM_T} \\ Pitch: & c_{55} & = & \rho g \nabla \cdot \overline{GM_L} \end{array} \tag{A.8}$$

in which:

$\overline{GM_T}$	=	transverse initial metacentric height
$\overline{GM_L}$	=	longitudinal initial metacentric height
∇	=	volume of displaced water per meter of barge length

The volume of displaced water can be calculated from the barge characteristics in table A.1, or automatically from a patch model as will be shown in the next section.

$$\overline{GM} = \overline{KB} + \overline{BM} - \overline{KG} \tag{A.9}$$

in which:

$\overline{GM}$	=	metacentric height
$\overline{KB}$	=	distance from keel to COB
$\overline{BM} = {}^{I}/_{\nabla}$	=	where I is the mass moment of inertia
$\overline{KG}$	=	distance from keel to COG

$$\begin{array}{lcl} I_{xx} & = & k_{xx}^2 \cdot \rho\nabla \\ I_{yy} & = & k_{yy}^2 \cdot \rho\nabla \\ I_{zz} & = & k_{zz}^2 \cdot \rho\nabla \end{array} \tag{A.10}$$

Length	122	m
Depth	7.6	m
Breadth	36.6	m
Draft	3.23	m
k_{xx}	10.8	m
k_{yy}	26.84	m
k_{zz}	26.84	m

TABLE A.1: Barge characteristics

Where the radii of gyration k are given in table A.1.



FIGURE A.2: Photograph of modelled barge

A.0.2 Hydrodynamic coefficients

The wave excitation force consists of two contributions, the Froude-Krilov force F_k and the diffraction force F_d. The Froude-Krilov force is generated by the pressure of the undisturbed incoming wave on the hull of the floating body. Since the incoming wave is disturbed by the presence of the body, the Froude-Krilov force needs to be corrected, which is done by introducing the diffraction force F_d. The forces can be computed by using potential theory, solving the Laplace differential equation and applying Green's theorem. Because this is a very time consuming process, usually numerical models are used for this. An example of such a model is WAMIT.

To determine the motion characteristics of a transport barge, the frequency dependent hydrodynamic coefficients in the equation of motion have to be determined (see appendix A. To do this in an accurate way a model called WAMIT was used. WAMIT[1] is a software tool developed by MIT for the linear analysis of the interaction of surface waves with floating and submerged structures. It assumes the flow around the bodies to be potential and the free surface and boundary conditions are linearized. The mean wetted part of the bodies are approximated by panel models (low-order) or patch models (high-order) for which the distribution of source singularities forms the velocity potential. The pressure distribution is then calculated from the velocity potential and from this parameters such as added mass, damping coefficients and wave forces are determined.
The sensitivity of the accuracy of the results for different patch and panel sizes has previously been investigated. Because the accuracy of the results is nearly insensitive to patch sizes for the high-order method, a 10 m. patch size was used for this study to reduce computation times.

In this appendix the barge motion characteristics as calculated by WAMIT are shown. In addition to the hydrodynamic coefficient matrices, WAMIT also calculates RAO's. These are complex transfer functions that can be used to directly translate sea states to barge motions and they are illustrated in figures A.6 to A.11.

WAMIT uses a panel model as numerical method to calculate the potential flow around the barge body. Based on Green's integral theorem the potential flow is solved by placing pulsating source terms in the center of each panel. A normal vector is defined orthogonal to the panel.

The results of the WAMIT analysis are illustrated in the form of RAO's. It should be noted that viscous damping is not accounted for in these calculations. Since viscous damping usually only accounts for a few percent of the total damping, and is mainly relevant for roll motion, it can be assumed that this does not affect the significance of the results of interest.

[1] `http://www.wamit.com/`

A.0.2.1 Potential theory

One way of finding a solution for the hydrodynamic loads is assuming that the body is floating in an ideal fluid. An implication of this assumption is that the fluid can be described with potential flow. Potential flow is a mathematical concept in which the velocity of the fluid at an arbitrary point in the field in any direction is the derivative of the potential in that direction. The potential function is defined by Φ and the fluid velocities in an arbitrary point are then defined by equation A.11.

$$u = \frac{\partial \Phi}{\partial x} \qquad v = \frac{\partial \Phi}{\partial y} \qquad w = \frac{\partial \Phi}{\partial z} \tag{A.11}$$

To properly describe the desired vessel behaviour, the potentials have to satisfy the boundary conditions as stated in equations A.12 to A.15.

Laplace condition

$$\frac{\partial^2 \Phi}{\partial x^2} + \frac{\partial^2 \Phi}{\partial y^2} + \frac{\partial^2 \Phi}{\partial z^2} = 0 \tag{A.12}$$

Sea bed boundary condition

$$\left.\frac{\partial \Phi}{\partial z}\right|_{z=-h_0} = 0 \tag{A.13}$$

Free surface boundary condition

$$g\frac{\partial \Phi}{\partial z} + \frac{\partial^2 \Phi}{\partial t^2} = 0 \tag{A.14}$$

Body surface condition

$$\frac{\partial \Phi}{\partial n} = \vec{v}.\vec{n} \tag{A.15}$$

According to linear potential theory, the total potential is a superposition of the potentials that originate from the different sources. When regarding floating bodies these are the undisturbed incoming wave Φ_w, the diffracted wave Φ_d, and the radiated waves Φ_r due to the six body motion modes. The resulting potential can then be described by equation A.16.

$$\Phi = \sum_{j=1}^{6} \Phi_{r,j} + \Phi_w + \Phi_d \tag{A.16}$$

The linear potential Φ can written as a space-dependent and a time-dependent term as shown in equation A.17.

$$\Phi(x, y, z, t) = \mathrm{Re}(\phi(x, y, z) \cdot v_a e^{-i\omega t}) \tag{A.17}$$

The time dependent term is defined as the multplication of a complex velocity amplitude v_a and a complex harmonic function. The complex velocity amplitude for potential j can be found by assuming a harmonic displacement in time. This is shown in complex notation in eqation A.18.

$$\begin{aligned} s_j(t) &= s_{a,j} \cdot e^{-i\omega t} \\ v_j(t) &= \dot{s}_j(t) \qquad = -i\omega s_{a,j} \cdot e^{i\omega t} \end{aligned} \tag{A.18}$$

The potentials of the incoming wave Φ_w and the diffracted wave Φ_d relate to the amplitude ζ_0 of the undisturbed incoming wave. The potentials of the radiated waves $\Phi_{r,j}$ relate to the amplitude of the motion of the floating body in the corresponding mode, $s_{a,j}$. The complex velocity amplitude can be taken together with the space dependent part of the potential as is shown in equation A.19.

$$\phi = -i\omega \left\{ (\phi_0 + \phi_7)\, \zeta_0 + \sum_{j=1}^{6} \phi_j s_{a,j} \right\} \tag{A.19}$$

The space-dependent part of the velocity potential of the incoming undisturbed long-crested regular wave is given by equation A.20.

$$\phi_0 = \frac{\zeta_0 g}{\omega} \cdot \frac{\cosh k(h_o + z)}{\cosh kh} \cdot e^{ik(x\cos\mu + y\sin\mu)} \tag{A.20}$$

In which:

ζ	=	Amplitude of undisturbed wave
μ	=	wave direction
h_o	=	distance form the origion of the earth-fixed reference frame to the sea bed
h	=	water depth

The fluid pressure follows from the Bernoulli equation:

$$p = -\rho \frac{\partial \Phi}{\partial t} \tag{A.21}$$

The first order wave exciting forces can then be found by integrating the pressure p over the submerged surface of the body. This is shown in equation A.22. The oscillating forces and moments are given by equation A.23.

$$\begin{aligned} X_k &= -\iint p n_k \cdot dS_0 \\ &= -\rho\omega^2 \zeta_0 e^{-i\omega t} \iint (\phi_0 + \phi_7)\, n_k \cdot dS_0 \end{aligned} \tag{A.22}$$

$$\begin{aligned} F_k &= -\iint p n_k \cdot dS_0 \\ &= -\rho\omega^2 \textstyle\sum_{j=1}^{6} \zeta_j e^{-i\omega t} \iint \phi_j n_k \cdot dS_0 \end{aligned} \tag{A.23}$$

In which:

S_0	=	The submerged surface
n_k	=	direction cosine of surface element dS_0 for the k-mode

A.0.2.2 WAMIT analysis

WAMIT uses a panel model to evaluate the fluid pressures of every surface element. For this thesis an existing model of a 122 m barge was used, which is illustrated in figure A.3. Using this model, an analysis of the hydrodynamic coefficients has been conducted. WAMIT was used to evaluate these coefficients for 8 different wave headings, ranging from 0° to 315° with a constant increment of 45°. Also the angular wave frequency has been ranged from $0.2\,\mathrm{rad\,s^{-1}}$ to $2\,\mathrm{rad\,s^{-1}}$ with an increment of $0.05\,\mathrm{rad\,s^{-1}}$. The results for the added mass and damping coefficients have been illustrated in figures A.4 and A.5 respectively. Note that since WAMIT uses potential theory, viscous effects are not taken into account and therefore the damping coefficient only represents the radiation damping.
The results for the RAO's of the six degrees of freedom have been illustrated in figures A.6 to A.11.

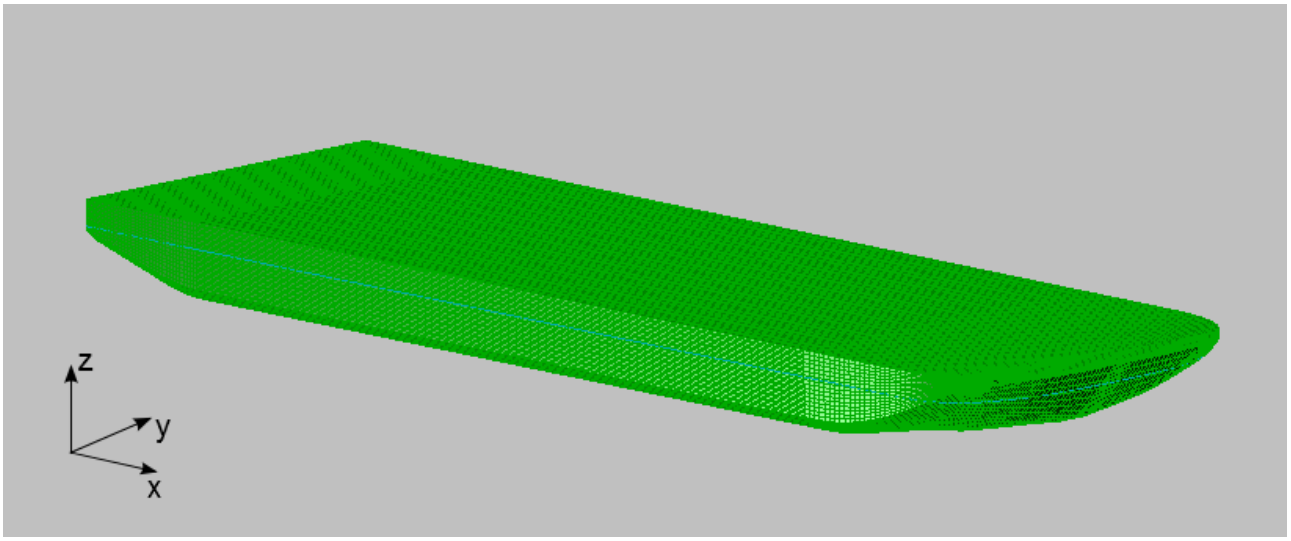

FIGURE A.3: Patch model used in WAMIT calculations

Determination of the free surface elevation

The values of the frequency dependend amplitudes $\hat{z}_a$ and $\hat{\theta}$ and the frequency dependend phase shifts $\varepsilon_{z\eta}$ and $\varepsilon_{\theta\eta}$ as used in section 3.1 can be found by a hydrodynamic analysis as described in this appendix. The value for the sea surface amplitude $\hat{\eta}_a$ equals that of the incoming wave when regarding the undisturbed sea surface, and then $\varepsilon_{\eta\eta}$ can easily be determined by a geometric consideration: $\varepsilon_{\eta\eta} = x_{poi} \cdot k$. This is what is done in the current engineering method. When regarding the disturbed sea surface due to the presence of the barge however, the amplitude $\hat{\eta}_a$ and phase shift $\varepsilon_{\eta\eta}$ can be found by a hydrodynamic analysis by regarding the velocity potential for the boundary condition stated in equation A.24.

$$\eta = -\frac{1}{g}\left(\frac{\partial \phi}{\partial t}\right)_{z=0} \tag{A.24}$$

With the total velocity potential defined as:

$$\phi = \phi_D + i\omega \sum_{j=1}^{6} \eta_j \phi_j \tag{A.25}$$

Where φ_{1-6} are the contributions of the potentials of the radiated wave, induced by the motion of the body in the corresponding degree of freedom.

With:

$$\phi_D = \phi_0 + \phi_S \tag{A.26}$$

Where ϕ_0 is the contribution due to the undisturbed wave and ϕ_S is the contribution due to the scattered wave field, also often written as ϕ_7. The sum, ϕ_D is known as the diffracted velocity potential.

$$\frac{\partial \phi}{\partial t} + \frac{1}{2}V^2 + \frac{p}{\rho} + gz = C(t) \tag{A.27}$$

In which:

$$V^2 = u^2 + v^2 + w^2 = \left(\frac{\partial \phi}{\partial x}\right)^2 + \left(\frac{\partial \phi}{\partial y}\right)^2 + \left(\frac{\partial \phi}{\partial z}\right)^2 \tag{A.28}$$

Since the velocities are considered small, the squared velocities become negligible, and the second term in equation A.27 can be neglected. Because the pressures considered are at the free surface, the z-coordinate equals zero and the third term in equation A.27 also falls out of the equation.

$$\eta = -\frac{1}{g}\frac{p}{-\rho} = \frac{p}{\rho g} \tag{A.29}$$

Wamit determines the velocity potential by solving the Laplace boundary condition for continuity. Using equation A.27 the pressures at the point of interest can be determined. By combining this with

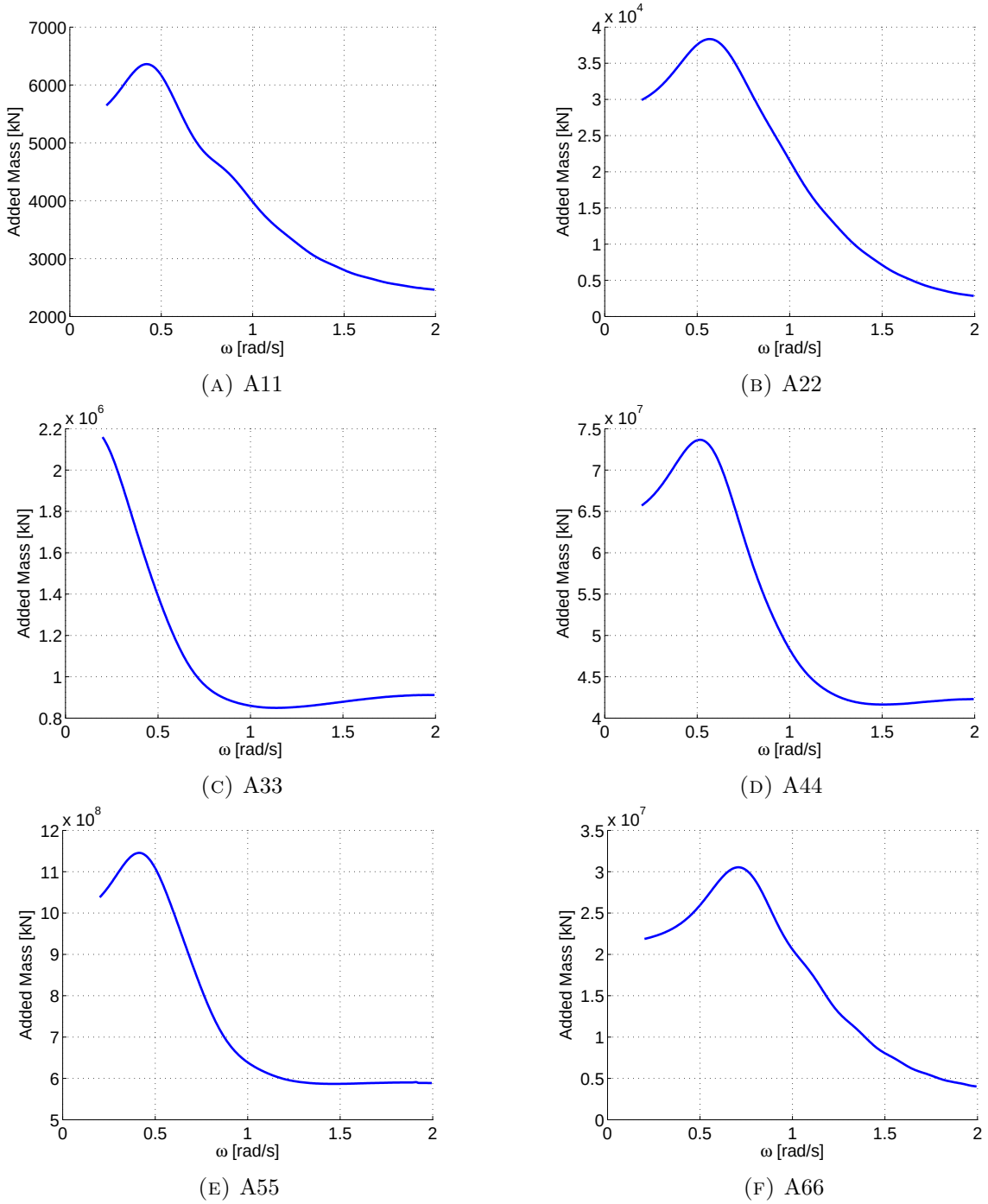

(A) A11 (B) A22

(C) A33 (D) A44

(E) A55 (F) A66

FIGURE A.4: Added mass coefficients

the boundary condition described by equation A.24, equation A.29 can be determined. By solving equation A.29 and combining the real and imaginary parts the amplitude of the free surface with regard to the undisturbed wave can be calculated for different wave frequencies.

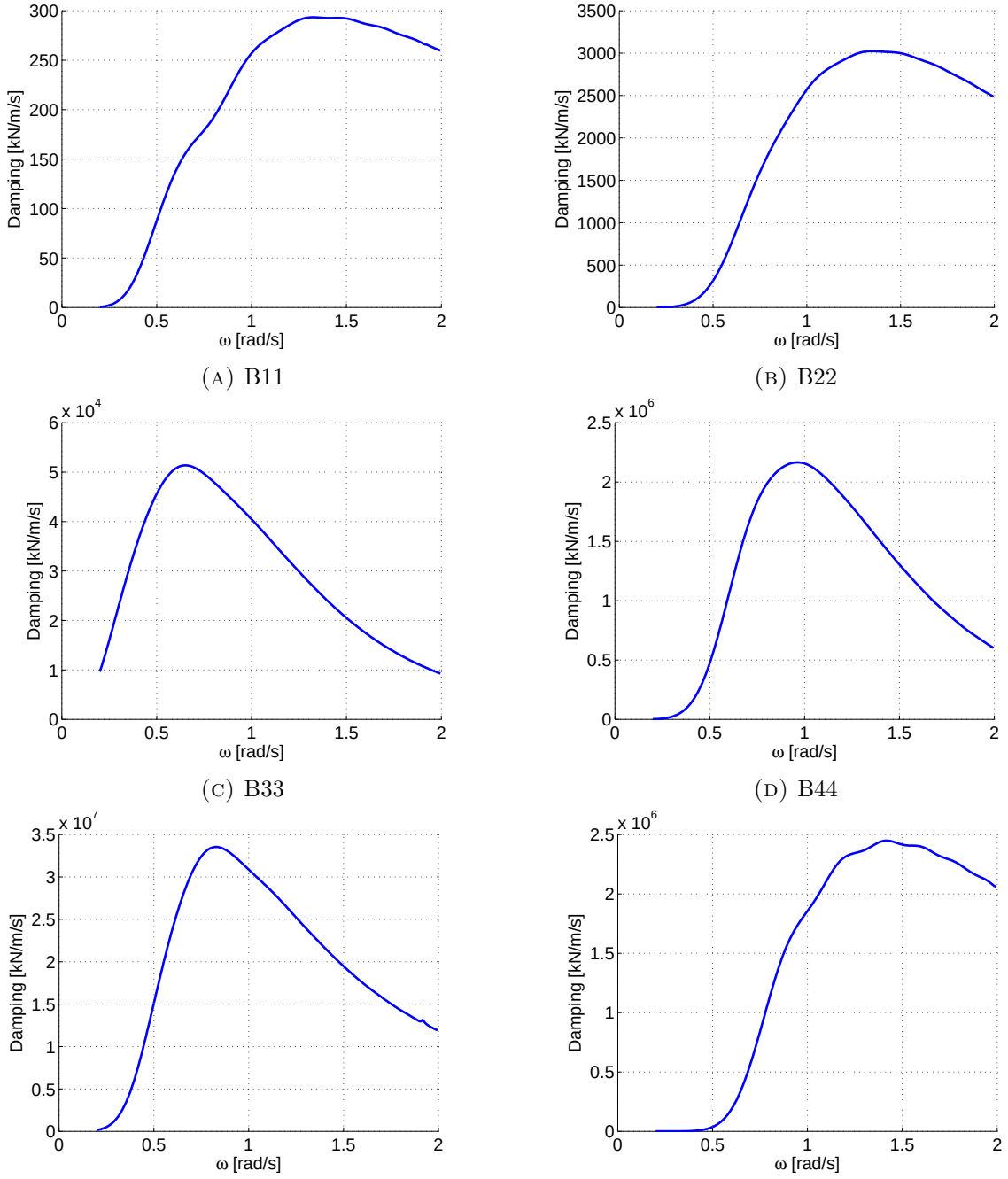

(A) B11 (B) B22

(C) B33 (D) B44

(E) B55 (F) B66

FIGURE A.5: Damping coefficients

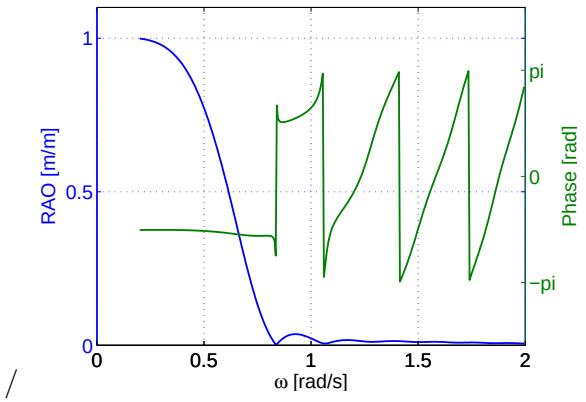

(A) Heading 0°

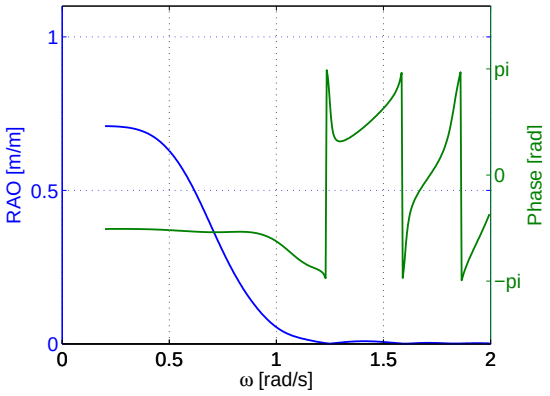

(B) Heading 45°

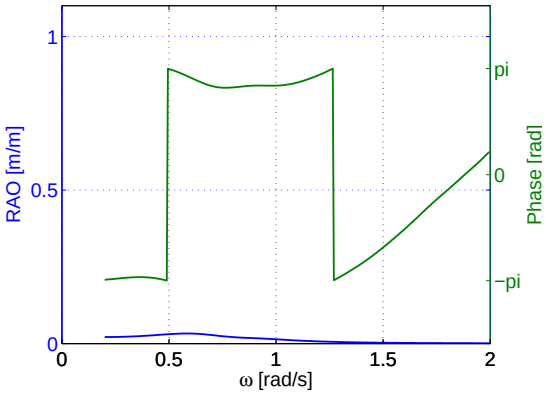

(C) Heading 90°

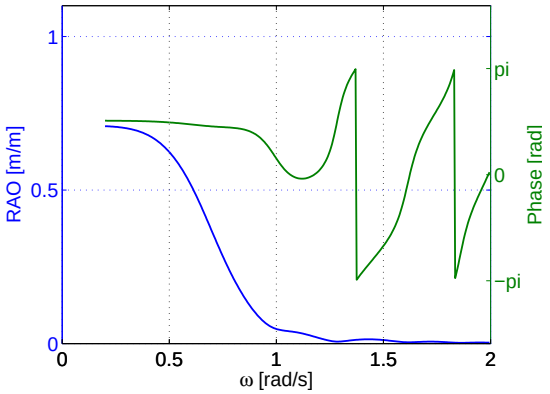

(D) Heading 135°

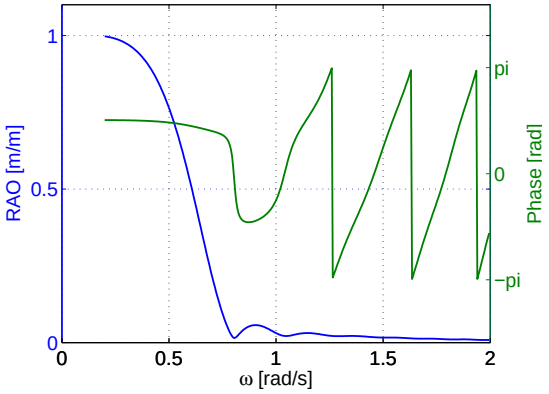

(E) Heading 180°

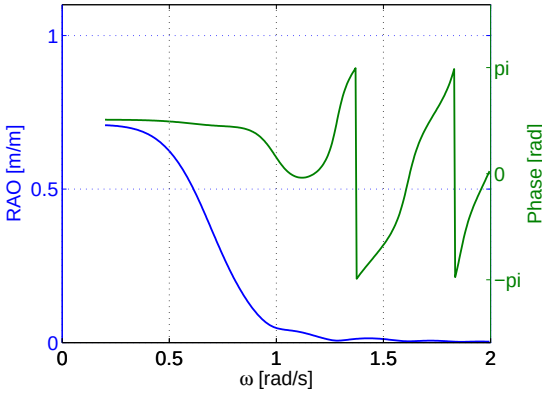

(F) Heading 225°

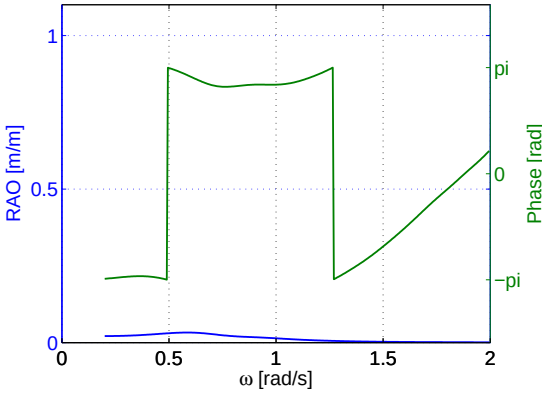

(G) Heading 270°

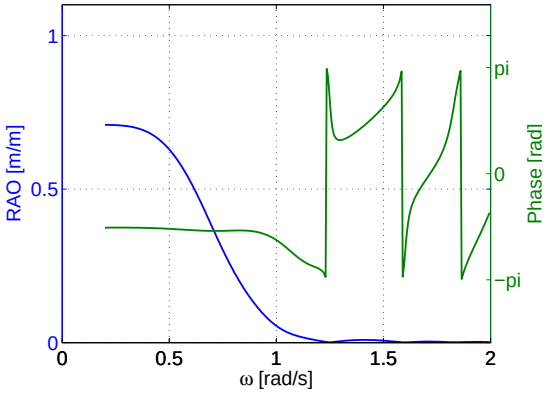

(H) Heading 315°

FIGURE A.6: Surge RAO's

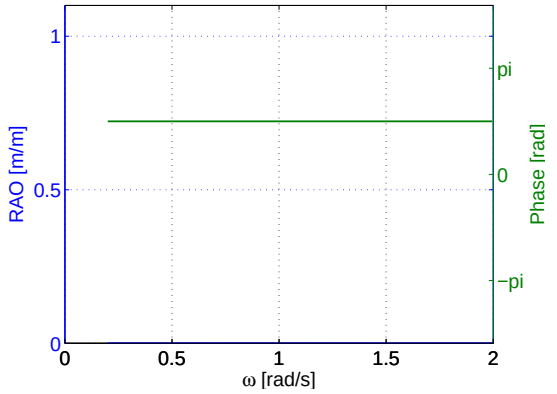

(A) Heading 0°

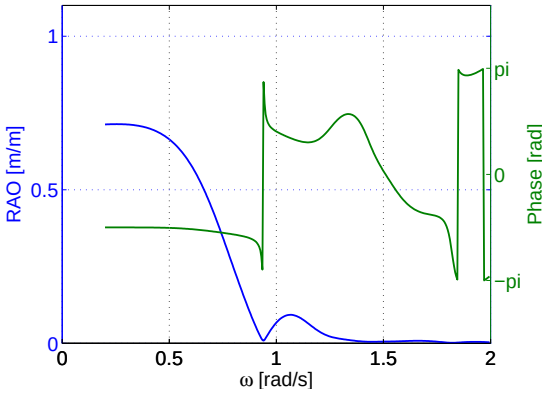

(B) Heading 45°

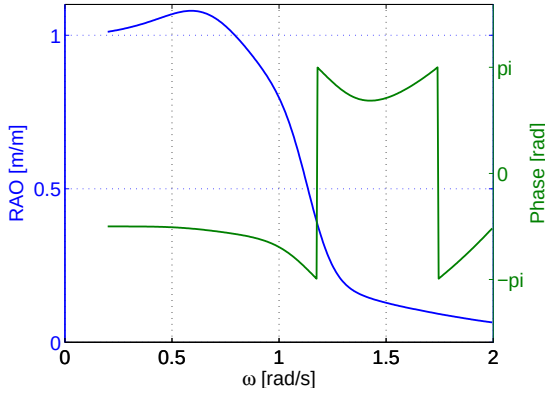

(C) Heading 90°

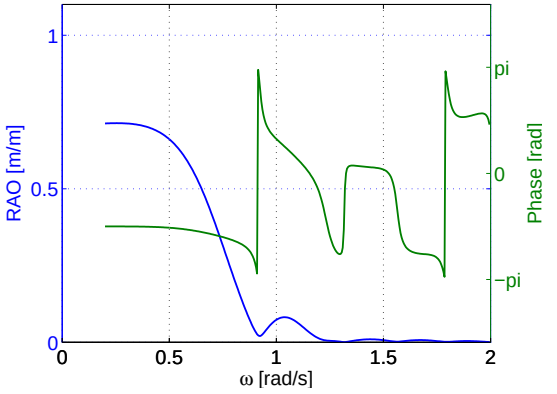

(D) Heading 135°

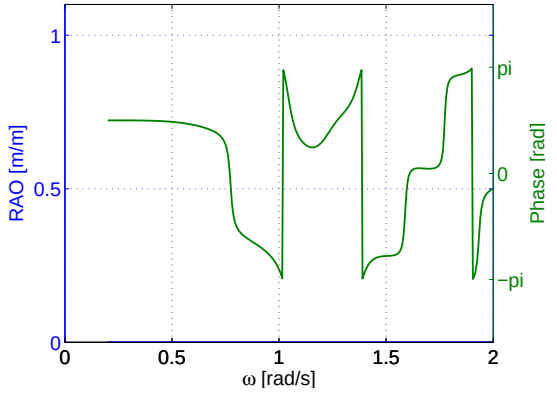

(E) Heading 180°

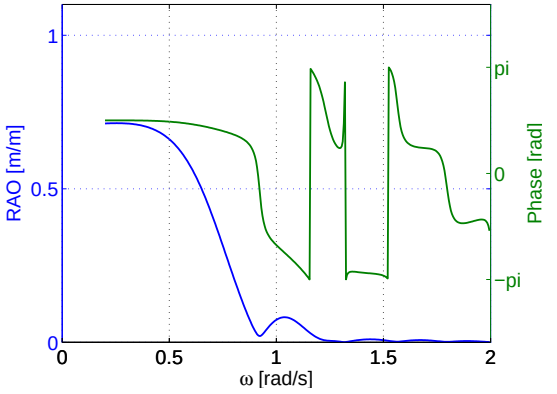

(F) Heading 225°

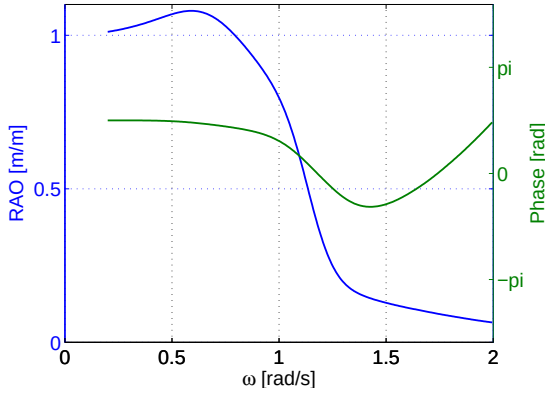

(G) Heading 270°

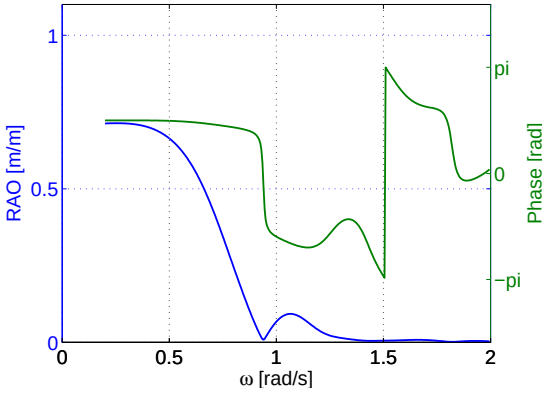

(H) Heading 315°

FIGURE A.7: Sway RAO's

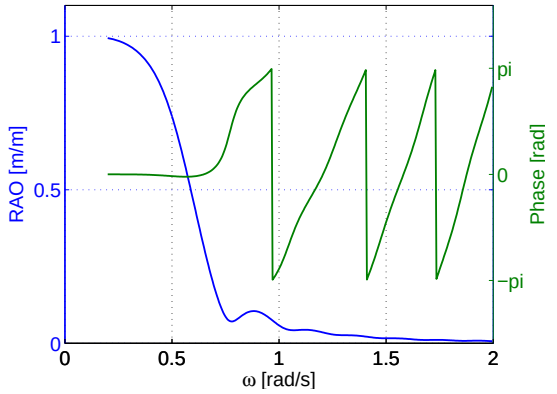

(A) Heading 0°

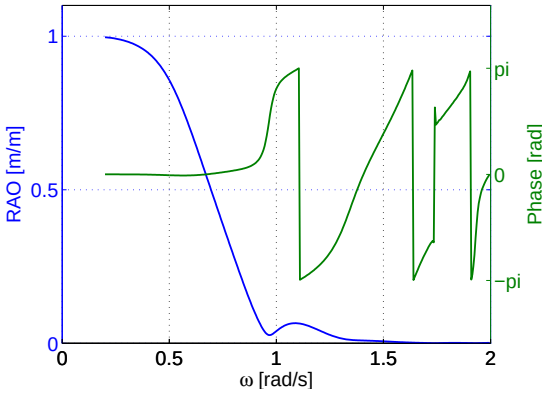

(B) Heading 45°

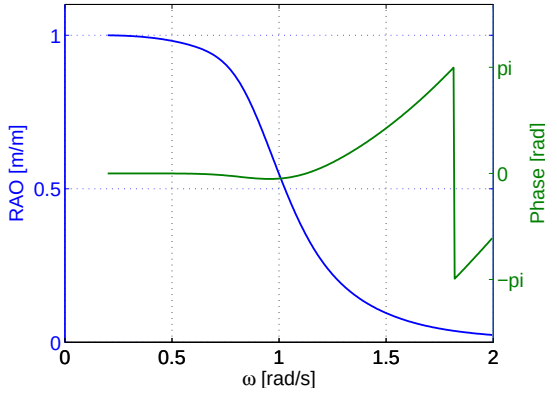

(C) Heading 90°

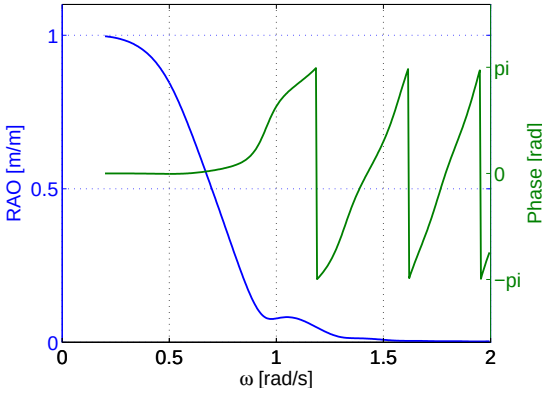

(D) Heading 135°

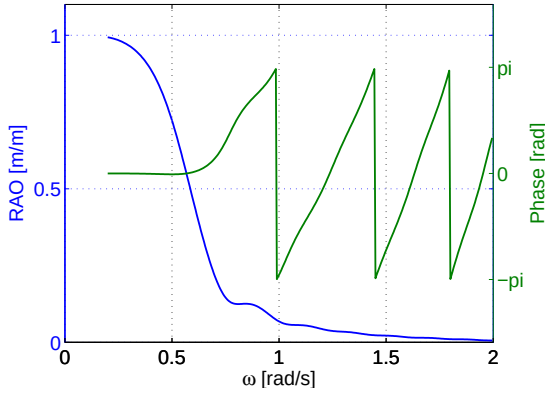

(E) Heading 180°

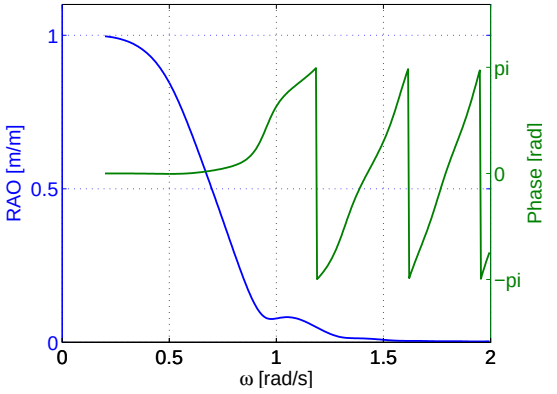

(F) Heading 225°

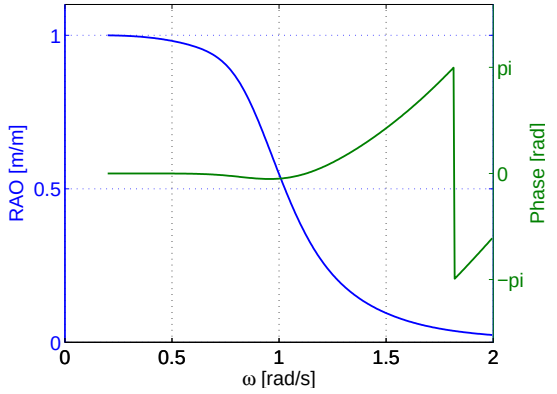

(G) Heading 270°

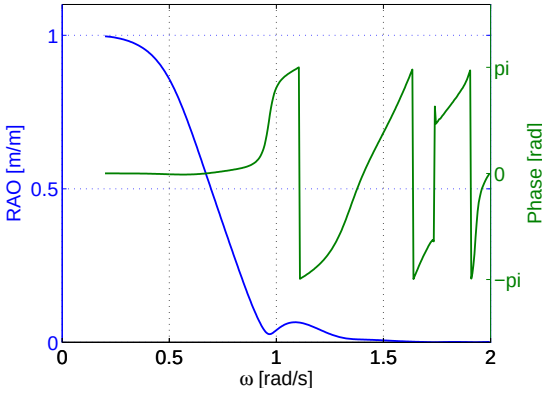

(H) Heading 315°

FIGURE A.8: Heave RAO's

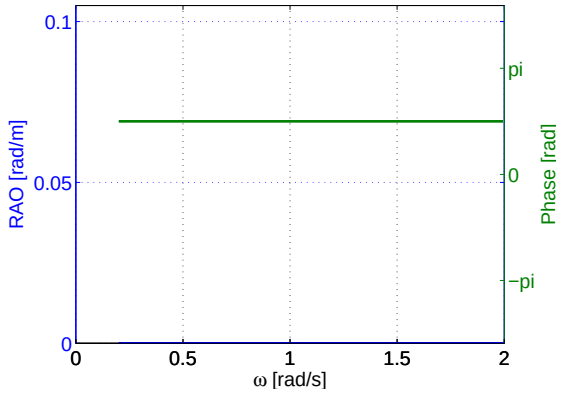

(A) Heading 0°

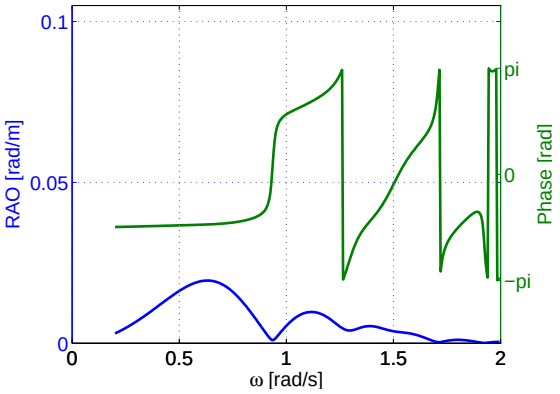

(B) Heading 45°

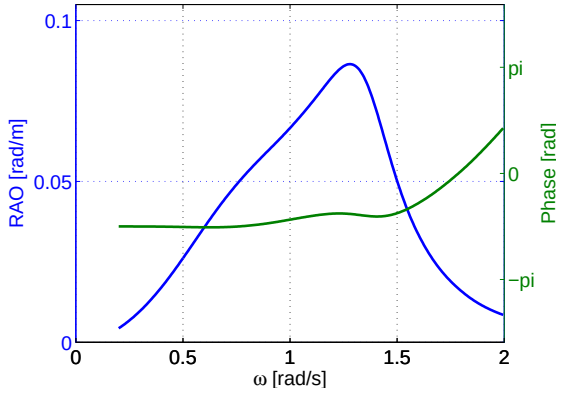

(C) Heading 90°

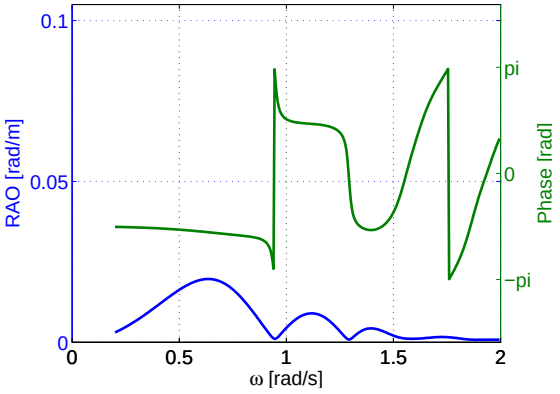

(D) Heading 135°

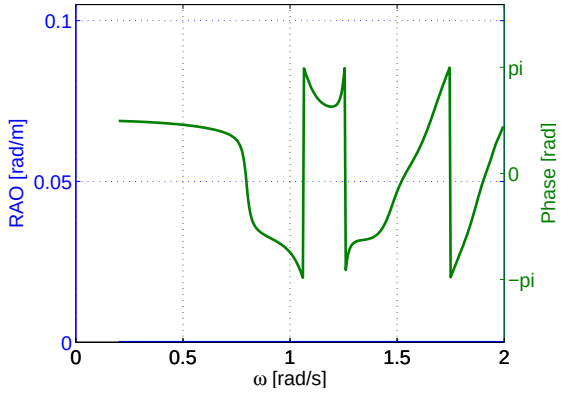

(E) Heading 180°

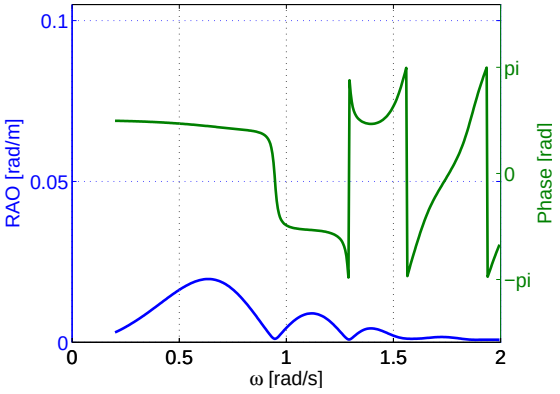

(F) Heading 225°

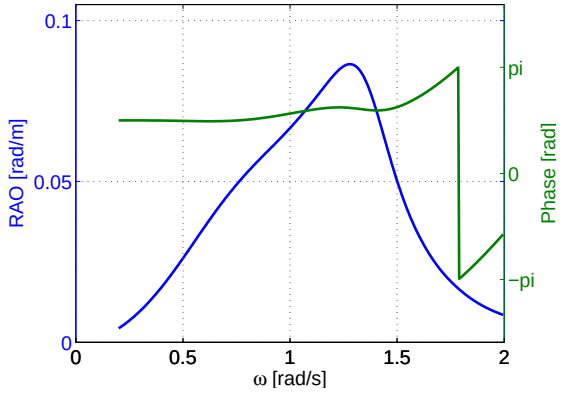

(G) Heading 270°

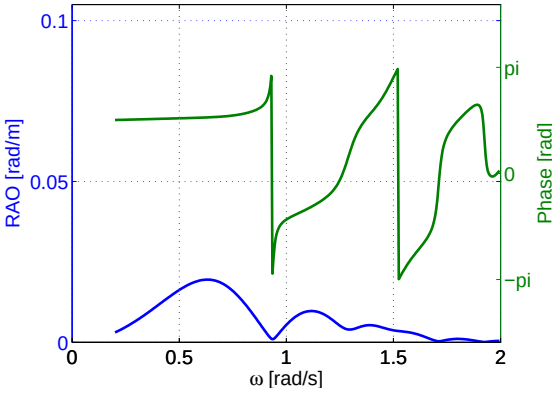

(H) Heading 315°

FIGURE A.9: Roll RAO's

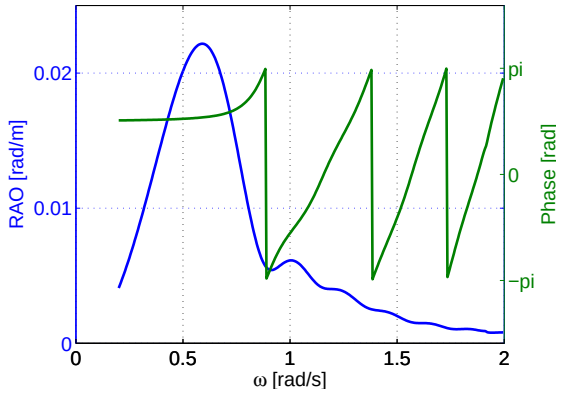

(A) Heading 0°

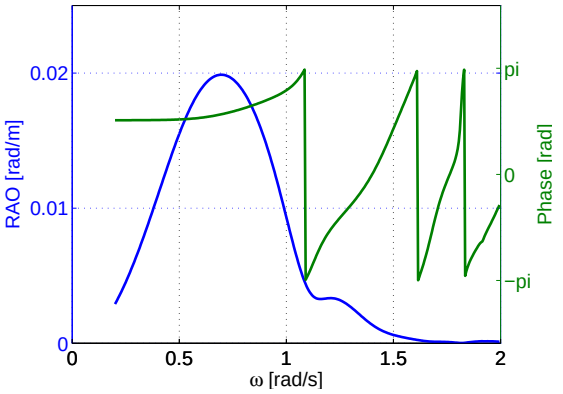

(B) Heading 45°

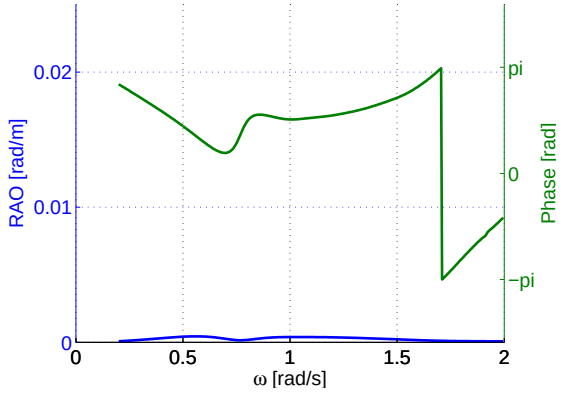

(C) Heading 90°

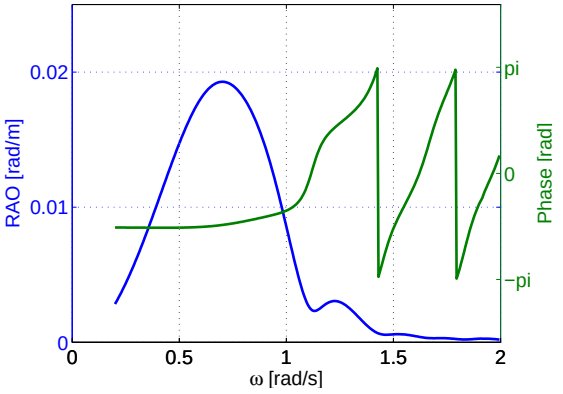

(D) Heading 135°

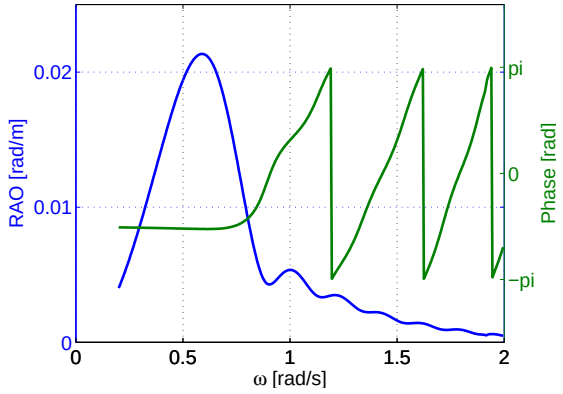

(E) Heading 180°

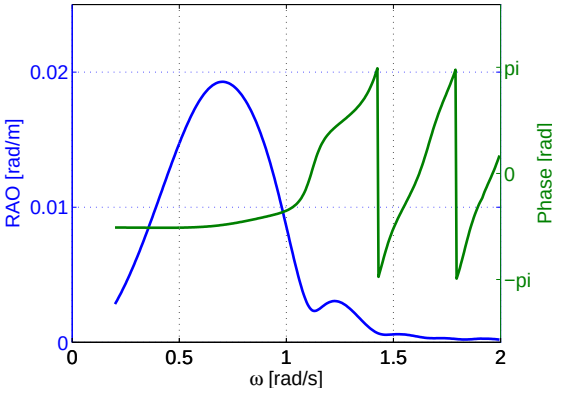

(F) Heading 225°

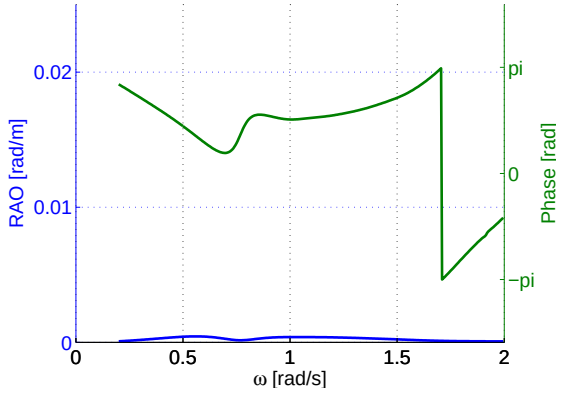

(G) Heading 270°

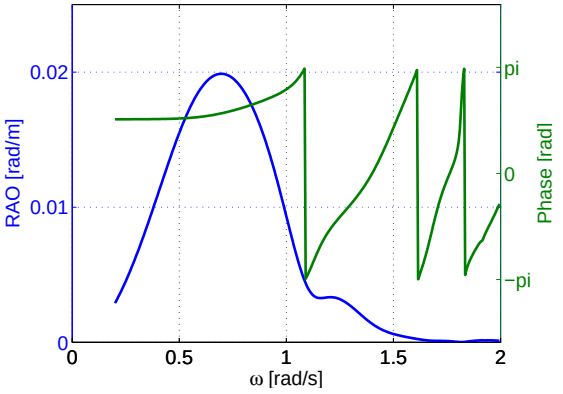

(H) Heading 315°

FIGURE A.10: Pitch RAO's

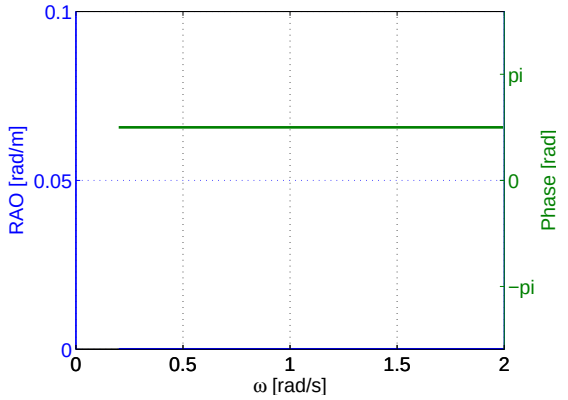

(A) Heading 0°

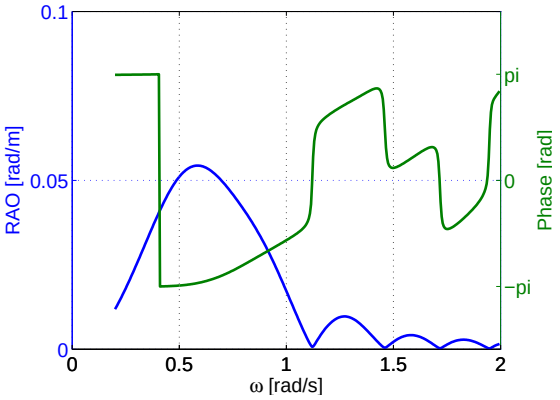

(B) Heading 45°

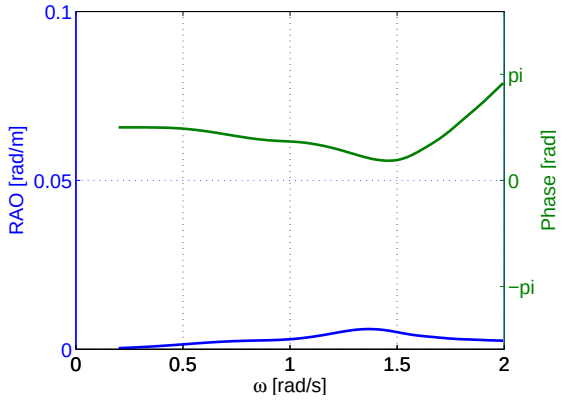

(C) Heading 90°

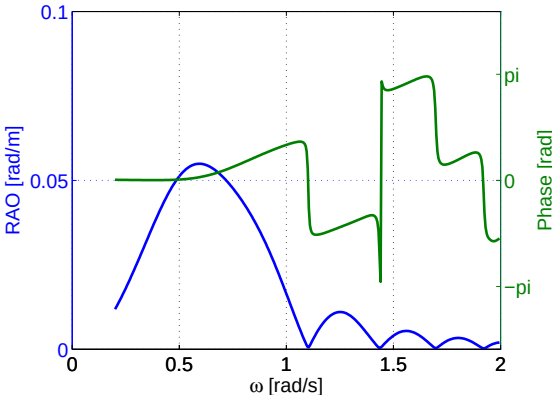

(D) Heading 135°

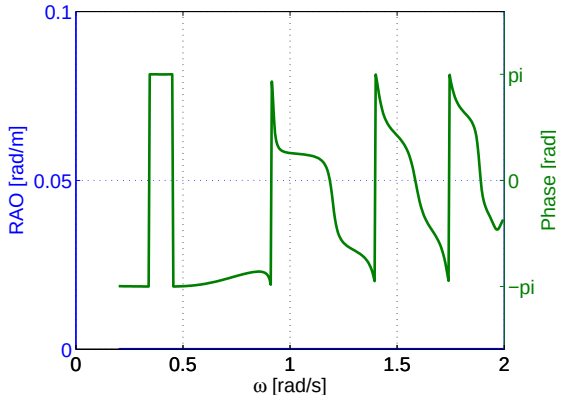

(E) Heading 180°

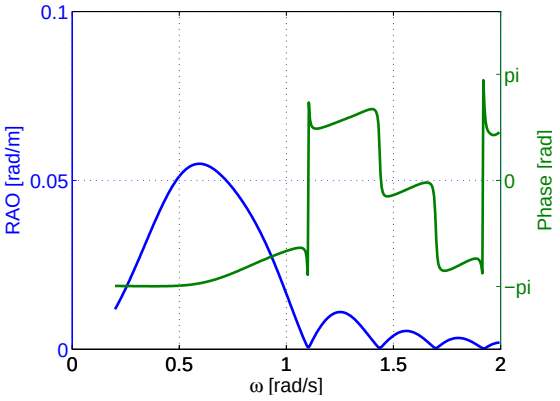

(F) Heading 225°

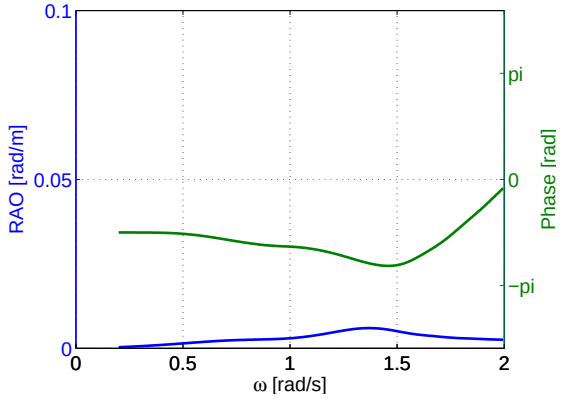

(G) Heading 270°

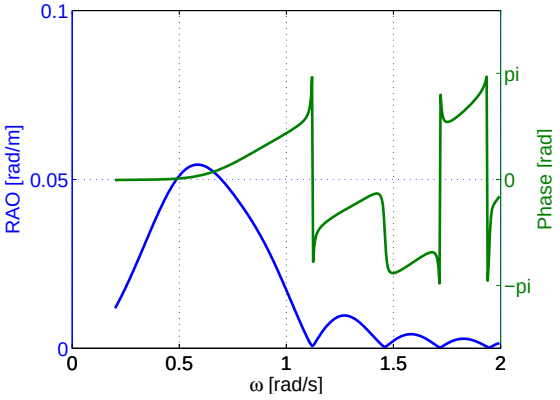

(H) Heading 315°

FIGURE A.11: Yaw RAO's

Appendix B

RAO plots

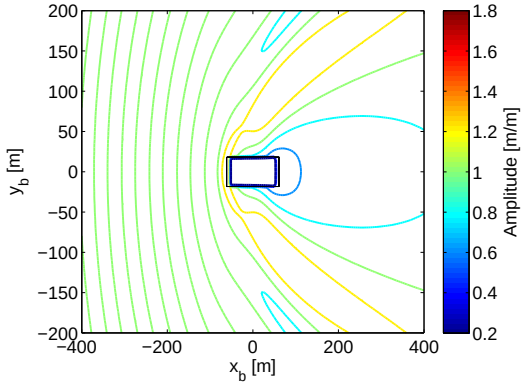

(A) Heading 0° amplitudes

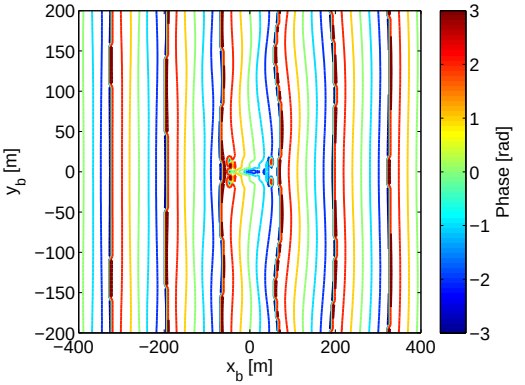

(B) Heading 0° phase shifts

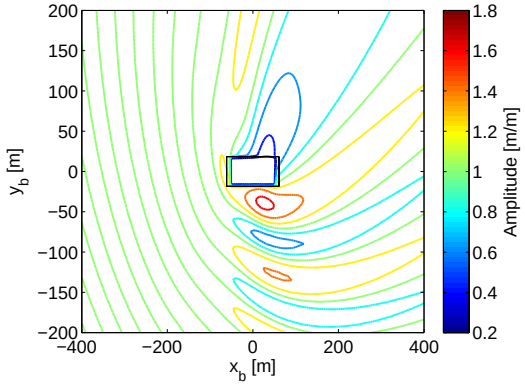

(C) Heading 45° amplitudes

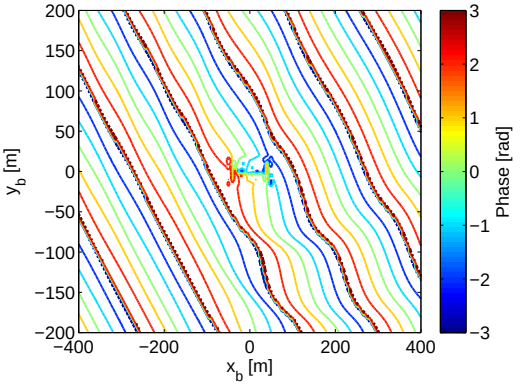

(D) Heading 45° phase shifts

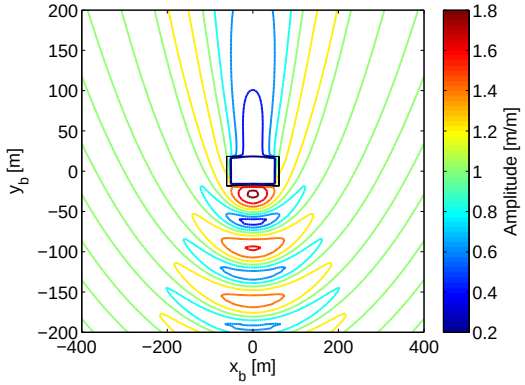

(E) Heading 90° amplitudes

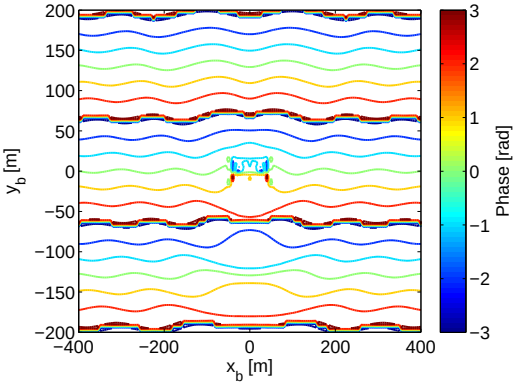

(F) Heading 90° phase shifts

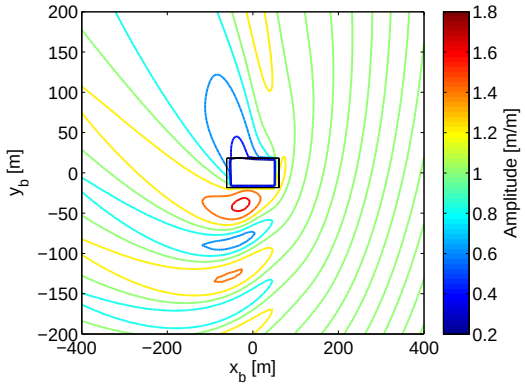

(G) Heading 135° amplitudes

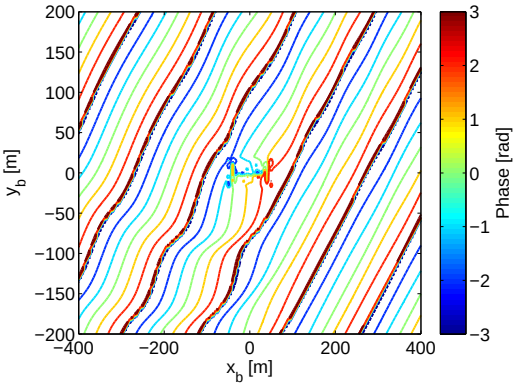

(H) Heading 135° phase shifts

FIGURE B.1: Amplitudes and phase shifts of sea surface elevation due to diffraction at $\omega = 0.69\,\mathrm{rad\,s^{-1}}$ ($T = 9.11\,\mathrm{s}$) for headings 0°, 45°, 90°, and 135°. Amplitudes and phase shifts are relative to an incident unit wave at the same frequency.

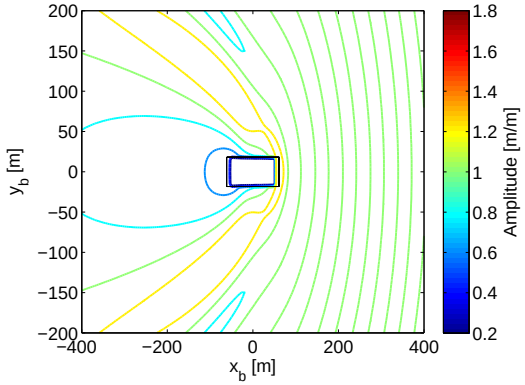

(A) Heading 180° amplitudes

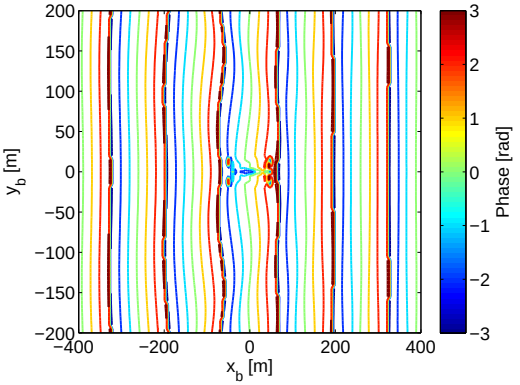

(B) Heading 180° phase shifts

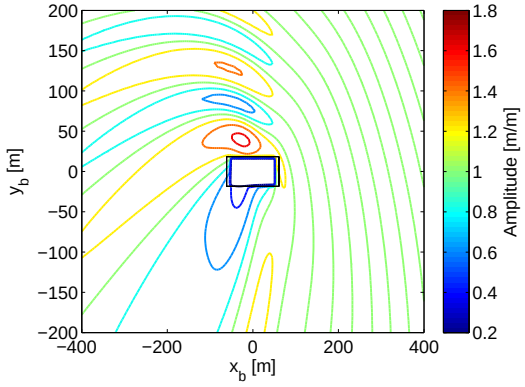

(C) Heading 225° amplitudes

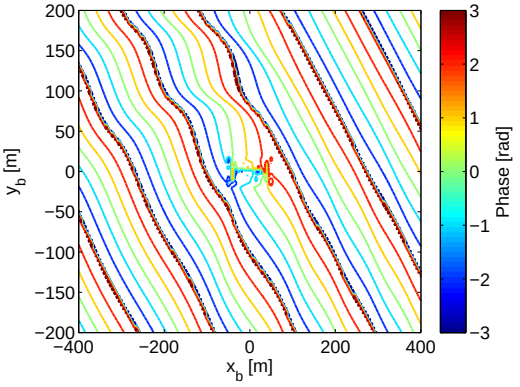

(D) Heading 225° phase shifts

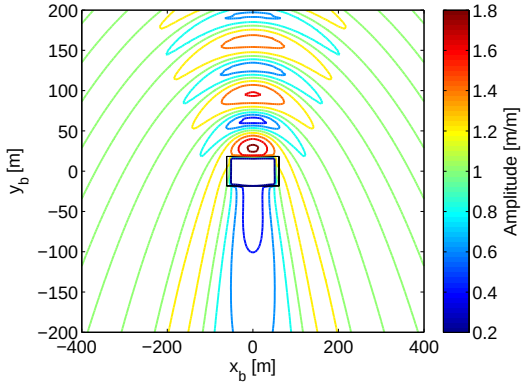

(E) Heading 270° amplitudes

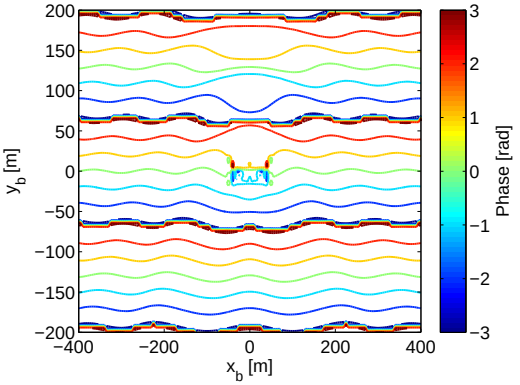

(F) Heading 270° phase shifts

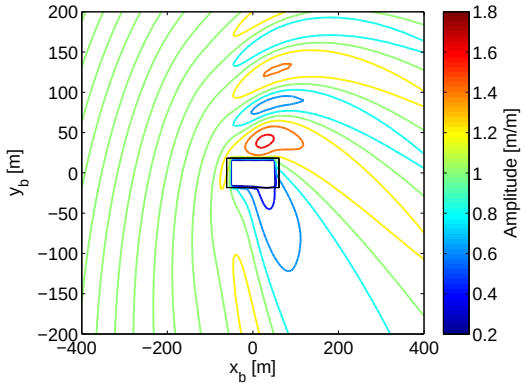

(G) Heading 315° amplitudes

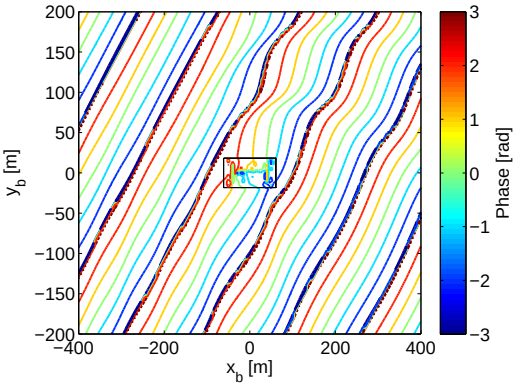

(H) Heading 315° phase shifts

FIGURE B.2: Amplitudes and phase shifts of sea surface elevation due to diffraction at $\omega = 0.69\,\mathrm{rad\,s^{-1}}$ ($T = 9.11\,\mathrm{s}$) for headings 180°, 225°, 270°, and 315°. Amplitudes and phase shifts are relative to an incident unit wave at the same frequency.

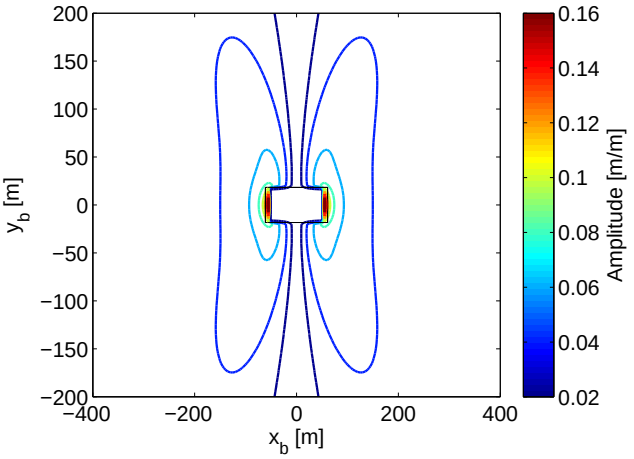

(A) Surge radiation amplitudes

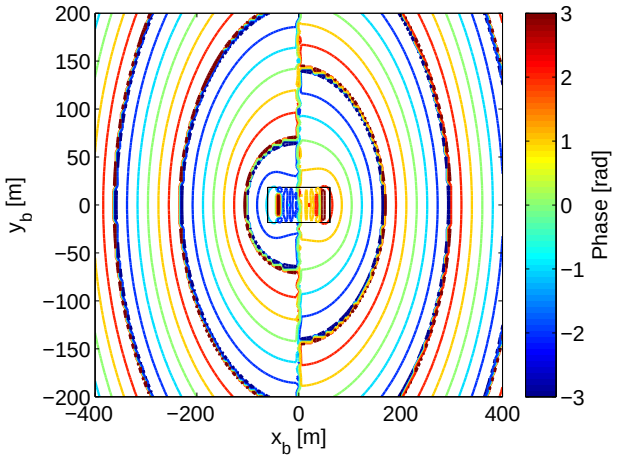

(B) Surge radiation phase shifts

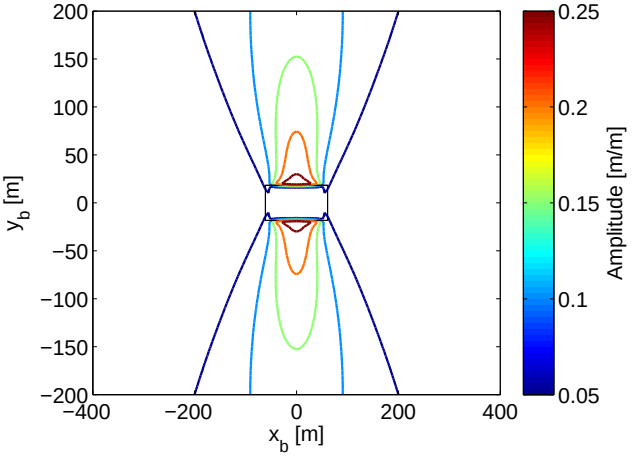

(C) Sway radiation amplitudes

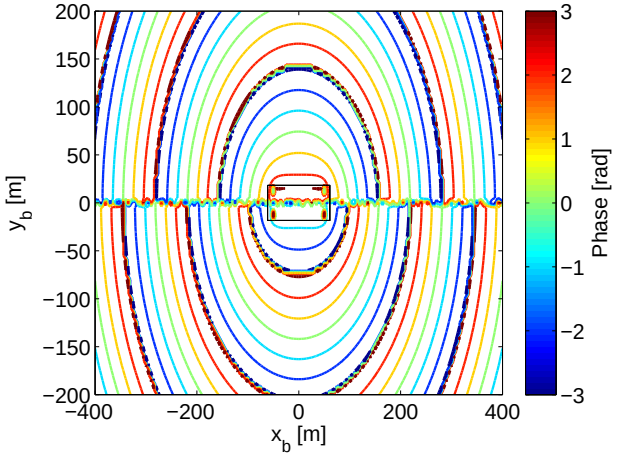

(D) Sway radiation phase shifts

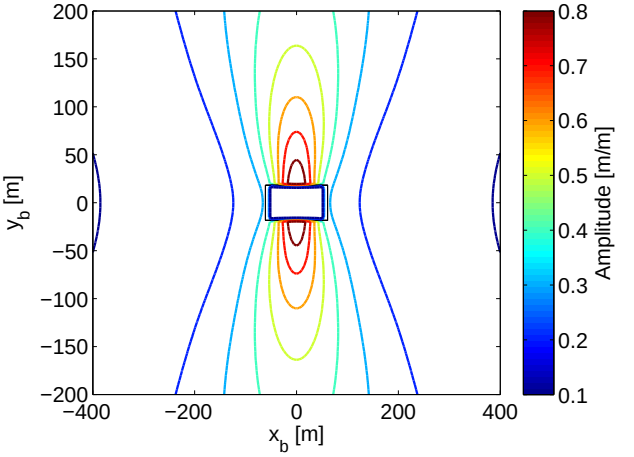

(E) Surge radiation amplitudes

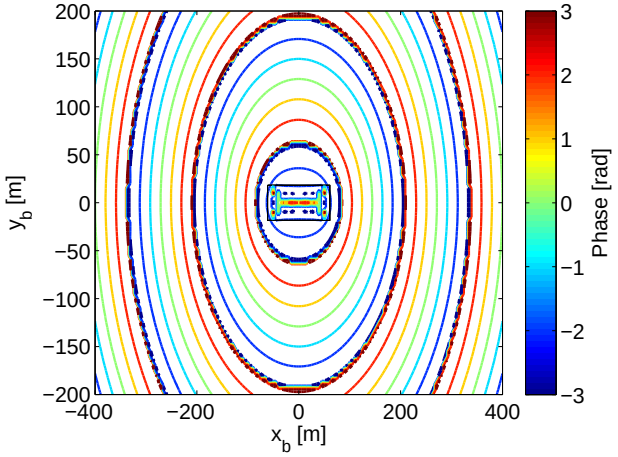

(F) Heave radiation phase shifts

FIGURE B.3: Amplitudes and phase shifts of sea surface elevation due to radiation of translation motions at $\omega = 0.69\,\mathrm{rad\,s^{-1}}$ ($T = 9.11\,\mathrm{s}$). Amplitudes and phase shifts are relative to their corresponding motion at the same frequency.

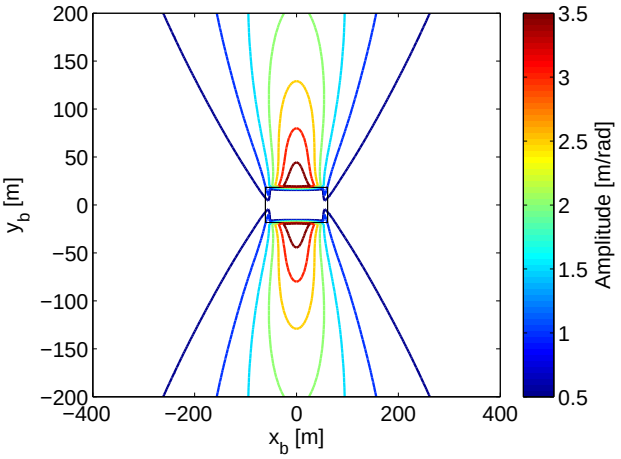

(A) Roll radiation amplitudes

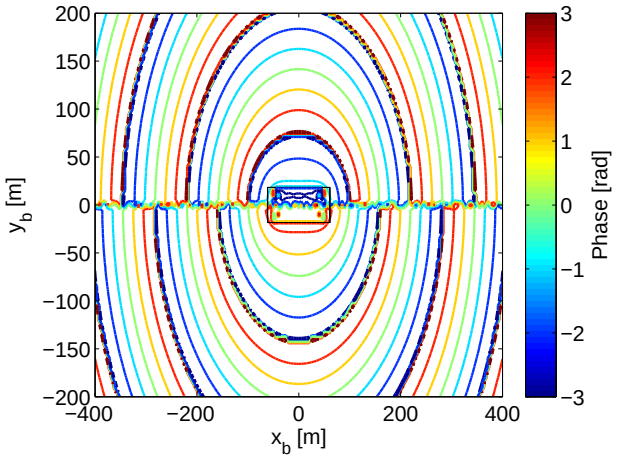

(B) Roll radiation phase shifts

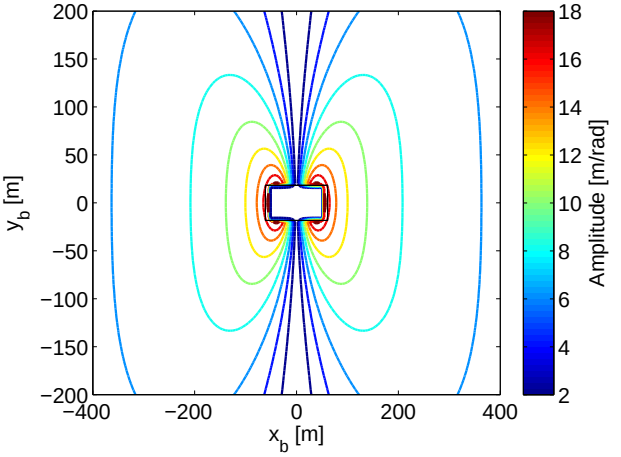

(C) Pitch radiation amplitudes

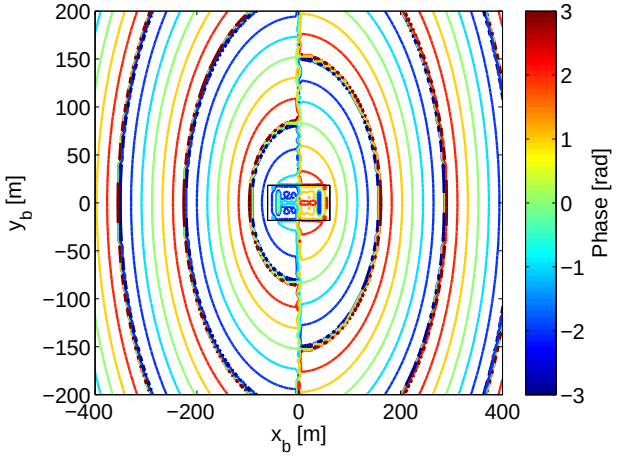

(D) Pitch radiation phase shifts

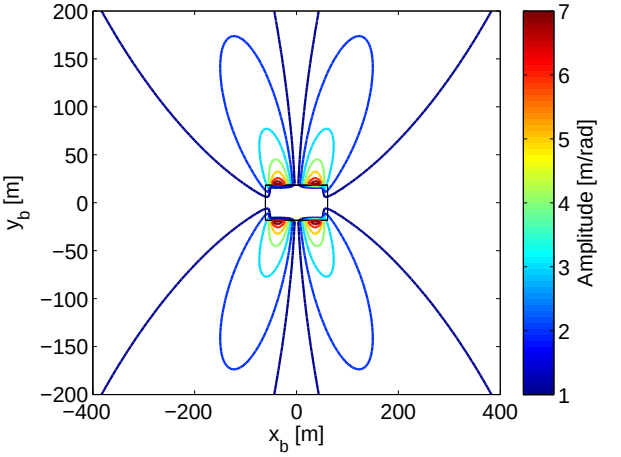

(E) Yaw radiation amplitudes

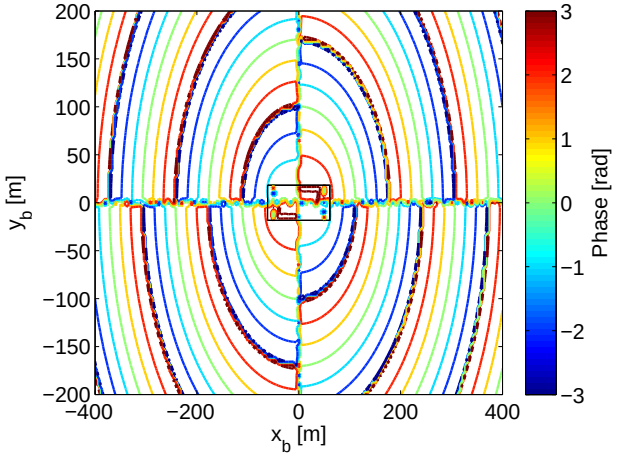

(F) Yaw radiation phase shifts

FIGURE B.4: Amplitudes and phase shifts of sea surface elevation due to radiation of rotation motions at $\omega = 0.69\,\mathrm{rad\,s^{-1}}$ ($T = 9.11\,\mathrm{s}$). Amplitudes and phase shifts are relative to their corresponding motion at the same frequency.

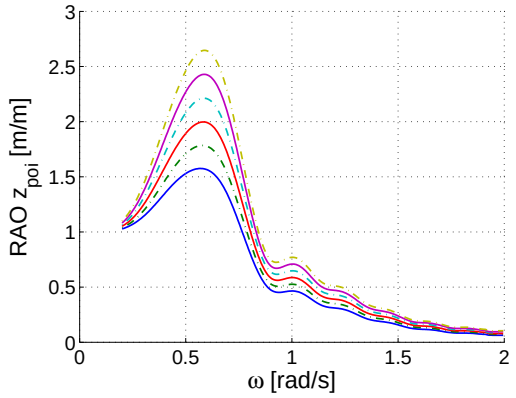

(A) Heading 0°

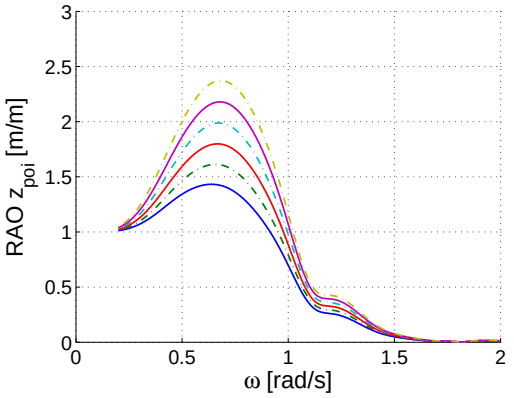

(B) Heading 45°

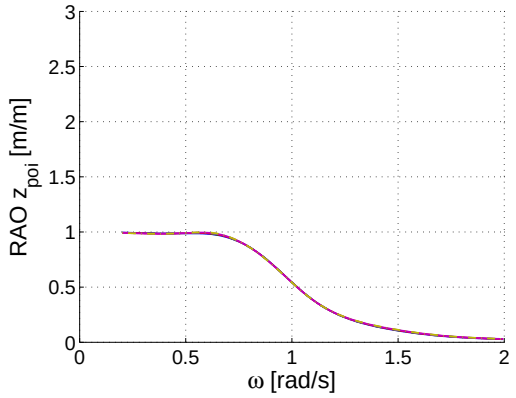

(C) Heading 90°

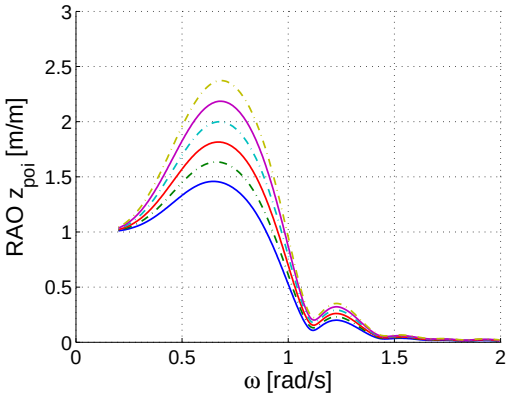

(D) Heading 135°

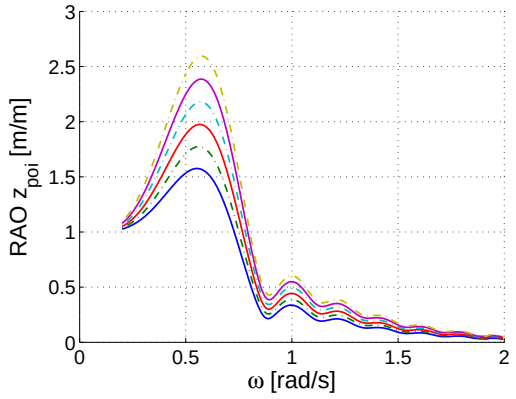

(E) Heading 180°

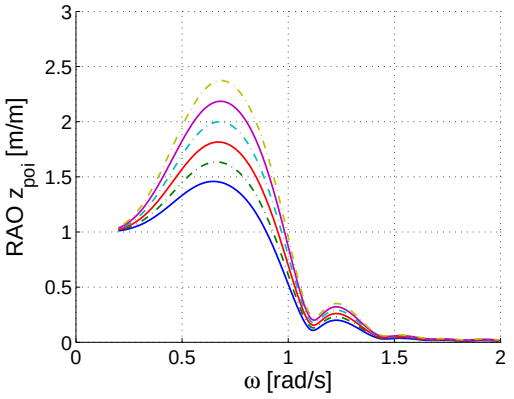

(F) Heading 225°

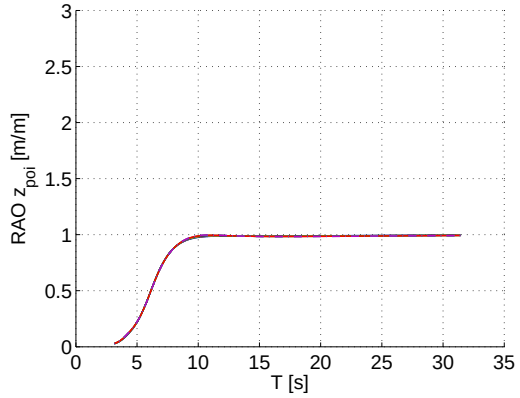

(G) Heading 270°

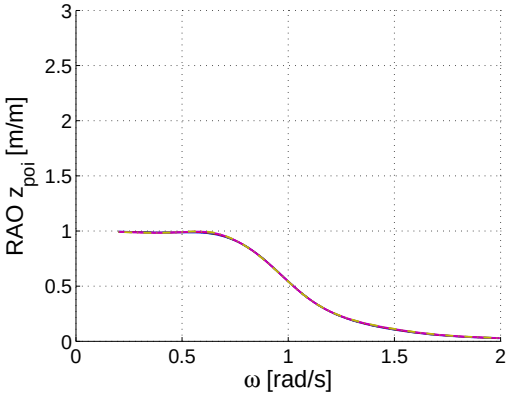

(H) Heading 315°

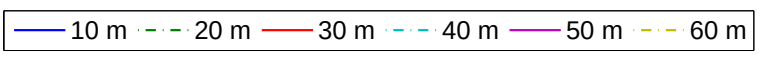

FIGURE B.5: RAO's of z_{poi}

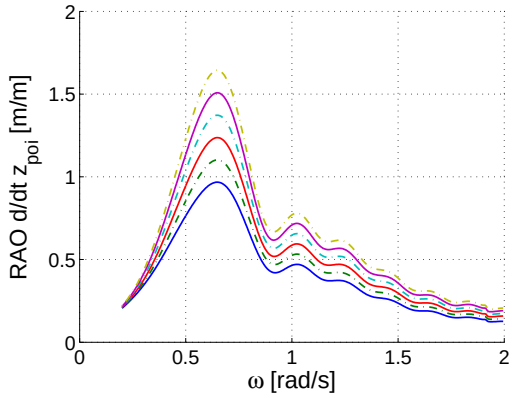

(A) Heading 0°

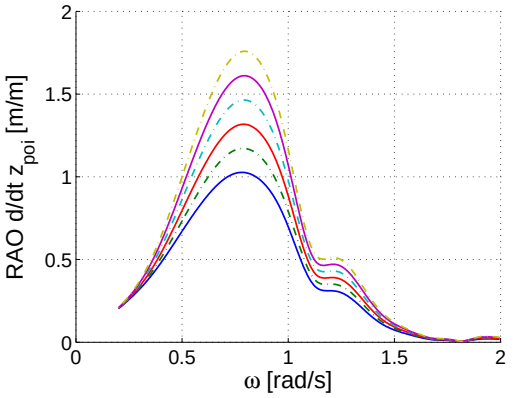

(B) Heading 45°

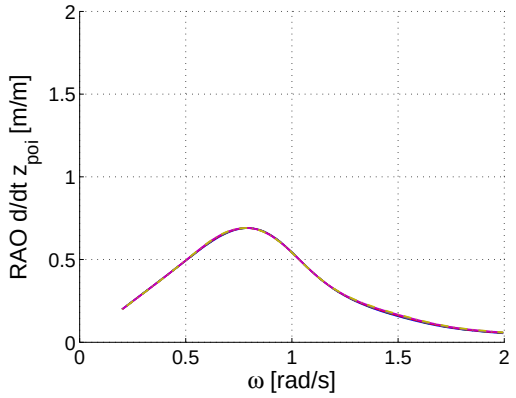

(C) Heading 90°

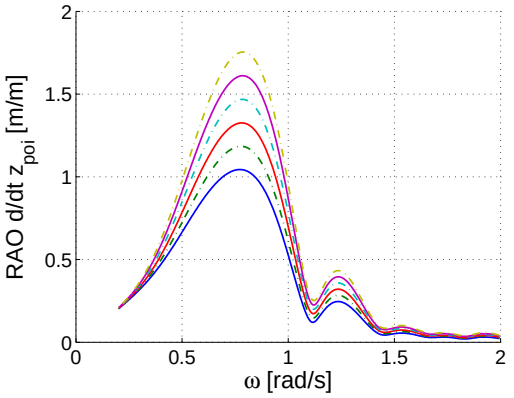

(D) Heading 135°

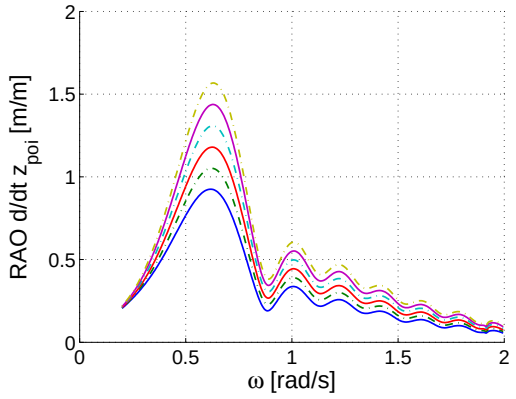

(E) Heading 180°

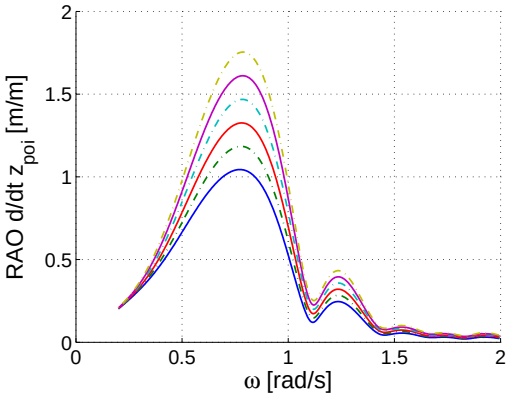

(F) Heading 225°

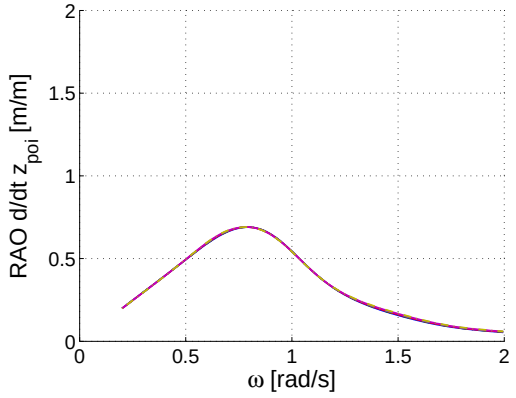

(G) Heading 270°

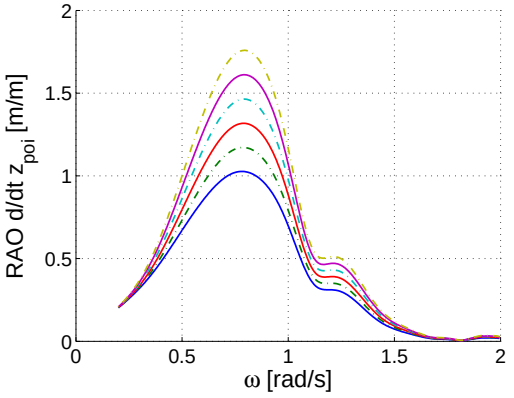

(H) Heading 315°

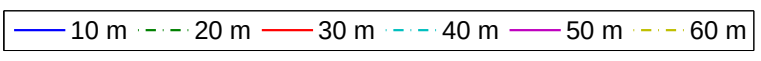

FIGURE B.6: RAO's of $^{d}/_{dt}z_{poi}$

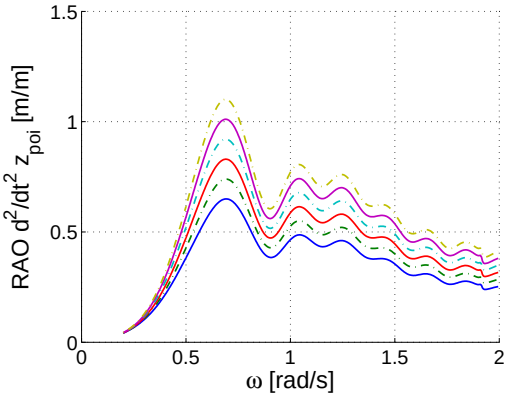

(A) Heading 0°

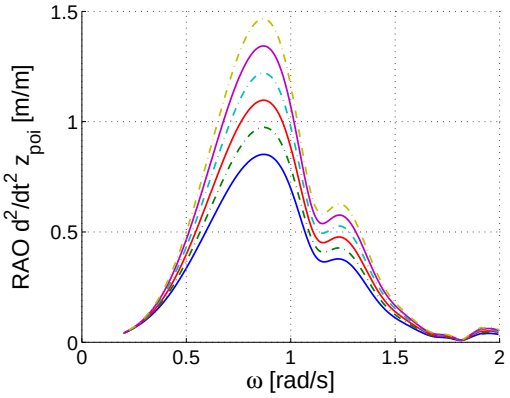

(B) Heading 45°

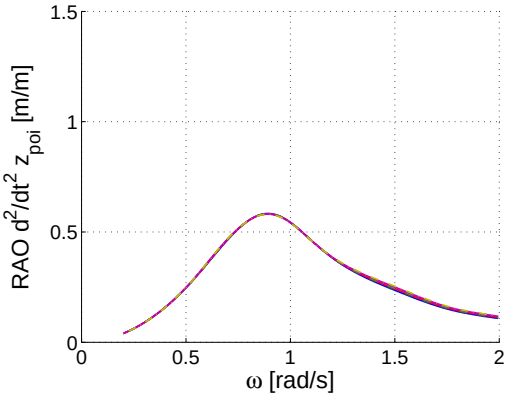

(C) Heading 90°

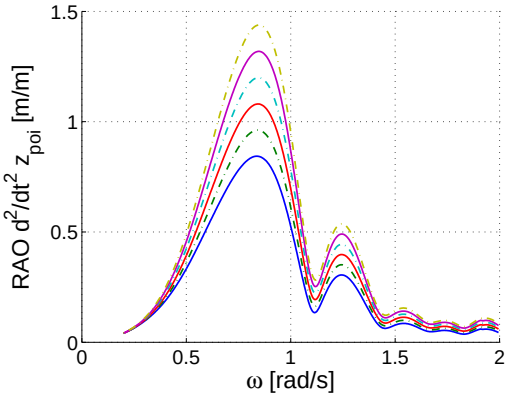

(D) Heading 135°

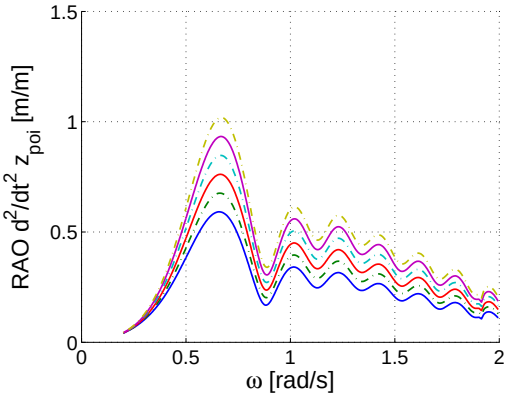

(E) Heading 180°

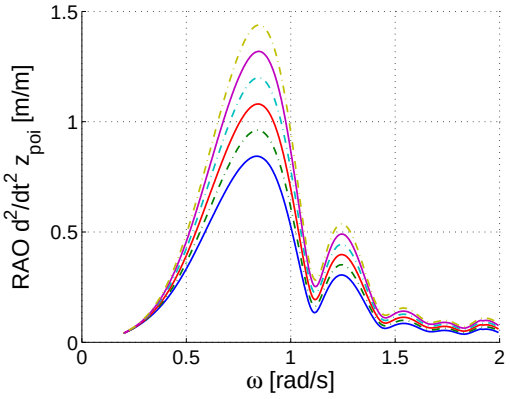

(F) Heading 225°

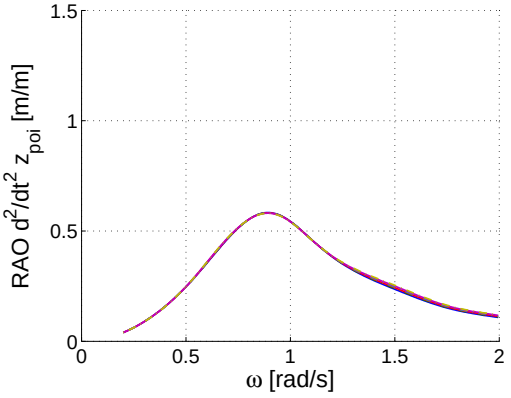

(G) Heading 270°

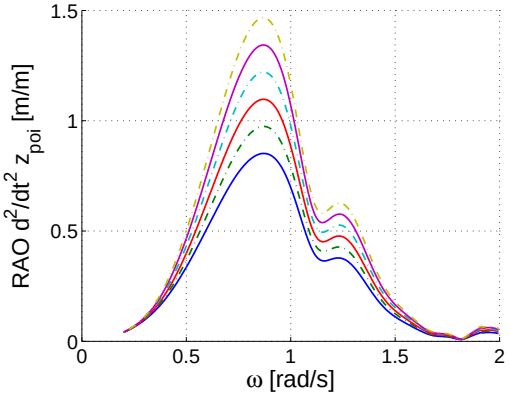

(H) Heading 315°

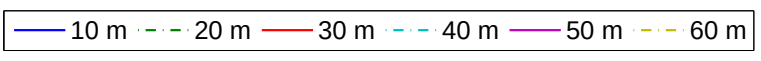

FIGURE B.7: RAO's of $^{d^2}/_{dt^2} z_{poi}$

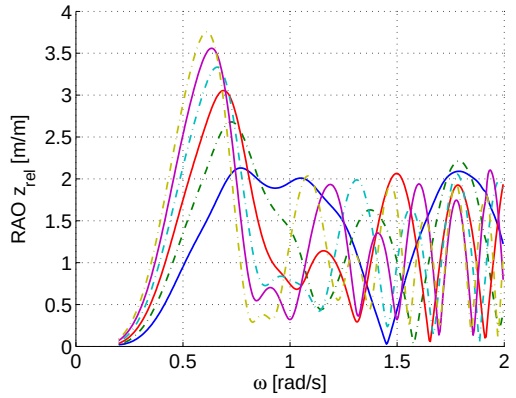

(A) Heading 0°

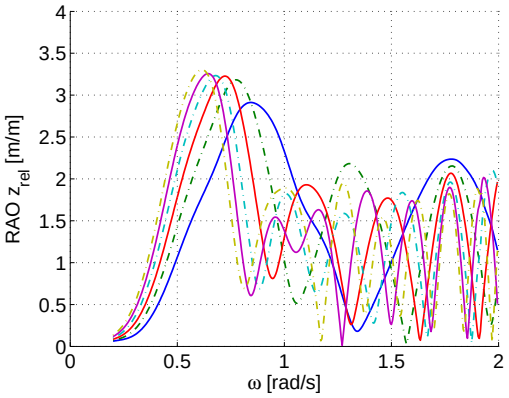

(B) Heading 45°

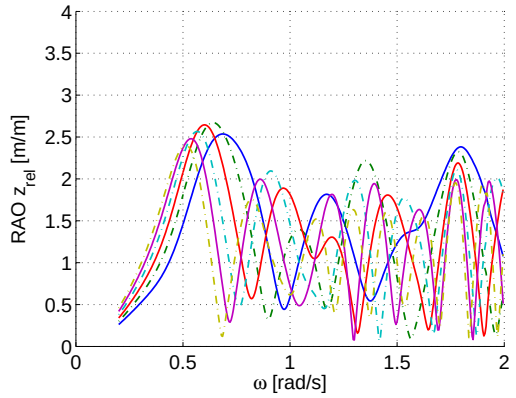

(C) Heading 90°

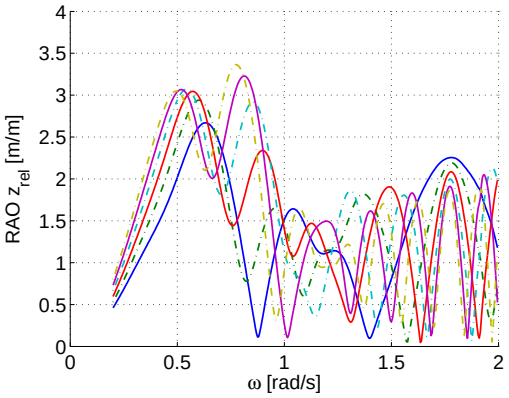

(D) Heading 135°

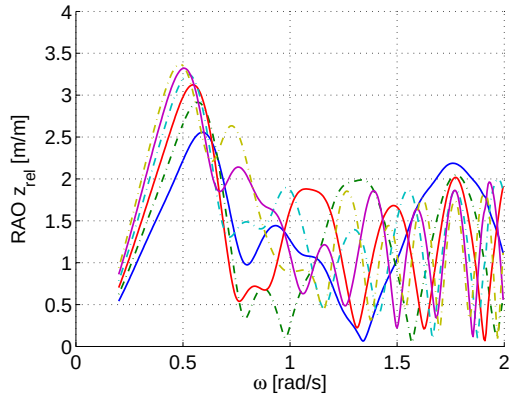

(E) Heading 180°

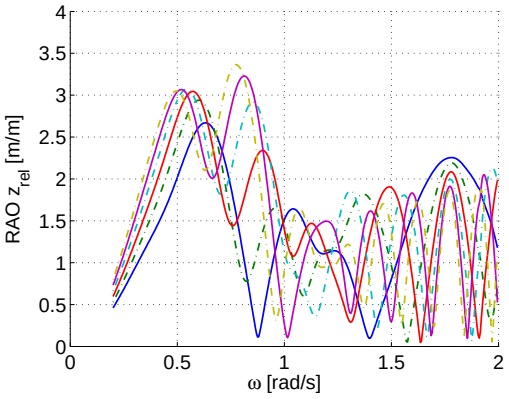

(F) Heading 225°

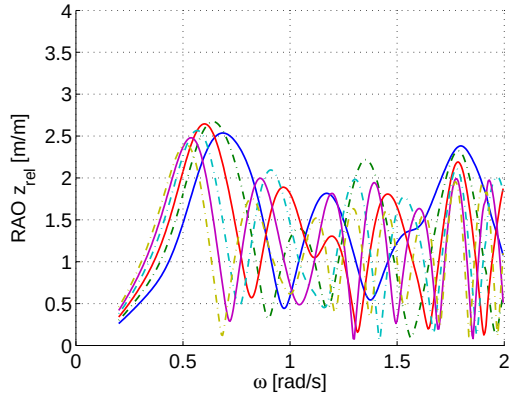

(G) Heading 270°

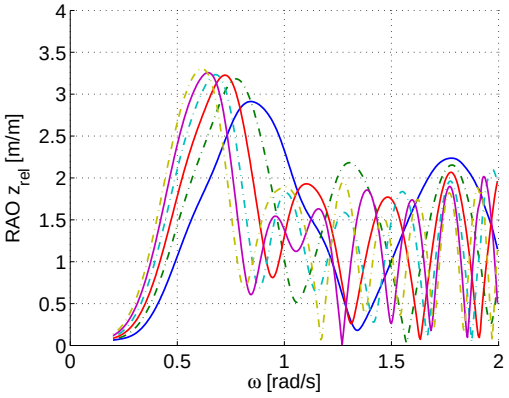

(H) Heading 315°

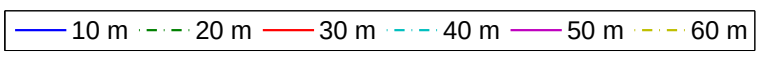

FIGURE B.8: RAO's of z_{rel} for a disturbed approach

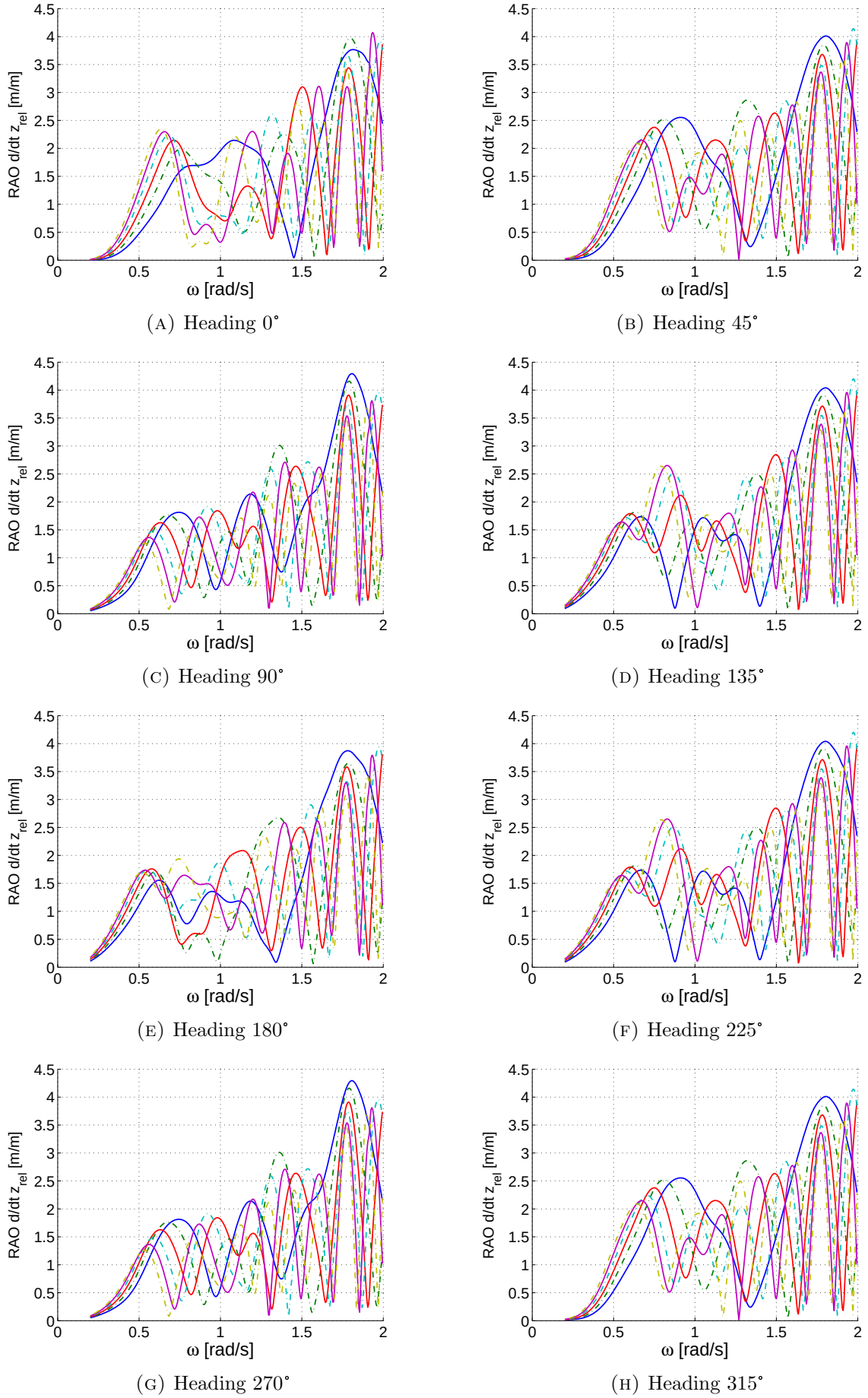

(A) Heading 0°

(B) Heading 45°

(C) Heading 90°

(D) Heading 135°

(E) Heading 180°

(F) Heading 225°

(G) Heading 270°

(H) Heading 315°

FIGURE B.9: RAO's of $^{d}/_{dt}z_{rel}$ for a disturbed approach

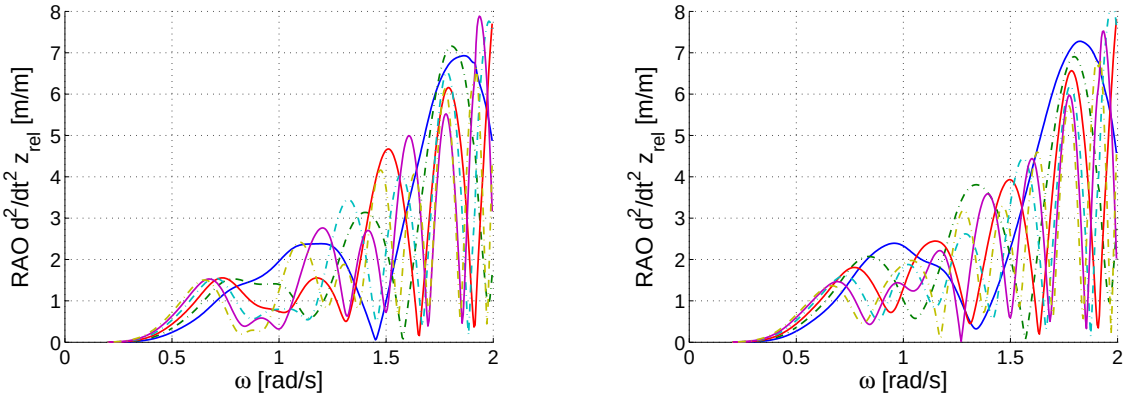

(A) Heading 0°

(B) Heading 45°

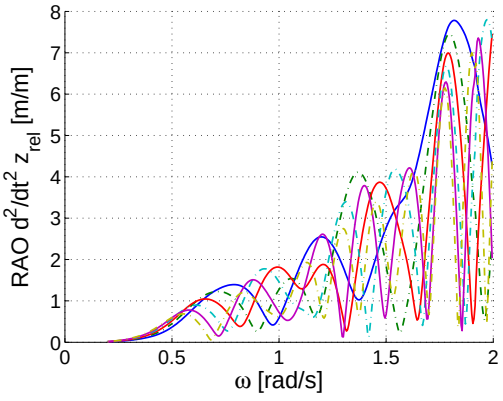

(C) Heading 90°

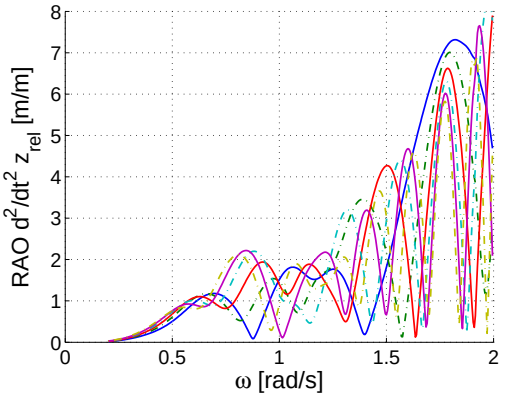

(D) Heading 135°

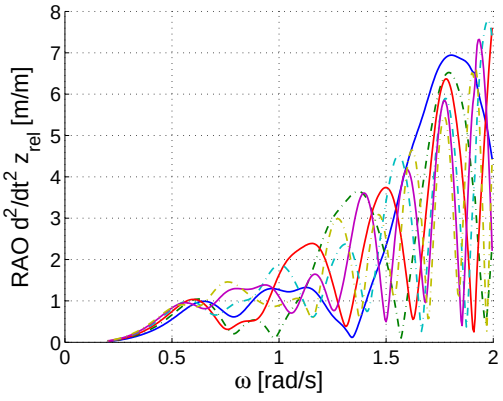

(E) Heading 180°

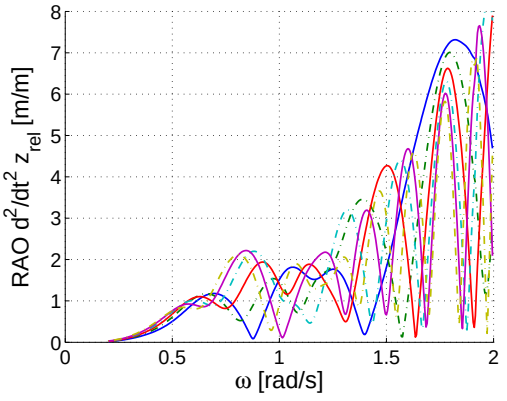

(F) Heading 225°

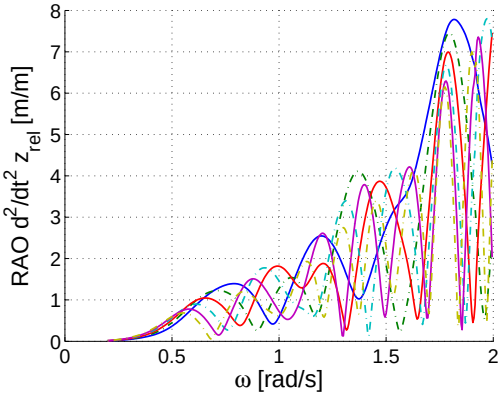

(G) Heading 270°

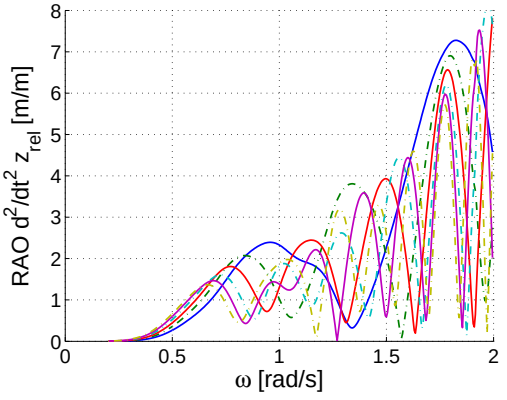

(H) Heading 315°

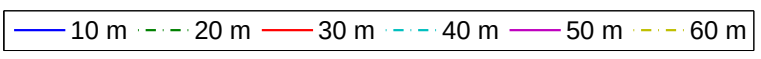

FIGURE B.10: RAO's of $^{d^2}/_{dt^2}z_{rel}$ for a disturbed approach

Appendix C

Current engineering methodology

This appendix described the current engineering method with which the loads related with slamming are estimated. The current method is based on a spectral analysis, from which the results are used in five defined load cases.

Motion Analysis

The current engineering approach uses RAO's of the relative motion, as is described in section 3.1. The loads are then determined according to five pre-defined load cases that are described below. For the current engineering method a spectral estimation with regard to the velocities and accelerations is used. This is further explained in chapter 4. To be consistent, the undisturbed MPM values as determined with potential theory in 4 are used here.

Heading	[°]	**0**	**45**	**90**	**135**	**180**	**225**	**270**	**315**
		poi_{inner}							
$\frac{d}{dt}\hat{z}_{rel,entry}$	$[\mathrm{m\,s^{-1}}]$	6.96	5.89	0	6.63	6.29	6.63	0	5.89
$\frac{d^2}{dt^2}\hat{z}_{rel,entry}$	$[\mathrm{m\,s^{-2}}]$	6.42	5.89	0	6.24	5.64	6.24	0	5.89
$\frac{d^2}{dt^2}\hat{z}_{poi,entry}$	$[\mathrm{m\,s^{-2}}]$	3.02	3.50	0	3.51	2.54	3.51	0	3.50
		poi_{middle}							
$\frac{d}{dt}\hat{z}_{rel,entry}$	$[\mathrm{m\,s^{-1}}]$	7.48	6.54	0	7.12	6.77	7.12	0	6.54
$\frac{d^2}{dt^2}\hat{z}_{rel,entry}$	$[\mathrm{m\,s^{-2}}]$	6.64	6.36	0	6.55	5.93	6.55	0	6.36
$\frac{d^2}{dt^2}\hat{z}_{poi,entry}$	$[\mathrm{m\,s^{-2}}]$	3.21	3.75	0	3.73	2.72	3.73	0	3.75
		poi_{outer}							
$\frac{d}{dt}\hat{z}_{rel,entry}$	$[\mathrm{m\,s^{-1}}]$	8.25	7.57	0	7.93	7.52	7.93	0	7.57
$\frac{d^2}{dt^2}\hat{z}_{rel,entry}$	$[\mathrm{m\,s^{-2}}]$	7.00	7.00	0	7.02	6.36	7.02	0	7.00
$\frac{d^2}{dt^2}\hat{z}_{poi,entry}$	$[\mathrm{m\,s^{-2}}]$	3.55	4.18	0	4.12	3.03	4.12	0	4.18

TABLE C.1: MPM values for a 3 hour storm from a spectral analysis with an undisturbed approach for different POI's

Load cases

The characteristic values as determined in the previous section are used to assess the loads related to the topic of this study by means of five load cases. These load cases are illustrated in figures C.1 to C.5.

$$F_d = \frac{1}{2}\rho_w C_D D v_{rel}^2 L drag \tag{C.1}$$

$$F_s = \frac{1}{2}\rho_w C_s D v_{rel}^2 L_{slam} \tag{C.2}$$

$$F_{entrapped} = \rho_w \pi r_o^2 \left(\ddot{z}_{rel,entry} + g\right) L_{entrapped} \tag{C.3}$$

In which:
$C_d = 1$
$C_s = 5.15$
[DNV, 2014]

C.0.3 Load case 1

The first load case is based on slam loading. For this situation it is assumed that one third of the overhang length is loaded simultaneously. The force is calculated with equation C.2 with a constant C_s of 5.15. The maximum relative velocity, as described in section C, is taken halfway the outer one third of the overhang length as is shown by the dotted green line in figure C.1.

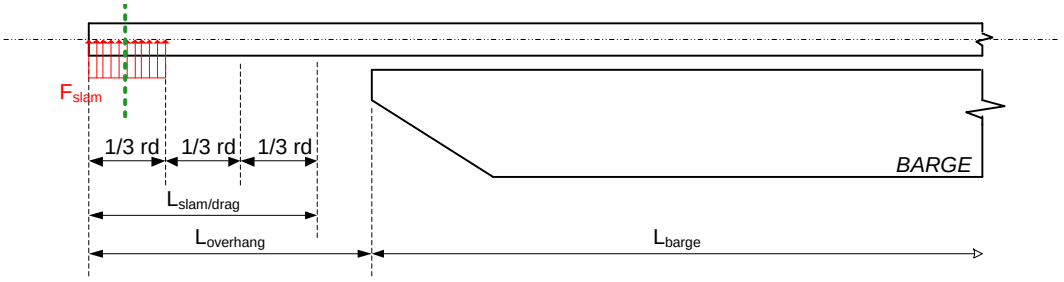

FIGURE C.1: Load case 1

C.0.4 Load case 2

Load case two is based on the structure being partly loaded by slam forces and partly by drag forces. The slam force is calculated with equation C.2 and the drag force with equation C.1. For both the slam load and drag load the maximum relative velocity as described in section C is taken halfway the inner one third of the overhang length, as is shown by the dotted green line in figure C.2.

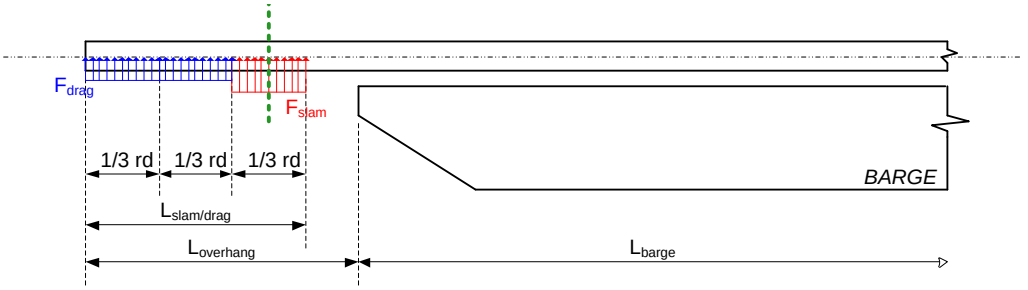

FIGURE C.2: Load case 2

C.0.5 Load case 3

The third load case is based on the entire structure overhang being loaded by drag forces, in a relative upward moving direction. The situation is sketched in figure C.3. The maximum relative velocity as described in section C is taken halfway the structure's overhang. The force is then calculated with equation C.1.

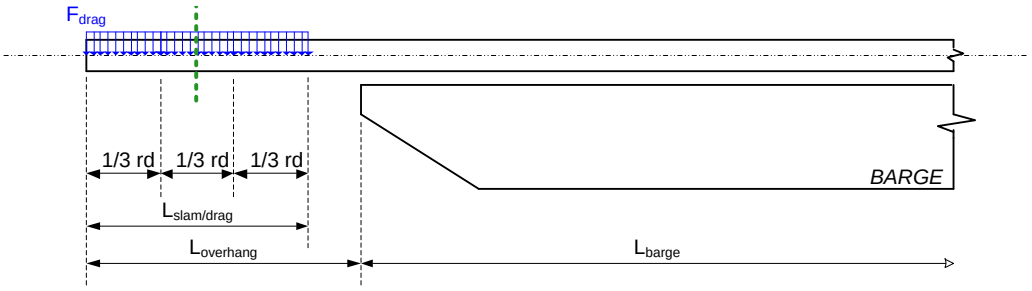

FIGURE C.3: Load case 3

C.0.6 Load case 4

Load case four is based on the situation in which one third of the structure's overhang length is filled with water, referred to as scooping. The load then originates from inertia, and is calculated with equation C.3. The maximum acceleration is taken halfway the outer one third of the overhang length and is added to the gravitational acceleration.

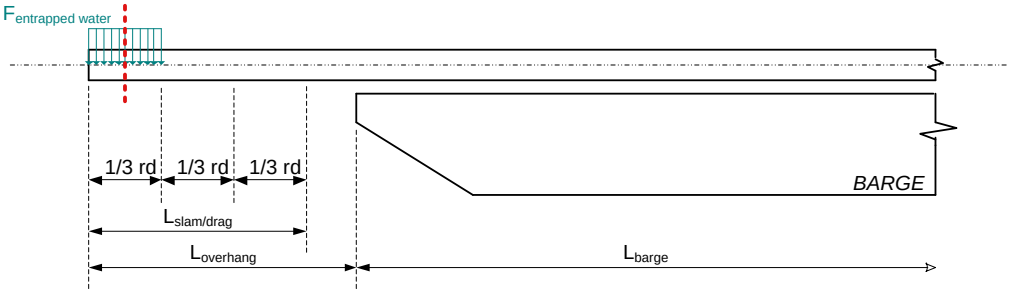

FIGURE C.4: Load case 4

C.0.7 Load case 5

The fifth load case is a combination of load case three and entrapped water in the outer one third of the overhang. Because this situation is only possible when the overhang is submerged, in this case the entrapped water is only accelerated with the acceleration of the POI, without taking gravity into account.

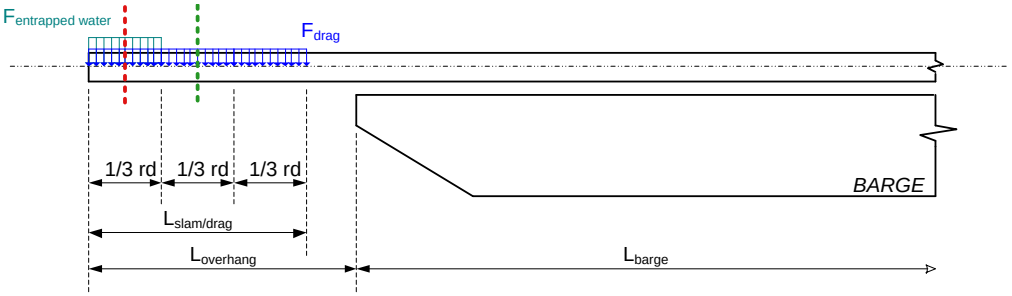

FIGURE C.5: Load case 5

Appendix D

Flowcharts

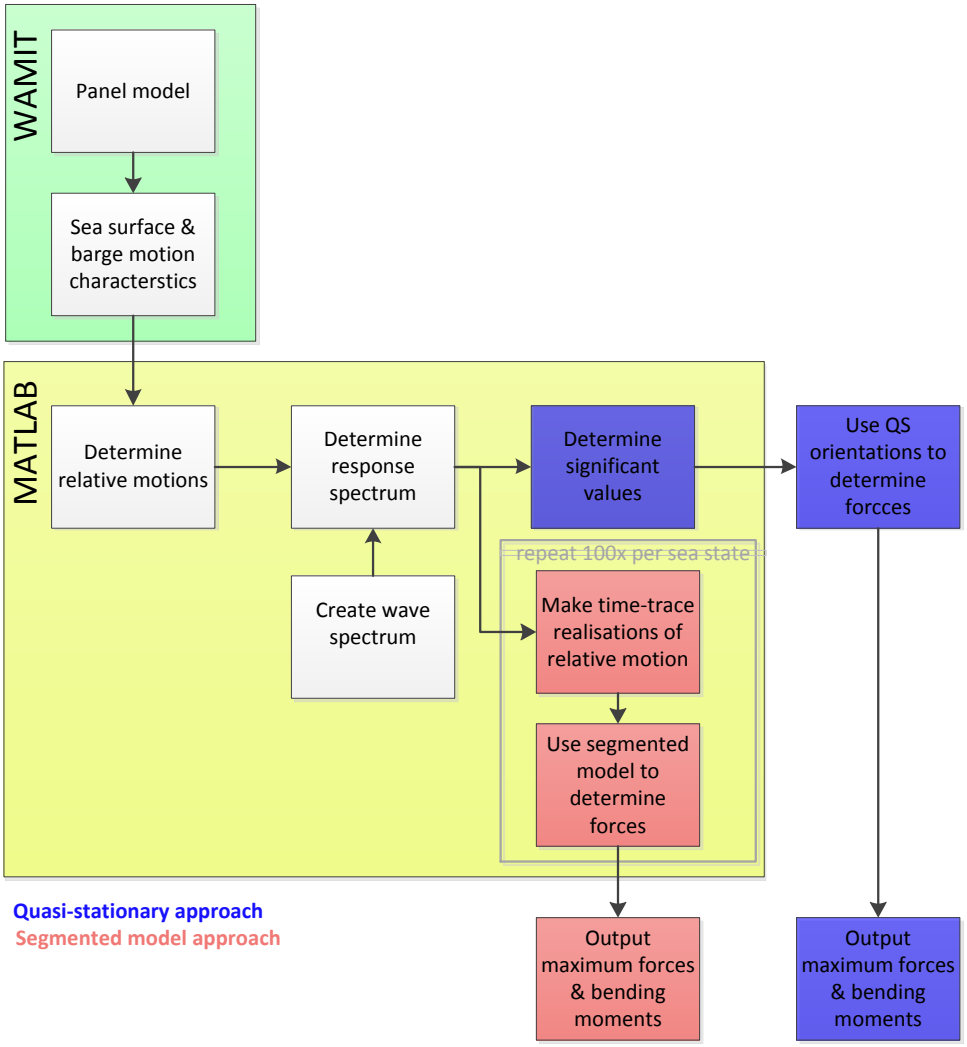

FIGURE D.1: Flowchart of approaches

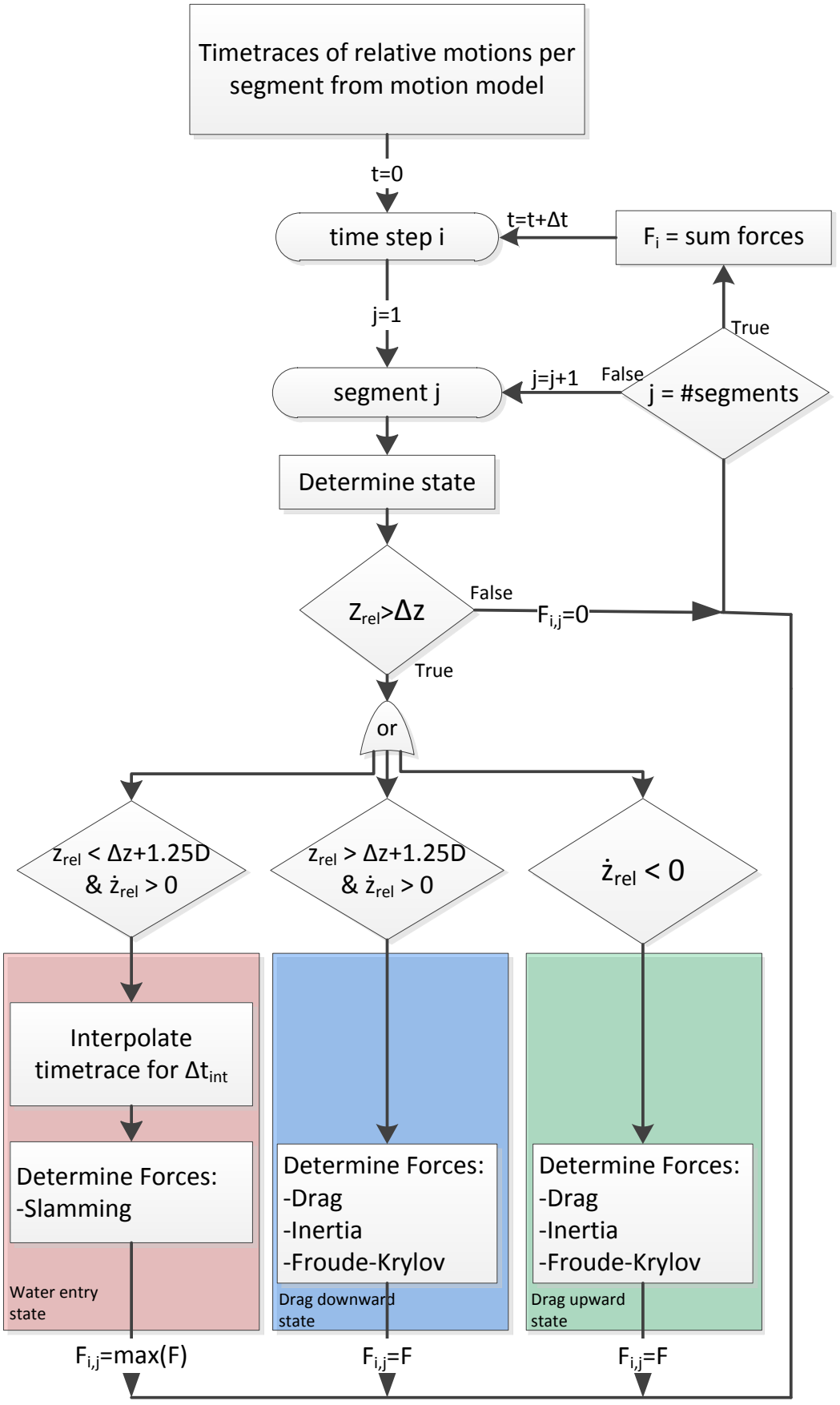

FIGURE D.2: Flowchart of segmented model

Appendix E

Source code of developed models

This appendix holds the source code for all the processes in the yellow shaded area in figure D.1.

Main file

```
close all; clear all; clc
%% SETTING PARAMETERS

wamit4file = './b400.4';
wamit6pfile = './b400.6p';
heading = 180;              % wave heading [deg]
nrpoints=22;                % nr of pois considered [-]
nrfrequencies=360;          % nr of frequencies considered [-]
nrheadings = 8;             % nr of headings considered [-]
g=9.81;                     % gravitational acceleration [m/s^2]

nriterations = 100;         % nr of iterations per heading [-]

Tp = 0;                     % Tp [s] , 0 for automatic
dz = 5.425;                 % initial gap [m]
dx = 1;                     % segment length [m]
gamma = 3.3;                  % peak shape factor spectrum [-]
Hs = 6.3;                   % significant wave height [m]
dt = 0.1;                   % time step [s]
tstorm =10800;              % realisation time [s]
diameter = 2.13;            % pipe outer diameter [m]
innerdiameter = 2.04;       % pipe inner diameter [m]

diffraction = 1;            % take dif into account (1 for yes, 0 for no)
radiation = 1;              % take dif into account (1 for yes, 0 for no)
showplots = 0;              % show plots

%% IMPORT DATA
xb=-61-dx:-dx:-61-(dx*nrpoints); % x-coordinate of poi's [m]
t=0:dt:tstorm-dt; %duration of time trace with interval dt

%import disturbed sea surface information via function
disturbdata = seasurface_import_data(heading, nrpoints, nrfrequencies, nrheadings,
    wamit6pfile);
```

```
34
35 %import wamit motion rao's
36     f = load(wamit4file);
37     data(:,:) = f;
38     data(:,4) = f(:,4);
39
40
41 %% CALCULATE RAO's for every segment
42
43 %Pre-allocate variables
44 rad_re_heave = zeros(nrfrequencies,nrpoints);
45 rad_im_heave = zeros(nrfrequencies,nrpoints);
46 rad_amp_heave = zeros(nrfrequencies,nrpoints);
47 rad_phase_heave = zeros(nrfrequencies,nrpoints);
48
49 rad_re_pitch = zeros(nrfrequencies,nrpoints);
50 rad_im_pitch = zeros(nrfrequencies,nrpoints);
51 rad_amp_pitch = zeros(nrfrequencies,nrpoints);
52 rad_phase_pitch = zeros(nrfrequencies,nrpoints);
53
54 dif_re = zeros(nrfrequencies,nrpoints);
55 dif_im = zeros(nrfrequencies,nrpoints);
56 dif_amp = zeros(nrfrequencies,nrpoints);
57 dif_phase = zeros(nrfrequencies,nrpoints);
58
59 reldisre=zeros(nrfrequencies,nrpoints);
60 reldisim=zeros(nrfrequencies,nrpoints);
61 ampdis = zeros(nrfrequencies,nrpoints);
62 phasedis = zeros(nrfrequencies,nrpoints);
63
64 absre=zeros(nrfrequencies,nrpoints);
65 absim=zeros(nrfrequencies,nrpoints);
66 amp_abspoi = zeros(nrfrequencies,nrpoints);
67 phase_abspoi = zeros(nrfrequencies,nrpoints);
68
69 wavedisre=zeros(nrfrequencies,nrpoints);
70 wavedisim=zeros(nrfrequencies,nrpoints);
71 wavedisamp = zeros(nrfrequencies,nrpoints);
72 wavedisphase = zeros(nrfrequencies,nrpoints);
73
74 relundre = zeros(nrfrequencies,nrpoints);
75 relundim = zeros(nrfrequencies,nrpoints);
76 relundamp = zeros(nrfrequencies,nrpoints);
77 relundphase = zeros(nrfrequencies,nrpoints);
78
79     for point=1:1:nrpoints
80
81         pitchind = find(data(:,2,1) == heading & data(:,3,1) == 5);
82
83         pitch_re = data(pitchind,6);
84         pitch_im = data(pitchind,7);
85         pitch_amp = sqrt(pitch_re.^2 + pitch_im.^2);
86         pitch_phase = atan2(pitch_im, pitch_re);
87
```

```
88          heaveind = find(data(:,2,1) == heading & data(:,3,1) == 3);
89
90          heave_re = data(heaveind,6);
91          heave_im = data(heaveind,7);
92          heave_amp = sqrt(heave_re.^2 + heave_im.^2);
93          heave_phase = atan2(heave_im, heave_re);
94
95          wavelength=(g/(2*pi))*(2*pi./data(heaveind,1)).^2;
96          wavenumber = (2*pi)./wavelength;
97
98          absre(:,point) = -xb(point)*pitch_amp.*cos(pitch_phase) + heave_amp.*cos(
    heave_phase);
99          absim(:,point) = -xb(point)*pitch_amp.*sin(pitch_phase) + heave_amp.*sin(
    heave_phase);
100         amp_abspoi(:,point) = sqrt(absre(:,point).^2+absim(:,point).^2);
101         phase_abspoi(:,point) = atan2(absim(:,point), absre(:,point));
102
103        if(diffraction == 1 && radiation ==1)
104
105         %heave radiation
106         rad_re_heave(:,point) = disturbdata.radre(:,3,point);
107         rad_im_heave(:,point) = disturbdata.radim(:,3,point);
108         rad_amp_heave(:,point) = sqrt( rad_re_heave(:,point).^2 + rad_im_heave(:,point
    ).^2);
109         rad_phase_heave(:,point) = atan2(rad_im_heave(:,point), rad_re_heave(:,point))
    ;
110
111         %pitch radiation
112         rad_re_pitch(:,point) = disturbdata.radre(:,5,point);
113         rad_im_pitch(:,point) = disturbdata.radim(:,5,point);
114         rad_amp_pitch(:,point) = sqrt( rad_re_pitch(:,point).^2 + rad_im_pitch(:,point
    ).^2);
115         rad_phase_pitch(:,point) = atan2(rad_im_pitch(:,point), rad_re_pitch(:,point))
    ;
116
117         %diffraction
118         dif_re(:,point) = disturbdata.difre(:,point);
119         dif_im(:,point) = disturbdata.difim(:,point);
120         dif_amp(:,point) = sqrt( dif_re(:,point).^2 + dif_im(:,point).^2 );
121         dif_phase(:,point) = atan2(dif_im(:,point), dif_re(:,point));
122
123         reldisre(:,point) = (dif_amp(:,point).*cos(dif_phase(:,point)) + (
    rad_amp_heave(:,point) .* heave_amp ) .* cos (rad_phase_heave(:,point) +
    heave_phase) + (rad_amp_pitch(:,point) .* pitch_amp ) .* cos(rad_phase_pitch(:,
    point) + pitch_phase) ) - ( -xb(point)*pitch_amp .* cos(pitch_phase) + heave_amp .*
     cos(heave_phase) );
124         reldisim(:,point) = (dif_amp(:,point).*sin(dif_phase(:,point)) + (
    rad_amp_heave(:,point) .* heave_amp ) .* sin (rad_phase_heave(:,point) +
    heave_phase) + (rad_amp_pitch(:,point) .* pitch_amp ) .* sin(rad_phase_pitch(:,
    point) + pitch_phase) ) - ( -xb(point)*pitch_amp .* sin(pitch_phase) + heave_amp .*
     sin(heave_phase) );
125
```

```
126         wavedisre(:,point) = (dif_amp(:,point).*cos(dif_phase(:,point)) + (
    rad_amp_heave(:,point) .* heave_amp ) .* cos (rad_phase_heave(:,point) +
    heave_phase) + (rad_amp_pitch(:,point) .* pitch_amp ) .* cos(rad_phase_pitch(:,
    point) + pitch_phase) );
127         wavedisim(:,point) = (dif_amp(:,point).*sin(dif_phase(:,point)) + (
    rad_amp_heave(:,point) .* heave_amp ) .* sin (rad_phase_heave(:,point) +
    heave_phase) + (rad_amp_pitch(:,point) .* pitch_amp ) .* sin(rad_phase_pitch(:,
    point) + pitch_phase) );
128
129         ampdis(:,point) = sqrt(reldisre(:,point).^2 + reldisim(:,point).^2);
130         phasedis(:,point) = atan2(reldisim(:,point), reldisre(:,point));
131
132         wavedisamp(:,point) = sqrt(wavedisre(:,point).^2 + wavedisim(:,point).^2);
133         wavedisphase(:,point) = atan2(wavedisim(:,point), wavedisre(:,point));
134
135         elseif(diffraction ==1 && radiation ==0)
136
137         %diffraction
138         dif_re(:,point) = disturbdata.difre(:,point);
139         dif_im(:,point) = disturbdata.difim(:,point);
140         dif_amp(:,point) = sqrt( dif_re(:,point).^2 + dif_im(:,point).^2 );
141         dif_phase(:,point) = atan2(dif_im(:,point), dif_re(:,point));
142
143         reldisre(:,point) = (dif_amp(:,point).*cos(dif_phase(:,point))) - ( -xb(point)
    *pitch_amp .* cos(pitch_phase) + heave_amp .* cos(heave_phase) );
144         reldisim(:,point) = (dif_amp(:,point).*sin(dif_phase(:,point))) - ( -xb(point)
    *pitch_amp .* sin(pitch_phase) + heave_amp .* sin(heave_phase) );
145
146         wavedisre(:,point) = (dif_amp(:,point).*cos(dif_phase(:,point))  );
147         wavedisim(:,point) = (dif_amp(:,point).*sin(dif_phase(:,point))  );
148
149
150         ampdis(:,point) = sqrt(reldisre(:,point).^2 + reldisim(:,point).^2);
151         phasedis(:,point) = atan2(reldisim(:,point), reldisre(:,point));
152
153
154         wavedisamp(:,point) = sqrt(wavedisre(:,point).^2 + wavedisim(:,point).^2);
155         wavedisphase(:,point) = atan2(wavedisim(:,point), wavedisre(:,point));
156
157
158        elseif(diffraction ==0 && radiation ==1)
159         %heave radiation
160         rad_re_heave(:,point) = disturbdata.radre(:,3,point);
161         rad_im_heave(:,point) = disturbdata.radim(:,3,point);
162         rad_amp_heave(:,point) = sqrt( rad_re_heave(:,point).^2 + rad_im_heave(:,point
    ).^2);
163         rad_phase_heave(:,point) = atan2(rad_im_heave(:,point), rad_re_heave(:,point))
    ;
164
165         %pitch radiation
166         rad_re_pitch(:,point) = disturbdata.radre(:,5,point);
167         rad_im_pitch(:,point) = disturbdata.radim(:,5,point);
168         rad_amp_pitch(:,point) = sqrt( rad_re_pitch(:,point).^2 + rad_im_pitch(:,point
    ).^2);
```

```
169         rad_phase_pitch(:,point) = atan2(rad_im_pitch(:,point), rad_re_pitch(:,point))
    ;
170
171
172         reldisre(:,point) = (cos(xb(point)*cosd(heading)*wavenumber) + ( rad_amp_heave
    (:,point) .* heave_amp ) .* cos (rad_phase_heave(:,point) + heave_phase) + (
    rad_amp_pitch(:,point) .* pitch_amp ) .* cos(rad_phase_pitch(:,point) + pitch_phase
    ) ) - ( -xb(point)*pitch_amp .* cos(pitch_phase) + heave_amp .* cos(heave_phase) );
173         reldisim(:,point) = (sin(xb(point)*cosd(heading)*wavenumber) + ( rad_amp_heave
    (:,point) .* heave_amp ) .* sin (rad_phase_heave(:,point) + heave_phase) + (
    rad_amp_pitch(:,point) .* pitch_amp ) .* sin(rad_phase_pitch(:,point) + pitch_phase
    ) ) - ( -xb(point)*pitch_amp .* sin(pitch_phase) + heave_amp .* sin(heave_phase) );
174
175         wavedisre(:,point) = (( rad_amp_heave(:,point) .* heave_amp ) .* cos (
    rad_phase_heave(:,point) + heave_phase) + (rad_amp_pitch(:,point) .* pitch_amp ) .*
     cos(rad_phase_pitch(:,point) + pitch_phase) );
176         wavedisim(:,point) = (( rad_amp_heave(:,point) .* heave_amp ) .* sin (
    rad_phase_heave(:,point) + heave_phase) + (rad_amp_pitch(:,point) .* pitch_amp ) .*
     sin(rad_phase_pitch(:,point) + pitch_phase) );
177
178
179         ampdis(:,point) = sqrt(reldisre(:,point).^2 + reldisim(:,point).^2);
180         phasedis(:,point) = atan2(reldisim(:,point), reldisre(:,point));
181
182         wavedisamp(:,point) = sqrt(wavedisre(:,point).^2 + wavedisim(:,point).^2);
183         wavedisphase(:,point) = atan2(wavedisim(:,point), wavedisre(:,point));
184
185       elseif(diffraction == 0 && radiation ==0)
186
187         reldisre(:,point) = cos(-xb(point).*wavenumber.*cosd(heading)) - (-xb(point)*
    pitch_amp .* cos(pitch_phase) + heave_amp .* cos(heave_phase));
188         reldisim(:,point) = sin(-xb(point).*wavenumber.*cosd(heading)) - (-xb(point)*
    pitch_amp .* sin(pitch_phase) + heave_amp .* sin(heave_phase));
189         %dist = -xb(point)*cosd(heading);
190         %eps = wavelength./dist;
191         eps = -xb(point).*wavenumber*cosd(heading);
192         wavedisre(:,point) = cos(eps);
193         wavedisim(:,point) = sin(eps);
194
195         %reldisre(:,point) = wavedisre(:,point) - absre(:,point);
196         %reldisim(:,point) = wavedisim(:,point) - absim(:,point);
197
198
199         ampdis(:,point) = sqrt(reldisre(:,point).^2 + reldisim(:,point).^2);
200         phasedis(:,point) = atan2(reldisim(:,point), reldisre(:,point));
201
202         wavedisamp(:,point) = sqrt(wavedisre(:,point).^2 + wavedisim(:,point).^2);
203         wavedisphase(:,point) = atan2(wavedisim(:,point), wavedisre(:,point));
204
205       else
206             error('Error in disturbed sea surface settings')
207       end
208
209
```

```
210
211
212     end
213
214 %%
215 sq = 0.2:0.005:0.2+(nrfrequencies-1)*0.005;
216
217 lowerbound_tp = sqrt(13*Hs);
218 upperbound_tp = sqrt(30*Hs);
219
220 periods_tp = 2*pi./sq;
221
222 lowerbound_tp_ind = find(periods_tp <= lowerbound_tp);
223 upperbound_tp_ind = find(periods_tp >= upperbound_tp);
224 boundindices = [lowerbound_tp_ind upperbound_tp_ind];
225
226 if(Tp == 0)
227 ampdis_tp = ampdis;
228 ampdis_tp(boundindices,:) = 0;
229
230 [M,I] = max(ampdis_tp);
231
232 %ampvels = ampdis(:,22)./periods';
233 Tp = 2*pi/sq(I(1,nrpoints));
234 end
235
236 disp(['Tp = ', num2str(Tp)]);
237
238
239 %%Loop for HS'en
240  P95 = zeros(105,10);
241 MPM = zeros(105,5);
242  counter=0;
243 %for Hs=3:0.1:10;
244  disp(['Hs = ', num2str(Hs)])
245  counter=counter+1;
246 %% SEGMENTED MODEL
247
248 %make JONSWAP variance spectrum
249 Sw = wavespectrum(Hs,Tp,gamma,sq);
250
251 integral_m0 = Sw*0.005;
252 m0 = sum(integral_m0);
253 integral_m2 = sq.^2.*Sw*0.005;
254 m2 = sum(integral_m2);
255 tz = 2*pi*sqrt(m0./m2);
256
257 %Determine response spectrum
258 Sw_zrel = bsxfun(@times, Sw', ampdis.^2);
259 Sw_zpoi = bsxfun(@times, Sw', amp_abspoi.^2);
260 Sw_pitch = bsxfun(@times, Sw', pitch_amp.^2);
261 Sw_zwave = bsxfun(@times, Sw', wavedisamp.^2);
262
263 %%     START FORCE SCRIPT
```

```
264
265 for i=1:1:nriterations
266 clear iteration_result DFT Zrel
267 disp(['Simulation: ',num2str(i)])
268 tic
269
270 N = tstorm/dt;
271 dw = 2*pi / (dt * N);
272 om = 0:dw:(N-1)*dw;
273
274 wave_phase_shifts = 2*pi*rand(size(om));
275
276 Zrel=zeros(length(t),nrpoints);
277 Zpoi=zeros(length(t),nrpoints);
278 Zeta=zeros(length(t),nrpoints);
279
280 for j=1:1:nrpoints
281
282 Spec = hmcSpectrum;
283 Spec.addSpectrum(Sw_zrel(:,j)',0,sq);
284 Zrel(:,j) = Spec.makeTimetrace(N,dt, wave_phase_shifts, phasedis(:,j)')';
285
286 Specpoi = hmcSpectrum;
287 Specpoi.addSpectrum(Sw_zpoi(:,j)',0,sq);
288 Zpoi(:,j) = Specpoi.makeTimetrace(N,dt, wave_phase_shifts, phase_abspoi(:,j)')';
289
290 Specwave = hmcSpectrum;
291 Specwave.addSpectrum(Sw_zwave(:,j)',0,sq);
292 Zeta(:,j) = Specwave.makeTimetrace(N,dt, wave_phase_shifts, wavedisphase(:,j)')';
293 end
294
295 Specpitch = hmcSpectrum;
296 Specpitch.addSpectrum(Sw_pitch',0,sq);
297 pitch = Specpitch.makeTimetrace(N,dt, wave_phase_shifts, pitch_phase')';
298
299 %calculate forces from timetrace
300 iteration_result = timetrace_to_forces(Zrel,Zpoi,Zeta,pitch,tz,dt,dx,dz,diameter,
      innerdiameter,include_selfweight);
301
302
303
304 %% Determine iteration maxima
305 Forces_total=zeros(size(iteration_result.Forces_slam,1),4);
306   %Forces_total=zeros(size(Zrel,1)-2,4);
307    Forces_total(:,1)=sum(iteration_result.Forces_slam,2);
308    Forces_total(:,2)=sum(iteration_result.Forces_drag,2);
309    Forces_total(:,3)=sum(iteration_result.Forces_inertia,2);
310   %Forces_total(:,4)=sum(iteration_result.Forces_froudekrylov,2);
311    Forces_total(:,5)=sum(iteration_result.Forces_static_steel,2);
312    Forces_total(:,6)=sum(iteration_result.Forces_inertia_steel,2);
313    Forces_total(:,7)=sum(Forces_total(:,1:3),2);
314    Forces_total(:,8)=sum(iteration_result.Forces_total,2);
315
316    maxima.Forces(i) = max(Forces_total(:,7));
```

```
317    minima.Forces(i) = min(Forces_total(:,7));
318    maxima.Bendmoment(i) = max(iteration_result.Ms);
319    minima.Bendmoment(i) = min(iteration_result.Ms);
320    maxima.Pitchmoment(i) = max(iteration_result.Mp);
321    minima.Pitchmoment(i) = min(iteration_result.Mp);
322
323
324    maxima.submergence(i) = iteration_result.submergence;
325    maxima.slamvel(i) = max((iteration_result.slamvel));
326    maxima.nrslams(i) = iteration_result.nrslams;
327
328    maxima.subacc(i) = max(abs(iteration_result.acc(:,22)));
329    maxima.subvel(i) = max(abs(iteration_result.vel(:,22)));
330
331
332 toc
333 end %end iteration loop
334
335 %% Extreme value analysis
336
337 disp(['Tp = ' num2str(Tp)]);
338
339  sortedmaxforces = sort(maxima.Forces);
340  sortedminforces = sort(abs(minima.Forces));
341  sortedmaxbendmoment = sort(maxima.Bendmoment);
342  sortedminbendmoment = sort(abs(minima.Bendmoment));
343  sortedmaxpitchmoment = sort(maxima.Pitchmoment);
344  sortedminpitchmoment = sort(abs(maxima.Pitchmoment));
345  sortedslamvel = sort(maxima.slamvel);
346  sortednrslams = sort(maxima.nrslams);
347  sortedsubmergence = sort(maxima.submergence);
348  sortedsubaccs = sort(maxima.subacc);
349  sortedsubvels = sort(maxima.subvel);
350
351
352
353    P95(counter,1) = Hs;
354    P95(counter,2) = sortedmaxforces(95);
355    P95(counter,3) = sortedminforces(95);
356    P95(counter,4) = sortedmaxbendmoment(99);
357    P95(counter,5) = sortedminbendmoment(95);
358    P95(counter,6) = sortedmaxpitchmoment(95);
359    P95(counter,7) = sortedminpitchmoment(95);
360    P95(counter,8) = sortedslamvel(95);
361    P95(counter,9) = sortednrslams(95);
362    P95(counter,10) = sortedsubmergence(95);
```

Function to import seasurface and vessel characteristics from WAMIT

```
1 function [ seasurface ] = seasurface_import_data( heading, nrpoints, nrfrequencies,
      nrheadings, wamit6pfile )
2 % Function to import diffraction and radiation terms at fieldpoints from
3 % wamit .6p file.
4 % RGM Wijnands, 02-03-2015
```

```
5
6  f = importdata(wamit6pfile);
7
8  %pre-allocate variables
9  difre=zeros(nrfrequencies,nrpoints);
10 difim=zeros(nrfrequencies,nrpoints);
11 radretot=zeros(nrfrequencies,6,nrpoints);
12 radimtot=zeros(nrfrequencies,6,nrpoints);
13
14 %determine starting rows for diffraction and radiation terms seperately
15 difstartfirst = nrpoints + 1 + (heading / (360/nrheadings)) * nrpoints ;
16 difstartpoints = difstartfirst:1:difstartfirst + nrpoints - 1;
17 radstartpoints = 1:1:nrpoints;
18
19 for point = 1:1:nrpoints
20    %determine diffraction and radiation row of point
21    interval = nrpoints*(nrheadings+1);
22    difrows = difstartpoints(1,point):interval:size(f,1);
23    radrows = radstartpoints(1,point):interval:size(f,1);
24
25    %Put radiation terms in matrix, output is normalised w.r.t. incident
26    %wave amplitude
27    difre(:,point) = f(difrows,4);
28    difim(:,point) = f(difrows,5);
29
30    %pre-allocate variables
31    radre_int = zeros(nrfrequencies,6);
32    radim_int = zeros(nrfrequencies,6);
33
34    for mode =1:1:6
35        %radiation contributions per mode
36        radre_int(:,mode) = f(radrows,2*mode+1);
37        radim_int(:,mode) = f(radrows,2*mode+2);
38
39    end
40
41    %Put radiation terms in 3D matrix, output is normalised w.r.t. amplitude
42    %of corresponding mode
43    radretot(:,:,point) = radre_int;
44    radimtot(:,:,point) = radim_int;
45
46 end
47     %return results
48     seasurface.difre = difre;
49     seasurface.difim = difim;
50     seasurface.radre = radretot;
51     seasurface.radim = radimtot;
52
53 end
```

Function to transfrom the derived time trace to forces (segmented model)

```
1  function [ results ] = timetrace_to_forces( Zrel, Zpoi, Zeta, pitch_r, tz, dt, dx, dz,
       diameter, innerdiameter, include_selfweight)
```

```
2         %Function to calculate forces on a cylinder moving through water, given
3         %a timetrace of relative motions
4     %Author: RGM Wijnands
5     %Date: 09-01-2015
6
7     %calculate velocities and accelerations by differentiation
8     vel_rel=diff(Zrel)/dt;
9     acc_rel=diff(vel_rel)/dt;
10
11    vel_poi = diff(Zpoi)/dt;
12    acc_poi = diff(vel_poi)/dt;
13
14    vel_eta = diff(Zeta)/dt;
15    acc_eta = diff(vel_eta)/dt;
16
17    %delete two last and last row due to differentiation
18    Zrel(end-1:end,:)=[];
19    vel_rel(end,:)=[];
20
21    Zpoi(end-1:end,:)=[];
22    vel_poi(end,:)=[];
23
24    Zeta(end-1:end,:)=[];
25    vel_eta(end,:)=[];
26
27    pitch_r(end-1:end)=[];
28    pitch = bsxfun(@times, -pitch_r, ones(size(acc_rel,1),size(acc_rel,2)));
29
30    %define constant parameters
31    rho_w = 1025;                          % density of water [kg/m^3]
32    rho_s = 7850;                          % density of water [kg/m^3]
33    C_d = 1;                               % cylinder drag coefficient
34    C_m = 1;                               % cylinder added mass coefficient
35    nu = 1.004e-6;                         % kinematic viscosity water
36    g=9.81;                                % gravitational acceleration [m/s^2]
37
38    %Determine area's
39    Ai = 0.25 * pi * innerdiameter^2;
40    Ao = 0.25 * pi * diameter^2;
41    As = 0.25 * pi * (diameter^2 - innerdiameter^2);
42
43    %Advanced cylinder slamming coefficient
44    vtd = 0:0.05:1.25;
45    cstheta = [5.15 3.55 2.90 2.50 2.20 1.95 1.80 1.70 1.60 1.50 1.42 1.37 1.31 1.27
      1.23 1.205 1.185 1.150 1.130 1.110 1.090 1.070 1.050 1.030 1.010 1];
46
47    %find submerged time steps, rel. position is larger than SWL gap
48    ind_submerged_end = find(Zrel(:,size(Zrel,2))>dz);
49    acc_submerged = zeros(size(Zrel,1),size(Zrel,2));
50    vel_submerged = zeros(size(Zrel,1),size(Zrel,2));
51    vel_submerged(ind_submerged_end,size(Zrel,2)) = vel_rel(ind_submerged_end,size(
      Zrel,2));
52    acc_submerged(ind_submerged_end,size(Zrel,2)) = acc_rel(ind_submerged_end,size(
      Zrel,2));
```

```
53
54
55      %To count number of slamming occurences, check number of submergences
56      %of most outward point. Also save rel. velocities at these time steps
57      iSlam = find((Zrel(1:end-1,size(Zrel,2)) < dz) & (Zrel(2:end,size(Zrel,2)) > dz));
58      nrslams = length(iSlam);
59      slamvelindex = vel_rel(iSlam,size(Zrel,2));
60
61      if(isempty(slamvelindex))
62          slamvelindex = 0;
63      end
64
65      %calculate the submergence and dimensionless submergence for every
66      %segment per time step
67      submergence = Zrel-dz;
68      submergence(submergence<0) = 0;
69      submergence_dimless = submergence./(diameter);
70      submergence_max = max(submergence(1:end,size(Zrel,2)));
71
72      submergence_centreline = submergence - 0.5*diameter;
73      submergence_centreline(submergence_centreline<0) = 0;
74
75
76      %Find the timesteps in which the segments are in the drag state or
77      %slamming state, based on the dimensionless submergence and direction
78      %of the rel. motion
79      ind_drag = find((submergence >= (1.25*diameter)) | (submergence > 0 & vel_rel <0))
        ;
80      ind_slam = find((submergence > 0) & (submergence < (1.25*diameter)) & (vel_rel >
        0) );
81      ind_slam_delta = ind_slam(2:end) - ind_slam(1:end-1);
82      ind_slam_endstraight = find(ind_slam_delta > 1);
83
84      %Find the relative velocities corresponding to the drag and slam state
85      %time steps
86      dragvel_rel_temp = scalefactor.*vel_eta - vel_poi;
87      dragvel = zeros(size(Zrel,1),size(Zrel,2));
88      dragvel(ind_drag) = dragvel_rel_temp(ind_drag);
89
90      acc_rel_temp = scalefactor.*acc_eta - acc_poi;
91      acc_rel_scaled = zeros(size(Zrel,1),size(Zrel,2));
92      acc_rel_scaled(ind_drag) = acc_rel_temp(ind_drag);
93
94      acc_eta_temp = scalefactor.*acc_eta;
95      acc_eta_scaled = zeros(size(Zrel,1),size(Zrel,2));
96      acc_eta_scaled(ind_drag) = acc_eta_temp(ind_drag);
97
98      slamvel = zeros(size(Zrel,1),size(Zrel,2));
99      slamvel(ind_slam) = vel_rel(ind_slam);
100
101     %Determine characteristic parameters
102     Fr = abs(slamvel) / sqrt(g * diameter/2);
103     Re = abs(dragvel) * 0.5 * diameter / nu;
104     KC = abs(dragvel) * 12.1 / (0.5 * diameter);
```

```
105
106
107     Forces_entrapped_mass = zeros(size(Zrel,1),size(Zrel,2));
108     %Determine acting drag and inertia forces
109     Forces_drag = 0.5 * rho_w * C_d * diameter * dx .* dragvel.*abs(dragvel);
110     Forces_added_mass = Ao * rho_w * C_m * dx * acc_rel_scaled ;
111     Forces_entrapped_mass_temp = Ai * rho_w * dx * -1 * acc_poi ;
112     Forces_entrapped_mass(ind_drag) = Forces_entrapped_mass_temp(ind_drag);
113     Forces_froudekrylov = Ao * rho_w * dx * acc_eta_scaled ;
114     Forces_inertia = zeros(size(submergence,1),size(submergence,2));
115     Forces_inertia(ind_drag) = Forces_added_mass(ind_drag) + Forces_entrapped_mass(
        ind_drag) + Forces_froudekrylov(ind_drag);
116
117     if(include_selfweight == 1)
118         Forces_static_steel = - As * dx * (rho_s - rho_w) * g * ones(size(Zrel,1),size
        (Zrel,2));
119         Forces_inertia_steel = As * dx * rho_s * acc_poi;
120     else
121         Forces_static_steel = zeros(size(Zrel,1),size(Zrel,2));
122         Forces_inertia_steel = zeros(size(Zrel,1),size(Zrel,2));
123     end
124
125     if(isempty(ind_slam) == 0 && ind_slam(1) == 1)
126         ind_slam(1)=[];
127     end
128
129
130     %for slamming timesteps, refine dx with factor 10 to assure enough
131     %resolution for a correct determinatio of Cs by linear interpolation
132     interval=0.1:0.1:0.9;
133
134     %samplevalues_dimsub = [submergence_dimless(ind_slam-1) submergence_dimless(
        ind_slam) submergence_dimless(ind_slam)-submergence_dimless(ind_slam-1) ];
135     samplevalues_dimsub = [Zrel(ind_slam-1) Zrel(ind_slam) Zrel(ind_slam)-Zrel(
        ind_slam-1) ];
136     samplevalues_velocities = [vel_rel(ind_slam-1) vel_rel(ind_slam) vel_rel(ind_slam)
        -vel_rel(ind_slam-1) ];
137     addvalues_dimsub =  samplevalues_dimsub(:,3)*interval;
138     addvalues_velocity = samplevalues_velocities(:,3)*interval;
139
140     %intervalvalues_dimsub = bsxfun(@plus,samplevalues_dimsub(:,1),addvalues_dimsub);
141     intervalvalues_dimsub_temp = bsxfun(@plus,samplevalues_dimsub(:,1),
        addvalues_dimsub)-dz;
142     intervalvalues_dimsub = intervalvalues_dimsub_temp / diameter;
143     intervalvalues_velocity = bsxfun(@plus,samplevalues_velocities(:,1),
        addvalues_velocity);
144
145     intervalvalues_Cs = interp1(vtd,cstheta,intervalvalues_dimsub);
146     interval_slamforces = 0.5*rho_w*diameter*dx.*intervalvalues_Cs.*
        intervalvalues_velocity.*abs(intervalvalues_velocity);
147     interval_slamforces_max = max(interval_slamforces,[],2);
148     interval_slamforces_last = interval_slamforces(:,9);
149
150     Forces_slam = zeros(size(Zrel,1),size(Zrel,2));
```

```
151     Forces_slam(ind_slam-1) = interval_slamforces_max;
152     Forces_slam(ind_slam(ind_slam_endstraight)) = interval_slamforces_last(
        ind_slam_endstraight);
153
154
155
156     %Calculate moments w.r.t. cylinder starting point and barge COG
157     supportmomentarm = linspace(dx/2,size(Zrel,2)-0.5,size(Zrel,2));
158     pitchmomentarm = supportmomentarm+61;
159
160     Forces_total = Forces_slam+Forces_drag+Forces_inertia;
161
162     Ms=sum(bsxfun(@times,Forces_total,supportmomentarm),2);
163     Mp=sum(bsxfun(@times,Forces_total,pitchmomentarm),2);
164
165     %Output results to object
166     results.Forces_slam = Forces_slam;
167     results.Forces_drag = Forces_drag;
168     results.Forces_inertia = Forces_inertia;
169     results.Forces_added_mass = Forces_added_mass;
170     results.Forces_entrapped_mass = Forces_entrapped_mass;
171     results.Forces_froudekrylov = Forces_froudekrylov;
172     results.Forces_static_steel =  Forces_static_steel;
173     results.Forces_inertia_steel =  Forces_inertia_steel;
174     results.Forces_total = Forces_total;
175     results.Ms = Ms;
176     results.Mp = Mp;
177     results.Fr = Fr;
178     results.Re = Re;
179     results.KC = KC;
180     results.slamvel = slamvelindex;
181     results.nrslams = nrslams;
182     results.submergence = submergence_max;
183     results.acc = acc_submerged;
184     results.vel = vel_submerged;
```

Bibliography

Battistin, D. and Iafrati, A. Hydrodynamic loads during water entry of two-dimensional and axisymmetric bodies. *Journal of Fluids and Structures*, 17:643–664, 2003.

Campbell, I. and Weynberg, P. Measurement of parameters affecting slamming, 1980.

Chen, H.-C. and Yu, K. Cfd simulations of wave–current-body interactions including greenwater and wet deck slamming. *Computers & Fluids*, 38(5):970–980, May 2009. ISSN 0045-7930.

Cointe, R. and Armand, J.-L. Hydrodynamic impact analysis of a cylinder. *Journal of Offshore Mechanics and Arctic Engineering*, 109:237–243, 1987.

Cummins, W. The impulse response function and ship motions. In *International Symposium on Ship Theory*, 1962.

Daemrich, K. Investigations on orbital velocities and pressures in irregular waves. Technical report, University of Hannover, 1982.

DNV. Rp-c205: Recommended practice environmental conditions and environmental loads. Det Norske Veritas, 2014.

Greenhow, M. Water-entry and -exit of a horizontal circular cylinder. *Applied Ocean Research*, 10(4): 191–198, 1988.

Greenhow, M. and lin, W.-M. Nonlinear free surface effects: experiments and theory, 1983.

Greenhow, M. and Moyo, S. Water entry and exit of horizontal circular cylinders, 1997.

Greenhow, M. and Yanbao, L. Added masses for circular cylinders near or penetrating fluid boundaries– review, extension and application to water-entry, -exit and slamming. *Ocean Engineering*, 14(4):325–348, 1987.

Holthuijsen, L. *Waves in Oceanic and Coastal Waters*. Cambridge University Press, 2007.

Jacobsen, V. and Hansen, E. The concepts of added mass and inertia forces and their use in structural dynamics. OTC'90, 22nd Annual Offshore Technology Conference, 1990.

Journee, J. and Massie, W. *Offshore Hydromechanics*. Delft University of Technology, 2001.

Justesen, P. Hydrodynamic forces on large cylinders in oscillatory flow. *Journal of Waterway, Port, Coastal and Ocean Engineering*, 15:497–514, 1989.

Larsen, E. Impact loads on circular cylinders, 2013.

Lin, M.-C. and Shieh, L.-D. Flow visualization and pressure characteristics of a cylinder for water impact. *Applied Ocean Research*, 19(2):101–112, April 1997. ISSN 0141-1187.

Longoria, R., Beaman, J., and Miksad, R. An experimental investigation of forces induced on cylinders by random oscillatory flow. *Journal of Offshore Mechanics and Arctic Engineering*, 113:275–285, 1991.

Miller, B. Wave slamming loads on horizontal circular elements of offshore structures. Technical report, Middlesex National Maritime Institute, 1977.

Moran, J. P. On the hydrodynamic theory of water-exit and -entry, 1965.

Morison, J., O'Brien, M., Johnson, J., and Schaaf, S. The froces exerted by surface waves on piles. *Journal of Petroleum Technology*, 189:149–154, 1950.

Moyo, S. and Greenhow, M. Free motion of a cylinder moving below and through a free surface. *Applied Ocean Research*, 22(1):31–44, February 2000. ISSN 0141-1187.

Panciroli, R., Abrate, S., Minak, G., and Zucchelli, A. Hydroelasticity in water-entry problems: Comparison between experimental and sph results. *Composite Structures*, 94(2):532–539, January 2012. ISSN 0263-8223.

Piro, D. J. and Maki, K. J. Hydroelastic analysis of bodies that enter and exit water. *Journal of Fluids and Structures*, 37(0):134–150, February 2013. ISSN 0889-9746.

Sarpkaya, T. In-line and transverse forces on smooth and sand-roughened cylinders in oscillatory flow at high reynolds numbers. Technical report, Naval Postgraduate School, 1976.

Scarpkaya, T. Force on a circular cylinder in viscous oscillatory flow at low keulegan-carpenter numbers. *Journal of Fluid Mechanics*, 165:61–71, 1986.

Schewe, G. On the force fluctuations acting on a circular cylinder in cross-flow from subcritical up to transcritical reynolds numbers. *Journal of Fluid Mechanics*, 133:265–285, 1983.

Seif, S., Mousaviraad, M., Saddathosseini, H., and Bertram, V. Numerical modelling of 2-d water impact in one degree of freedom. *Sint. Tecnolog*, 2:79–83, 2005.

Smaling, H. Hydrodynamic loading on the shaft of a gravity based offshore wind turbine, 2013.

Sumer, B. M. and Fredsoe, J. *Hydrodynamics around cylindrical structures*. World Scientific, 1997.

Sun, H. and Faltinsen, O. M. Water impact of horizontal circular cylinders and cylindrical shells. *Applied Ocean Research*, 28:299–311, 2007.

Ushanth, N. C. Wave slamming forces on truss structures for wind turbines, 2013.

Vinje, T. and Brevig, P. Nonlinear, two-dimensional ship motions, 1981.

von Karman, T. The impact on seaplane floats during landing. NACA, 1929.

Wagner, H. Uber stoss- und gleitvorgange an der oberflache von flussigkeiten. *Journal of Applied Mathematics and Mechanics / Zeitschrift fur Angewandte Mathematik und Mechanik*, 12:193–215, 1932.

Wang, W. and Wang, Y. An improved free surface capturing method based on cartesian cut cell mesh for water-entry and -exit problems, 2009.

Yan, H. and Liu, Y. An efficient high-order boundary element method for nonlinear wave–wave and wave-body interactions. *Journal of Computational Physics*, 230(2):402–424, January 2011. ISSN 0021-9991.

Zhao. Water entry of arbitrary two-dimensional sections with and without flow separation, 1996.

List of Figures

1.1 Pictures of cylindrical members in offshore applications . . . 2
1.2 Pictures of heavy marine transport for offshore applications . . . 3
1.3 Simulation screenshot of oversized cylinder transport . . . 5

2.1 Definition sketch for drag force sources. [Sumer and Fredsoe, 1997] . . . 8
2.2 Drag coefficient as function of Reynolds number for cylinders. Taken from [Sumer and Fredsoe, 1997], originally from [Schewe, 1983] . . . 9
2.3 Definition sketch angle of attack. [Sumer and Fredsoe, 1997] . . . 11
2.4 In-Line force coefficients for a free, smooth cylinder. Taken from [Sumer and Fredsoe, 1997], orginally from [Justesen, 1989, Sarpkaya, 1976, Scarpkaya, 1986, Schewe, 1983] . 12
2.5 Typical force coefficients for irregular waves [Longoria et al., 1991]. Re/KC = 2323. . 13
2.6 Cylinder water entry sketches . . . 15
2.7 Different historical solutions for C_s [Greenhow and Yanbao, 1987] . . . 16
2.8 Slamming coefficient C_s as a function of dimensionless submergence for 8° inclined water entry of cylinders. A comparison between experiments [Campbell and Weynberg, 1980] and CFD computations [Larsen, 2013]. Taken from [Larsen, 2013] . . . 17
2.9 Reference frames . . . 19
2.10 Extrapolation of slamming coefficient values . . . 21

3.1 Schematisation of ship motions . . . 24
3.2 Top view of horziontal distances between a POI and the wave origin . . . 26
3.3 Surface elevation amplitudes with wave diffraction for $\beta = 180°$ . . . 28
3.4 Amplitudes of radiated waves due to heave and pitch at $0.60\,\mathrm{rad\,s^{-1}}$ relative to a unit amplitude of the corresponding motion . . . 29
3.5 Relative motion definition sketch and photographic detail of pile support structure at barge stern . . . 30
3.6 Comparison of RAO's of z_{rel} between the disturbed and undisturbed approach for a point at 20 m behind the barge stern . . . 32
3.7 Maximum impact velocity . . . 35
3.8 Maximum submerged acceleration . . . 36
3.9 Maximum submerged velocity . . . 37
3.10 Maximum emerged acceleration . . . 39
3.11 Visualization of segmented model . . . 40
3.12 Sketched impression of position and loading during water entry state . . . 41
3.13 Sketched impression of position and loading during drag downward state . . . 42
3.14 Sketched impression of position and loading during drag upward state . . . 44
3.15 Bending moments at first support . . . 45

4.1 RAO of z_{rel} at 22 m behind stern for 8 wave headings . . . 48

4.2 Left: Jonswap variance density spectrum, $\gamma = 3.3, H_s$ =6.3 m. Right: Response spectrum z_{rel} at 22 m overhang for $\beta = 180°$ 49
4.3 Visualization of segmented model 54
4.4 Example of amplitudes and phase shift used in IFFT 55
4.5 Example of a time trace realisation 56
4.6 Example of a time trace realization for one segment at 22 m overhang length and wave heading 180° 57
4.7 Extreme value analysis for total vertical forces results from segmented model approach with disturbed sea surface for $\beta = 180°$ 59

5.1 Validation sketch orientation 1 62
5.2 Simulation results for validation orientation 1 62
5.3 Validation sketch orientation 2 63
5.4 Simulation results for validation orientation 2 64
5.5 Validation sketch orientation 3 65
5.6 Simulation results for validation orientation 3 66

6.1 Restoring moment 68
6.2 Different encountered lay outs for pile transport 69
6.3 Multiple piles on a row with limited spacing leads to screen effects 69

A.1 System sketches for floating bodies 78
A.2 Photograph of modelled barge 80
A.3 Patch model used in WAMIT calculations 84
A.4 Added mass coefficients 86
A.5 Damping coefficients 87
A.6 Surge RAO's 88
A.7 Sway RAO's 89
A.8 Heave RAO's 90
A.9 Roll RAO's 91
A.10 Pitch RAO's 92
A.11 Yaw RAO's 93

B.1 Amplitudes and phase shifts of sea surface elevation due to diffraction at $\omega = 0.69\,\mathrm{rad\,s^{-1}}$ ($T = 9.11$ s) for headings 0°, 45°, 90°, and 135°. Amplitudes and phase shifts are relative to an incident unit wave at the same frequency. 96
B.2 Amplitudes and phase shifts of sea surface elevation due to diffraction at $\omega = 0.69\,\mathrm{rad\,s^{-1}}$ ($T = 9.11$ s) for headings 180°, 225°, 270°, and 315°. Amplitudes and phase shifts are relative to an incident unit wave at the same frequency. 97
B.3 Amplitudes and phase shifts of sea surface elevation due to radiation of translation motions at $\omega = 0.69\,\mathrm{rad\,s^{-1}}$ ($T = 9.11$ s). Amplitudes and phase shifts are relative to their corresponding motion at the same frequency. 98
B.4 Amplitudes and phase shifts of sea surface elevation due to radiation of rotation motions at $\omega = 0.69\,\mathrm{rad\,s^{-1}}$ ($T = 9.11$ s). Amplitudes and phase shifts are relative to their corresponding motion at the same frequency. 99
B.5 RAO's of z_{poi} 100
B.6 RAO's of $^{d}/_{dt} z_{poi}$ 101
B.7 RAO's of $^{d^2}/_{dt^2} z_{poi}$ 102
B.8 RAO's of z_{rel} for a disturbed approach 103

B.9 RAO's of $^{d}/_{dt}z_{rel}$ for a disturbed approach 104
B.10 RAO's of $^{d^2}/_{dt^2}z_{rel}$ for a disturbed approach 105

C.1 Load case 1 109
C.2 Load case 2 110
C.3 Load case 3 110
C.4 Load case 4 111
C.5 Load case 5 111

D.1 Flowchart of approaches 113
D.2 Flowchart of segmented model 114

List of Tables

2.1 Motion notations 19

4.1 Characteristics of the case study 48
4.2 Significant values from a spectral analysis for a point at 22 m behind the barge stern . 50
4.3 MPM load results from the current engineering method for undisturbed sea surfaces. . 51
4.4 MPM values for a 3 hour storm from a spectral analysis for a point at 22 m behind the barge stern 52
4.5 MPM lengths measures over which forces act 52
4.6 MPM load results from a quasi-stationary approach for disturbed and undisturbed sea surfaces. 53
4.7 Difference between simulations with and without refined water entry time step. MPM and P95 total upward force results from 100 simulations for β =180°, $\Delta t = 0.1$ s, and $\Delta t_{int} = 0.01$ s with disturbed sea surface approach. 56
4.8 Influence of time step size on force results. Obtained from 100 simulations for β =180° with disturbed sea surface approach. 58
4.9 MPM and P95 load results out of 100 simulations from a segmented model approach for disturbed and undisturbed sea surfaces. $\Delta x = 1$ m,$\Delta t = 0.1$ s, *Dis* = disturbed sea surface approach, *Und* = undisturbed sea surface approach. 59

A.1 Barge characteristics 80

C.1 MPM values for a 3 hour storm from a spectral analysis with an undisturbed approach for different POI's 108